

# 國立交通大學

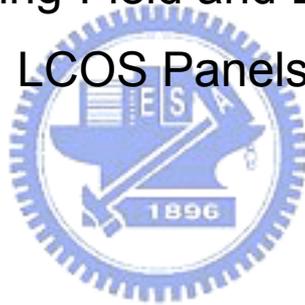
光電工程研究所

博士論文

反射式單晶矽液晶面板邊際場效應及繞射效應之研究

Study on the Fringing-Field and Diffraction Effects of

LCOS Panels



研究生：范姜冠旭

指導教授：王淑霞 教授

吳詩聰 教授

中華民國 九十四 年 六 月

反射式單晶矽液晶面板邊際場效應及繞射效應之研究

**Study on the Fringing-Field and Diffraction Effects of  
LCOS Panels**

研究生：范姜冠旭  
指導教授：王淑霞  
吳詩聰

Student : Kuan-Hsu Fan-Chiang  
Advisor : Shu-Hsia Chen  
Shin-Tson Wu

國立交通大學光電工程學系暨研究所  
博士論文

A Dissertation

Submitted to Department of Photonics and Institute of Electro-Optical Engineering

College of Electrical Engineering and Computer Science

National Chiao Tung University

in partial Fulfillment of the Requirements

for the Degree of

Doctor of Philosophy

in

Electro-Optical Engineering

June 2005

Hsinchu, Taiwan, Republic of China

中華民國九十四年六月

# 反射式單晶矽液晶面板邊際場效應及繞射效應之研究

研究生：范姜冠旭

指導教授：王淑霞 教授

吳詩聰 教授

國立交通大學光電工程學系暨研究所

## 摘要

近年來，反射式單晶矽液晶(LCOS)元件一直是顯示產業持續注意的焦點，尤其是在投影顯示器的應用方面，其產品包括前投式投影機、背投式電視以及頭戴式虛擬顯示器等。由於單晶矽的電子漂移率甚高，因此 LCOS 元件可以擁有非常高的解析度，除此之外，其周圍的驅動電路也可以整合在單一的晶片上以減少生產成本。在製造方面，LCOS 液晶面板乃建立在國內兩大產業的基礎上，即半導體與液晶顯示器產業，因此，這對於國內發展 LCOS 不啻為一大利基。由於矽基板的製造是屬於標準的半導體製程，所以具有低價格的潛力與優勢，也因此許多廠商已紛紛投入 LCOS 投影顯示器這個產業。

然而，目前 LCOS 顯示技術仍然存在著許多困難有待克服。在面板方面，由於要在微小的面板上做出高解析度的影像，其像素以及像素間距也相對地變得非常小。當相鄰像素的施加電壓不同時，其邊緣電場會被扭曲，使得此處的液晶分子產生不正常的排列，進而影響其光學特性，這就是所謂的邊際場效應。

此外，當解析度的要求提高而使得像素電極的大小接近可見光的波長時，其對光波的作用類似於一反射光柵。當光入射在面板上時會產生明顯的繞射效應，而斜向傳播的繞射光可能無法進入光學系統，因而造成嚴重的光損失。

在本論文中，我們探討八個常用液晶模態的邊際場效應，並且改變液晶盒參數，研究其對 LCOS 面板光學表現的影響。我們發現混和式扭轉向列型液晶模態的邊際場效應相對較弱，而扭轉向列型和垂直排列型液晶模態則會受到嚴重的邊際場效應影響而降低其影像品質。特別是對於垂直排列型液晶模態，其邊際場效應不但影響其靜態

顯示的品質，同時也嚴重地拖慢了動態影像的切換速度。在液晶盒結構方面，根據電腦程式的模擬結果，我們也發現像素節距、液晶盒厚度、預傾角和電極斜率都是影響邊際場效應的重要參數。

為了要設計一個高對比度且同時不受邊際場效應影響的 LCOS 面板，我們針對擁有完美暗態的垂直排列型液晶盒做分析。根據電腦模擬出的液晶指向矢分佈，我們發現利用圓偏振光的特性，可以有效地保留因邊際場效應所損失的光效率進而提高影像的銳利度；同時，在動態響應上也解決了因緩慢切換過程而產生的影像模糊問題。相關的光學原理可以由著名的 de Vries 理論來解釋。

在探討 LCOS 面板的繞射效應方面，由於傳統的瓊斯矩陣法並無法分析光的繞射效應，因此我們將以往應用在光波導計算的光束傳播法延伸到 LCOS 元件的光學計算，而撰寫出有考慮繞射效應的光學模擬程式。利用此程式，我們針對垂直排列型液晶模態以及工研院電子所研發的 FOP(finger-on-plane)模態進行分析。模擬結果顯示繞射效應對高解析度的 LCOS 元件影響甚巨；使用傳統瓊斯矩陣法會造成嚴重的誤差，唯有使用更嚴謹的光束傳播法才能正確的預估其光學行為。此外，我們發現稍微修改 FOP 模態的液晶盒結構能有效地降低在特定波段的繞射效應，若配合使用三片或雙片式的 LCOS 投影光學系統，則可以有效地提升因繞射效應所損失的光效率。

# Study on the Fringing-Field and Diffraction Effects of LCOS Panels

Student: Kuan-Hsu Fan-Chiang

Advisor: Prof. Shu-Hsia Chen

Prof. Shin-Tson Wu

**Department of Photonics and Institute of Electro-Optical Engineering  
National Chiao Tung University**

## Abstract

In recent years, the display industries keep showing great interests in liquid-crystal-on-silicon (LCOS) devices, especially in the application of projection display. The products of LCOS devices include data projectors, rear-projection TV and the head-mounted virtual display. Due to the advantage of intrinsic high electron mobility of crystalline silicon, LCOS devices can be fabricated with very high resolution. In addition, its peripheral driving circuits can be integrated on a single chip, which greatly reduces the cost of manufacturing. Technically, LCOS devices are based on two major domestic industries: the semiconductor and liquid crystal display industries. Since the fabrication of the silicon backplane is based on the standard manufacturing process of semiconductor, LCOS devices have great potential of low price. Therefore, many manufacturers have already invested in this industry.

However, there are still many challenges in the LCOS industry. The two major issues of LCOS panels are the fringing-field and diffraction effects. As the resolution increases, the pixel size and the inter-pixel gap will become very small. When the applied voltages between adjacent pixels are different, the electric fields near the pixel edges will be distorted. Hence, the liquid crystal molecules near this region are aligned abnormally, which, in turns, degrades the optical performance of the device significantly. This is the so-called fringe field effect.

In addition, as the pixel pitch becomes comparable to the wavelength of the visible light, the LCOS panel acts as a reflective grating. Therefore, obvious diffraction effect can be

observed. The oblique diffracted light may not be able to enter the optical system, and consequently results in serious light loss.

In this dissertation, we investigate the fringing-field effects of eight commonly used liquid crystal modes. We also investigate the influence of the LC cell structure on the optical performance of LCOS devices. It is found that the mixed-mode twist nematic (MTN) has weaker fringing-field effect while the twist nematic mode (TN) and vertically aligned mode (VA) suffer from the effect significantly. The fringing-field effect is particularly severe in VA mode. It not only degrades the static image qualities but also deteriorates the dynamic response of the LCOS panel. The pixel pitch, cell gap, pretilt angle and electrode slope are all found critical to the fringing-field effect.

In order to design a high-contrast-ratio LCOS panel without fringing-field effect, we focus on the analyses of VA mode which possesses an excellent dark state. Based on the simulated results of the LC director profile, we find that, by utilizing the properties of circularly polarized light, the light loss caused by fringing-field effect can be preserved and the sharpness of the image can be enhanced dramatically. Moreover, the dynamic response is also improved and the imaging blurring effect is successfully eliminated. The results can be qualitatively illustrated by the de Vries theory.

With regard to the effect of diffraction, a rigorous simulator is needed to investigate the optical performance of a high-definition LCOS panel. The conventional Jones matrix method is no longer suitable in this condition. We extend the beam propagation method (BPM), which is commonly employed in waveguide calculations, to the optical simulation of LCOS devices. Two promising LC operation modes are analyzed by BPM, i.e. VA and finger-on-plane (FOP) modes. The calculated light efficiencies by Jones matrix method and BPM with respect to the pixel pitch are compared. It is shown that the diffraction effect is critical to the light efficiency. Using Jones matrix method may give rise to significant miscalculation. By using BPM, it is found possible to reduce the diffraction effect for certain waveband by slightly modifying the FOP cell structure, suggesting that the light efficiency can be boosted effectively in a two- or three-panel LCOS projection system.

## 致謝 Acknowledgement

時光匆匆，在交大已經待了九個年頭。回想起來，能夠拿到博士學位，需要感謝的人實在太多。其中，家人當然是我最重要的精神支柱。感謝我的父親 范姜超沐先生對我的栽培，您始終是我內心中最重要的依靠。感謝我的母親 翁明甘女士對我無微不至的照顧，讓我遇到挫折時有一個安全的避風港。感謝我的哥哥 范姜冠宇先生陪我一起成長，一起分享心情，讓我的生活更加精彩。

在此要特別感謝我的指導教授 王淑霞教授。您在課業上和做人處事上的教導讓我一生受用無窮。您對我們的關懷照顧，早已超越了一般師生的關係。對我來說，您更像是一位親人。很難用短短的幾句話表達對老師的感激，只希望自己未來能夠不辜負老師的期望，繳出一張漂亮的成績單。

也要特別感謝的是美國的指導教授 吳詩聰教授。感謝吳老師讓我有機會能去美國深造。在美國一年的期間中，我在吳老師的指導下學到許多寶貴的知識和經驗，並且讓我的眼界更加寬廣。同時也感謝吳師母在我初到美國時貼心的照顧，使我感覺雖然身在異鄉，卻有在家鄉的溫暖。由衷的感謝您們。

在美國的期間，我要感謝 林怡欣學姊和 吳勇勳學長的照顧。有你們的陪伴讓我感覺很溫馨。感謝 朱新羽博士給我許多寶貴的意見，和您討論經常能夠激盪出許多有趣的新點子。同時我還要感謝許多在美國的朋友：*Mr. Tim Wilson, Mr. and Mrs. Kim, Mr. and Mrs. Matsubara, Mr. and Mrs. Teruaki. Thanks for sharing all the good times with me in Orlando. You guys are the best!!*

感謝液晶實驗室的學長姐們：秋蓮、志勇、阿寬、俊雄、芝珊、揚宜、彥廷、信全、乾煌、梓傑、佳成；我的同學們：怡安、惠雯、庭瑞、朝旭、英豪；以及學弟妹們：舒展、德源、建宏、世郁、品發、美琪、家榮、庭毅、瑞傑。你們讓我的研究生生活多采多姿。尤其要感謝芝珊、庭毅、瑞傑在最後關頭拼畢業的同時也分擔了實驗室許多繁重的工作。很高興我們一起做到了。

僅以此論文獻給我最親愛的家人、師長、以及所有關心我和幫助過我的人。由衷的感謝。

范姜冠旭  
新竹交通大學 2005 年 6 月

# Contents

Abstract (in Chinese).....	i
Abstract (in English) .....	iii
Acknowledgement (in Chinese).....	v
Contents .....	vi
List of Figures .....	viii
List of Symbols .....	xiii
Chapter 1 Introduction.....	1
1.1 Overview of LCOS devices.....	1
1.2 The issues of LCOS projection displays.....	10
1.2.1 The issues of optical engines .....	10
1.2.2 The issues of LCOS panels .....	12
1.3 Aims of the research.....	13
Chapter 2 Theory and Numerical Simulation .....	17
2.1 Theories of deformations and optical properties of liquid crystals.....	17
2.1.1 Continuum theory of liquid crystals.....	17
2.1.2 Optical properties of an ideal helix: de Vries theory .	22
2.2 Numerical Simulations .....	30
2.2.1 Jones matrix method .....	30
2.2.2 Beam propagation method .....	36
Chapter 3 Fringing-Field Effects of LCOS Devices.....	46
3.1 Introduction .....	46
3.2 Liquid crystal operation modes .....	46
3.2.1 Twisted LC modes.....	47
3.2.1.1 Mixed-mode twisted nematic (MTN).....	48
3.2.1.2 Twisted nematic modes (TN) .....	55

	3.2.2 Non-twisted LC modes .....	61
	3.2.2.1 Vertically aligned mode (VA).....	61
	3.2.2.2 Film-compensated homogenous mode (FCH) ..	63
	3.3 Influences of the cell structures .....	65
	3.3.1 The effect of pixel pitch .....	65
	3.3.2 The effect of cell thickness .....	66
	3.3.3 The effect of pretilt angle .....	68
	3.3.4 Electrode slope effect .....	69
	3.4 Dynamic response of the panel switched from the dark-bright-dark state to the all-bright state .....	70
	3.5 Conclusion .....	72
Chapter 4	Circularly Polarized Light Illuminated Vertically Aligned LCOS Device.....	76
	4.1 Introduction .....	76
	4.2 Simulation results.....	77
	4.3 Theoretical interpretation .....	80
	4.4 Experimental results .....	83
	4.5 Optical engines for CPVA device.....	85
	4.6 Conclusion .....	88
Chapter 5	Diffraction Effect of the LCOS Devices .....	91
	5.1 Introduction .....	91
	5.2 The influence of the pixel pitch to the light efficiency.....	92
	5.3 Phase-compensated finger-on-plane mode.....	99
	5.4 Conclusion .....	100
Chapter 6	Summary and Future Scope .....	102
Vita	.....	105

# List of Figures

- 1.1 Schematic of pixel apertures in (a) transmissive and (b) reflective light valves.
- 1.2 Cross-section of a common LCOS structure.
- 1.3 A Typical three-panel LCOS projection system. M1, M2, M3 and M4 are mirrors. DM1 is the cyan/red dichroic mirror and DM2 is the green/blue dichroic mirror. PBS is the polarizing beam splitter and PSC is the polarization state converter.
- 1.4 Intensity homogenization optical parts: (a) the fly's eye lenslet elements; (b) light pipe.
- 1.5 (a) The polarization state converter; (b) the typical front end of a LCOS optical engine.
- 1.6 The time-sequential system using a rotating color wheel with red, green and blue segments.
- 1.7 The time-sequential rotating-prism system.
- 1.8 Single-panel LCOS system using holographic color filter.
- 1.9 (a) Sketch of the Brewster angle reflection; (b) an calculated results of normalized reflectance with respect to incident angle when light propagating from air to  $Ti_2O_3$  ( $n=2.45$ ).
- 1.10 Sketch of the fringing fields at the pixel edges when adjacent pixels are operated at different voltages.
- 1.11 Sketch of the diffraction effect of LCOS devices.
- 2.1 Structure of chiral nematic liquid crystals.  $P_0$  is the natural pitch.
- 2.2 (a)The dispersion relation of a CLC with  $n_e=1.5578$ ,  $n_o=1.4748$  and  $P_0=0.25 \mu m$ ; the insert denotes the characteristics of eigenmodes at some specific frequencies; (b) Calculated ellipticity with respect to  $l_2/q_0$  when  $-1 < l_2/q_0 < 0$ ; (c) Calculated ellipticity with respect to  $l_2/q_0$  when  $0 < l_2/q_0 < 10^3$ ; (d) Calculated ellipticity with respect to  $l_1/q_0$  when  $0 < l_1/q_0 < 600$ .
- 2.3 The calculate (a)  $B/A$  and (b)  $\phi_b - \phi_a$  with respect to frequency.

- 2.4 The represented Jones matrix can be derived by subdividing the LC layer into a large number,  $N$ , of thin layers.
- 2.5 Sketch of the mirror image of a left-handed twist LC cell.
- 2.6 The angle definitions in numerical calculations.
- 2.7 Sketches of the concepts of the (a) Jones matrix method and (b) the beam propagation method.
- 3.1 The LC cell structure used for the two-dimensional simulations.
- 3.2 Simulated results of (a) the broad band RV curve, (b) the broad band green light iso-contrast viewing diagram, and (c) the LC director and the reflectance profiles of NW  $90^\circ$ -MTN mode with  $\beta=20^\circ$  and  $d\Delta n=240$  nm.
- 3.3 Simulated results of (a) the broad band RV curve, (b) the broad band green light iso-contrast viewing diagram, and (c) the LC director and the reflectance profiles of  $63.6^\circ$ -MTN mode with  $\beta=0^\circ$ ,  $d\Delta n=203$  nm,  $(d\Delta n)_{\text{film}}=24$  nm, and  $110^\circ$  film angle related to x-axis.
- 3.4 Simulated results of (a) the broad band RV curve, (b) the broad band green light iso-contrast viewing diagram, and (c) the LC director and the reflectance profiles of  $45^\circ$ -MTN mode with  $\beta=78^\circ$ ,  $d\Delta n=195$  nm,  $(d\Delta n)_{\text{film}}=27$  nm, and  $110^\circ$  film angle related to x-axis.
- 3.5 Simulated results of (a) the broad band RV curve, (b) the broad band green light iso-contrast viewing diagram, and (c) the LC director and the reflectance profiles of NB  $63.6^\circ$ -TN mode with  $\beta=0^\circ$ ,  $d\Delta n=508$  nm, and  $d/p=0.6$ .
- 3.6 Calculated results of the contrast ratio with respect to  $d/p$  ratio for  $63.6^\circ$ -TN mode with  $d=2.1$   $\mu\text{m}$ .
- 3.7 Simulated results of (a) the broad band RV curve, (b) the broad band green light iso-contrast viewing diagram, and (c) the LC director and the reflectance profiles of NB  $45^\circ$ -TN mode with  $\beta=0^\circ$ ,  $d\Delta n=533$  nm.
- 3.8 Simulated reflectance of NB  $45^\circ$ -TN mode with  $d=2.2$   $\mu\text{m}$ .
- 3.9 Simulation results of (a) the broad band RV curve, (b) the broad band green light iso-contrast viewing diagram, and (c) the LC director and the reflectance profile of

NB 52°-TN mode with  $\beta=0^\circ$ ,  $d\Delta n=517$  nm.

- 3.10 Simulated reflectance of NB 52°-TN mode with  $d=2.2$   $\mu\text{m}$ .
- 3.11 Simulation results of (a) the broad band RV curve, (b) the broad band green light iso-contrast viewing diagram, and (c) the LC director and the reflectance profile of VA mode with  $\beta=45^\circ$ ,  $d\Delta n=192$  nm and  $(d\Delta n)_{\text{c-film}}=-183$  nm.
- 3.12 The simulated green band reflectance profile of FCH mode,  $d_1\Delta n_1=184$ ,  $\beta=45^\circ$  (a) without compensation film, and (b) with compensation film,  $d_2\Delta n_2=52$  nm.
- 3.13 Sketch of the influence of the pixel pitch to the fringing-field effect.
- 3.14 Calculated contrast ratio of each LC operation mode at dark-bright-dark state with respect to the pixel size.
- 3.15 Sketch of the effect of cell gap.
- 3.16 Calculated contrast ratio of 63.6°-TN, 45°-TN and 52°-TN at dark-bright-dark state with respect to cell gap.
- 3.17 Sketch of the effect of pretilt angle to negative liquid crystal molecules.
- 3.18 (a) Simulated reflectance profiles of VA mode at dark-bright-dark state with pretilt angle varies from  $85^\circ$  to  $88^\circ$ , and (b) the calculated optical filled factor with respect to the pretilt angle.
- 3.19 Calculated optical filled factor with respect to evolution time of VA cell after switched from dark-bright-dark state to the all-bright state with pretilt angle varies from  $85^\circ$  to  $88^\circ$ .
- 3.20 (a) Sketch of the electrode slope; (b) Calculated contrast ratio with respect to the electrode slope ranging from 0.3 to  $\infty$  at dark-bright-dark state for 90°-MTN, 45°-MTN and VA mode.
- 3.21 The calculated transient states of VA mode when switching from the dark-bright-dark state to the all bright state. The cell gap is  $2.3$   $\mu\text{m}$  and the pretilt angle is  $88^\circ$ .
- 4.1 Schematic drawing of the systems used for (a) the LPVA device and (b) the CPVA device. PBS=polarizing beam splitter; P=polarization axis, R is the LC alignment direction at the front surface.
- 4.2 The simulated LC director distribution and the corresponding reflectance profiles,

- $R_{LP}(x)$  and  $R_{CP}(x)$ , at the alternate dark and bright state for the CPVA and the LPVA systems, respectively. The on-state voltage  $V_{on}=5$  V and the off-state voltage  $V_{off}=0$ .
- 4.3 Calculated azimuthal angles ( $\phi$ ) of the LC directors along the z direction at  $x=x_1$ ,  $x_a$ ,  $x_b$  and  $x_2$  as denoted in Fig. 4.2.
  - 4.4 Photos captured by CCD through the polarizing microscope of the LC panel operated at the alternate bright and dark states for (a) the LPVA and (b) the CPVA devices. Photos of the LC panel switched from the alternate bright and dark states to the all-bright state for (c) the LPVA device at 198 ms after switching and (d) the CPVA device at 33 ms after switching.
  - 4.5 Measured reflectance with respect to the elapsed time after switching from the alternate bright and dark states to the all-bright state for the CPVA device.
  - 4.6 Sketch of the broadband circular polarizer which comprises a linear polarizer, a  $1/2\lambda$ -plate and a  $1/4\lambda$ -plate.
  - 4.7 The off-axis optical system for reflective CPVA device.
  - 4.8 The optical system using hologram film for reflective CPVA device.
  - 4.9 The optical system using Faraday rotator for reflective CPVA device.
  - 4.10 The three-panel optical system for transmissive CPVA high-temperature poly-Si LCD.
  - 5.1 Schematic representation of angle definitions and mirror image of reflective LCOS device.
  - 5.2 Sketch of the acceptance angle  $\theta_a$  of the light waves propagating from the LCOS panel to the projection lens.
  - 5.3 Cell structures used for 2D computer simulations of (a) FOP mode (b) VA mode.
  - 5.4 Computer simulated light efficiencies ( $\theta_a=10^\circ$ ) with respect to  $P/\lambda$  value of FOP-LCOS devices at voltage-off state by extended BPM and Jones matrix method.
  - 5.5 Simulated intensity angular spectrum with  $P=7.7$   $\mu\text{m}$  and  $\lambda=540$  nm for FOP mode.
  - 5.6 (a) Simulated light efficiencies with respect to  $P/\lambda$  value of VA-LCOS devices at voltage-off state by extended BPM and Jones matrix method, and (b) simulated intensity angular spectrum with  $P=7.7$   $\mu\text{m}$  and  $\lambda=540$  nm.

- 5.7 Computer simulated results of VA mode with off-on-off pixel configuration by extended BPM and Jones matrix method: (a) light efficiencies ( $\theta_a=10^\circ$ ) of LCOS devices with respect to  $P/\lambda$  value, (b) intensity angular spectrum with  $P=7.7 \mu\text{m}$  and  $\lambda=540 \text{ nm}$ , and (c) the intensity of zeroth-order diffracted light,  $I_0$ , calculated with respect to  $P/\lambda$  value.
- 5.8 Calculated light efficiency by reflective BPM with respect to wavelength for FOP mode ( $P=15.5 \mu\text{m}$ ) with  $d_i=115 \text{ nm}$  and  $150 \text{ nm}$ .



# List of Symbols

$n$	index of refraction
$\mathbf{n}$	director of liquid crystal
$g$	free energy density
$K_{11}$	elastic constant of the splay deformation
$K_{22}$	elastic constant of the twist deformation
$K_{33}$	elastic constant of the bend deformation
$P_0$	natural pitch of the structure of chiral liquid crystals
$q_0$	$2\pi/P_0$
$\varepsilon$	dielectric constant
$\mathbf{D}$	electric displacement
$\mathbf{E}$	electric field
$G$	total free energy
$n_o$	ordinary refractive index of liquid crystal
$n_e$	extraordinary refractive index of liquid crystal
$\omega$	angular frequency of light
$\rho$	ellipticity of light
$\mathbf{k}$	wavevector
$d$	thickness of liquid crystal cells
$\theta$	tilt angle of liquid crystal director
$\phi$	azimuthal angle of liquid crystal director
$\alpha$	the angle between the optical axis of compensation film and x-axis
$\beta$	the angle between the transmission axis of linear polarizer and the entrance liquid crystal director
$F$	optical filled factor
$F_{\#}$	f-number
$s$	electrode slope



# Chapter 1

## Introduction

### 1.1 Overview of LCOS devices

Information displays can be broadly categorized into direct-view and projection types. Direct-view displays generate images directly on the surfaces that can be viewed by human eyes. On the other hand, projection displays present their images on an auxiliary surface which is separated from the image-generating devices. These images can be either real or virtual depending on different applications.

Generally, there are three main technologies being developed for projection displays: poly-silicon thin-film-transistor (TFT) liquid crystal displays (LCDs) [1], digital light processing (DLP) [2] and liquid-crystal-on-silicon (LCOS) devices [3]. Table 1.1 compares the advantages and disadvantages of these three technologies. Among them, LCOS is especially attractive due to its standard semiconductor manufacturing process. This technology is particularly suitable to its development in Taiwan because of the mature semiconductor industry. When compared to transmissive-type LCDs, reflective-type LCOS light valves have higher aperture ratio since all of the electronic circuits can be hidden behind the reflective pixels. Figure 1.1 illustrates the schematic of pixel apertures in transmissive and reflective light valves. The black areas represent the light-absorbing material for blocking light to prevent any current leakage. The aperture ratio of reflective light valves can be above 90% while that of the transmissive one is only around 70%. On the aspect of DLP system, it has the advantage of fast response, high light efficiency and compactness which are very suitable for data projectors. However, when playing movies, the so-called color-breaking effect appears as a momentary flash of rainbow-like stripes

typically trailing the bright objects when looking from one side of the screen to the other [4]. This effect is intrinsically generated from the field-sequential color generating method which degrades the image quality significantly. Another drawback of DLP is the complex manufacturing process of the micro-electro-mechanical systems (MEMS) which becomes one of the main barriers for many investors.

Table 1.1 Comparison of LCD, DLP and LCOS for the application of projection display.

<b>Technologies</b>	<b>LCD</b>	<b>DLP</b>	<b>LCOS</b>
<b>Light valves</b>	Transmissive	Refelective	Reflective
<b>Companies</b>	Sony and Epson, etc.	Taxes Instruments	JVC, Aurora, Sony, Brillian, TMDC, Himax, etc.
<b>Advantages</b>	<ul style="list-style-type: none"> <li>•Mature technology</li> <li>•Mass productive</li> <li>•Simple optical engines</li> </ul>	<ul style="list-style-type: none"> <li>•Fast response (<math>\mu\text{s}</math> level)</li> <li>•High light efficeincy</li> <li>•Compact</li> </ul>	<ul style="list-style-type: none"> <li>•Standard semiconductor manufacturing</li> <li>•High aperture ratio</li> <li>•High resolutions (5-8 <math>\mu\text{m}</math> pitch)</li> </ul>
<b>disadvantage</b>	<ul style="list-style-type: none"> <li>•Low aperture ratio</li> <li>•Bulky</li> </ul>	<ul style="list-style-type: none"> <li>•Complex manufacturing</li> <li>•Less color saturation</li> <li>•Color breaking (rainbow effect)</li> </ul>	<ul style="list-style-type: none"> <li>•Low yield</li> <li>•Fringing field effect</li> <li>•Diffraction effect</li> </ul>

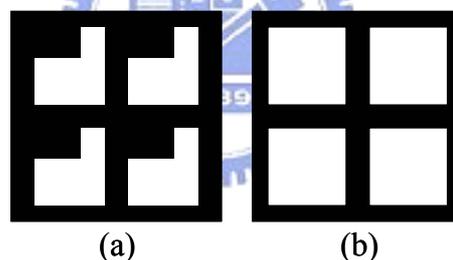


Figure 1.1 schematic of pixel apertures in (a) transmissive and (b) reflective light valves.

Figure 1.2 demonstrates the cross-section of a common LCOS structure. Basically, LCOS comprises a liquid crystal (LC) layer sandwiched between a cover glass slide (top substrate) and a crystalline silicon wafer (bottom substrate). The LC layer functions as an electro-optic modulator which delivers signals of displaying images to incident light. The LC effect will be discussed in Chap. 2. Owing to the high electron mobility of the silicon substrate, the pixel size can be shrunk to as small as 5-8  $\mu\text{m}$ , which results in a very high resolution. Some characteristics of LCOS microdisplay compared to those of TFT-LCDs are listed in Table 1.2. Another benefit of LCOS

from high electron mobility is the integration capability of driving circuits, which can reduce cost significantly and make the system more compact.

Optical engines play an important role in LCOS projection systems. There is a great diversity of the optical systems for LCOS devices. Basically, the engine is composed of an LCOS panel (or panels), color management optics, projection lens, basic display driving electronics and an illumination system. Optical engines can be roughly classified according to the number of LCOS panels employed in the system. In general, three-panel and single-panel systems are more popular than others, as will be discussed later. Other optical systems are less mature and will not be discussed in this dissertation.

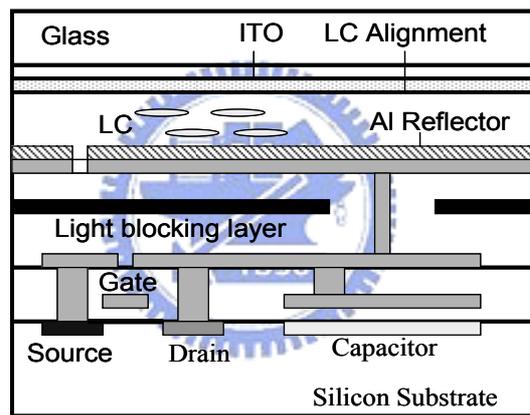


Figure 1.2 Cross-section of a common LCOS structure.

Table 1.2 Comparison of characteristics of TFT LCD and crystalline silicon based microdisplays.

TFT-LCDs	LCOS
Medium geometry	Small geometry
Line Width: several $\mu\text{m}$	Line Width: sub-microns
Large panel area	Small chip area
Low mobility	High mobility
$\alpha\text{-Si:}\sim 1.5$ ; $\text{p-Si:}150$ ( $\text{cm}^2/\text{Vs}$ )	$\sim 500$ $\text{cm}^2/\text{Vs}$
Transmissive	Reflective
Poor integration capability	Great integration capability

Figure 1.3 shows a typical three-panel LCOS projection system. Usually, an

ultra-high-pressure (UHP) mercury arc lamp is used to generate stable light throughput. This kind of lamps offers a small arc gap, acceptable efficiency and long lifetime [5]. However, some UV and IR radiations are also generated by the UHP lamp. UV light can be harmful to the LC alignments and IR light generates additional heat to the system. Therefore, UV/IR filters must be applied in front of the lamp in order to protect the system from these unwanted UV and IR components.

Integrated lenses including intensity-homogenizing elements are placed in the optical path behind the UV/IR filters. There are two main functions of the integrated lens. The first one is to homogenize the light intensity profile generated by the UHP lamp. The second is to transform the circular cross-section of light beams into a rectangular shape so that the beams can fit in with the size of LCOS light valves. Two approaches are commonly adopted: the fly's eye lenslet [6] and the light pipe elements [7]. The fly's eye approach consists of two lenslet elements with different patterns as shown in Fig. 1.4 (a). When light passes through these lenslets, a more uniform light intensity profile can be obtained. The other approach utilizes a hollow or solid rod as shown in Fig. 1.4 (b). Light coming from the lamp is coupled into the rod and is reflected off the internal walls by multiple total internal reflection. As light exits the light pipe, the light intensity will be evened out and produce uniform brightness.

LCOS light valves are polarization-dependent devices. Therefore, a polarizer must be used to polarize the light before it is incident on LCOS panels. A conventional dichroic polarizer theoretically absorbs half of the light which limits the light efficiency to 50%. A polarization state converter (PSC) can significantly recapture the light that is absorbed or dumped by a conventional polarizer. Figure 1.5 (a) illustrates one of such designs [8]. Unpolarized light is decomposed into p-wave and s-wave after it passes through a polarizing beam splitter (PBS). The reflected s-wave is then

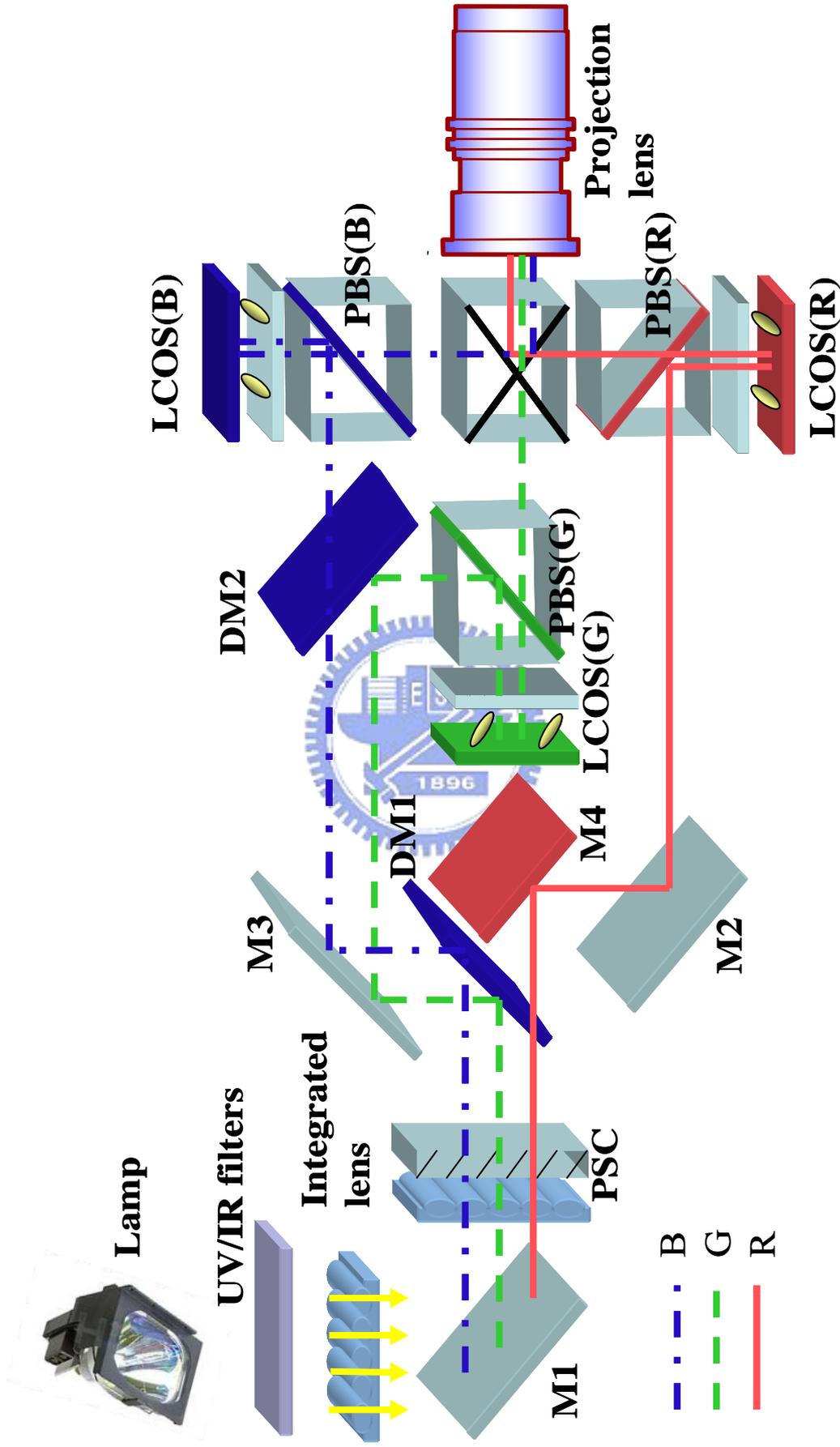
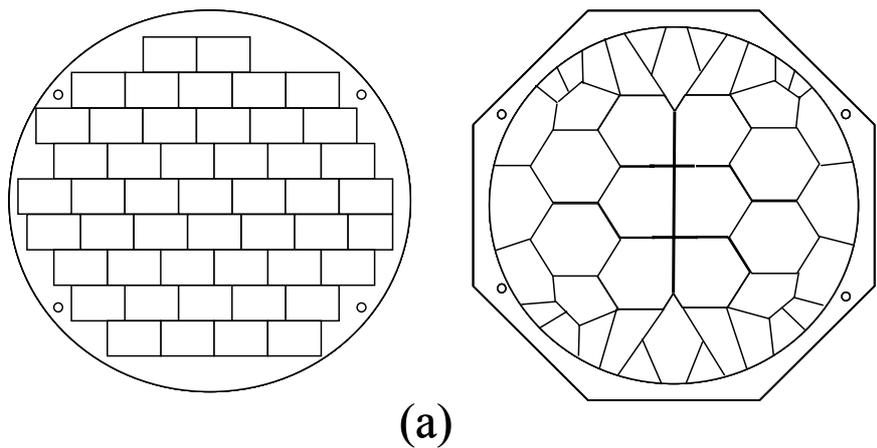
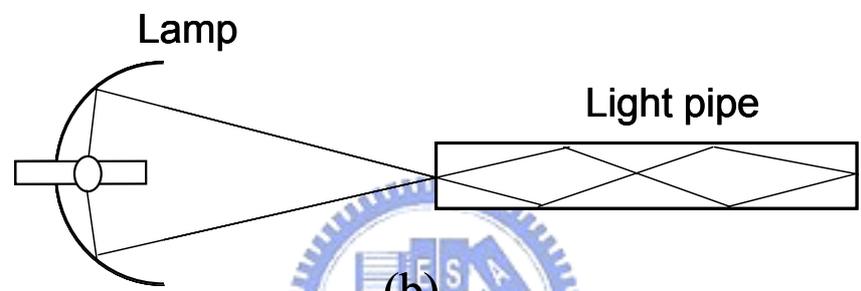


Figure 1.3 A Typical three-panel LCOS projection system. M1, M2, M3 and M4 are mirrors. DM1 is the cyan/red dichroic mirror and DM2 is the green/blue dichroic mirror. PBS is the polarizing beam splitter and PSC is the polarization state converter.

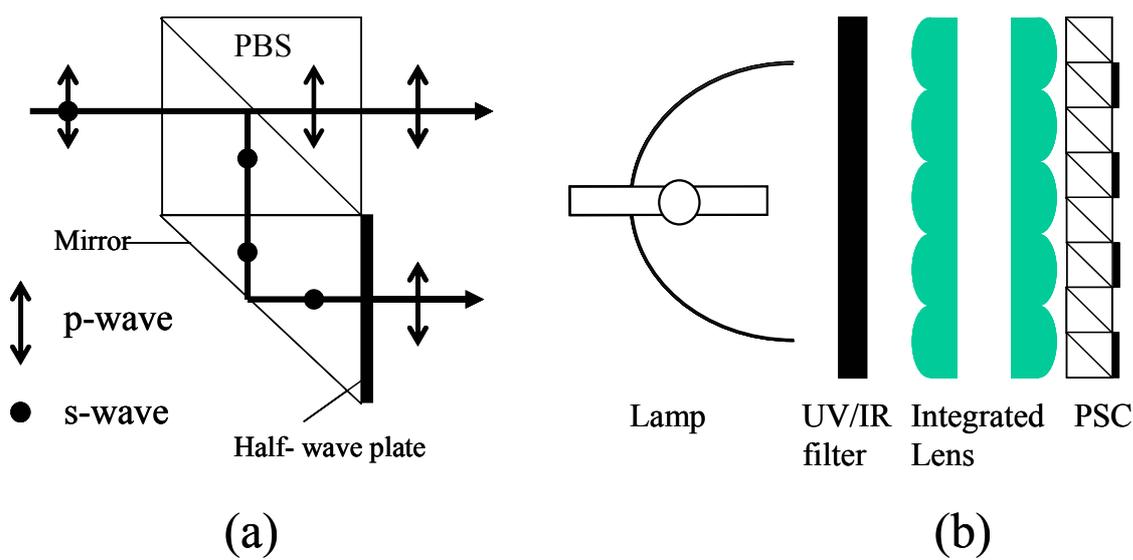


(a)



(b)

Figure 1.4 Intensity-homogenizing optical parts: (a) the fly's eye lenslet elements; (b) light pipe.



(a)

(b)

Figure 1.5 (a) The polarization state converter; (b) the typical front end of a LCOS optical engine

directed to a half-wave plate which rotates the polarization plane of the transmitted light to the direction parallel with p-wave. The light efficiency is, therefore, boosted effectively. A typical front end of an optical engine is formed comprising a lamp, UV/IR filters, integrated lens and PCS as shown in Fig. 1.5 (b).

A three-panel system needs to separate the red (R), green (G) and blue (B) wavebands from the white light. The most commonly employed element for color separation is a dichroic mirror (DM). The DM is constructed with thin-film stacks which induce interference for certain waveband and leave the others unaffected [9]. Hence, R, G and B wavebands can be separated by using the corresponding DMs as shown in Fig. 1.3. The basic requirements for these DMs are optical efficiency and high-temp durability.

Since LCOS systems are reflective-type devices, the PBS must be applied on the on-axis optical system in order to provide a crossed-polarizer condition. A PBS can pass light of one polarization state and reflect light of the other polarization state orthogonal to the former. When an s-wave is incident on a voltage-on LCOS panel, the reflected light will become p-wave which can pass through the PBS heading to the projection lens and display bright image on the screen. When the voltage is off, the reflected light will remain its polarization state, i.e. s-wave, and be reflected off by the PBS so that the image is dark. The gray level can be acquired by controlling the applied voltage on the LCOS panel. There are still several issues of PBS which will be addressed in the next section.

Another kind of optical engines commonly employed in LCOS projectors is the one-panel systems. Since only one light valve is needed, one-panel systems have the advantages of lower cost and compactness. Various designs have been developed in one-panel systems. There are in general two main approaches: time-sequential and sub-pixelated systems. For the time-sequential approach, the LCOS panel is illuminated by R, G and B lights subsequently. When the field-switching speed is fast enough that human eyes cannot catch up, the colors will be mixed together. Eventually, full color images are

formed. Figure 1.6 demonstrates a typical time-sequential system using a rotating color wheel with red, green and blue segments [10]. The emerging light after passing the colored segments is incident on the LCOS panel with R, G and B bands subsequently. The basic requirement of this system is the fast response time of LC. The rotating frequency is at least 180 Hz which means the minimum response time of LC is only 5.5 ms. To achieve this requirement, one can either use faster LC material, e.g. ferroelectric LC [11], or shrink the cell gap. Another concern of this system is the low light efficiency due to the absorption of 2/3 of the light after passing the color segments. In order to overcome this drawback, Philips constructed a rotating prism system [12] as shown in Fig. 1.7. In this system, the white light is divided into R, G, B bands by dichroic mirrors. A rotating prism is placed in the optical path of each waveband. The function of these prisms is to produce colored stripes scrolling on the LCOS panel. In this condition, three wavebands are displayed at the same time, implying the light energy is preserved. The main challenge of this system is the reduction of etendue because only 1/3 of the panel area is covered by a certain color.

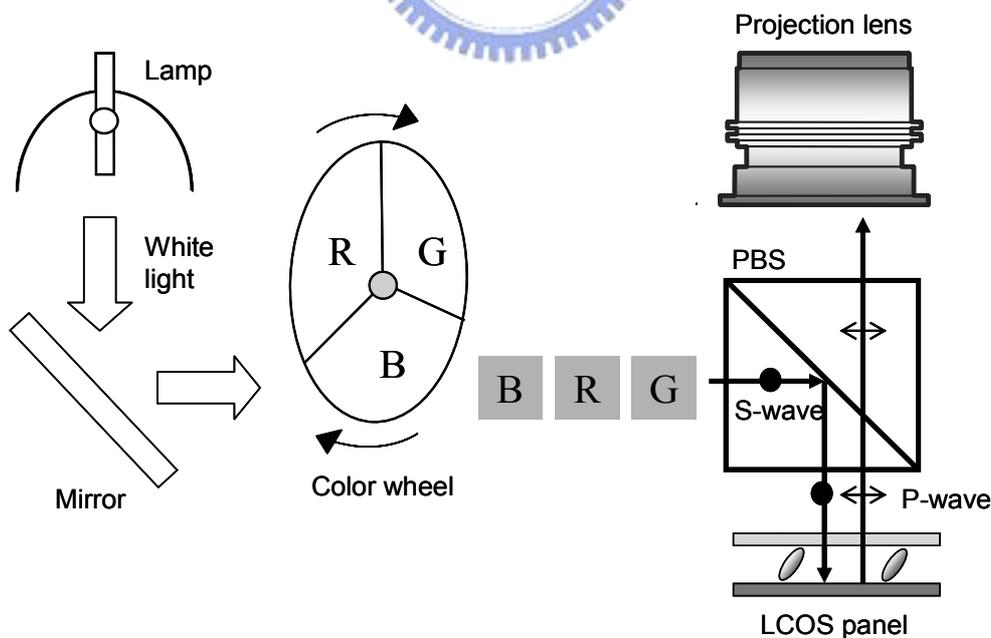


Figure 1.6 The time-sequential system using a rotating color wheel with red, green and blue segments.

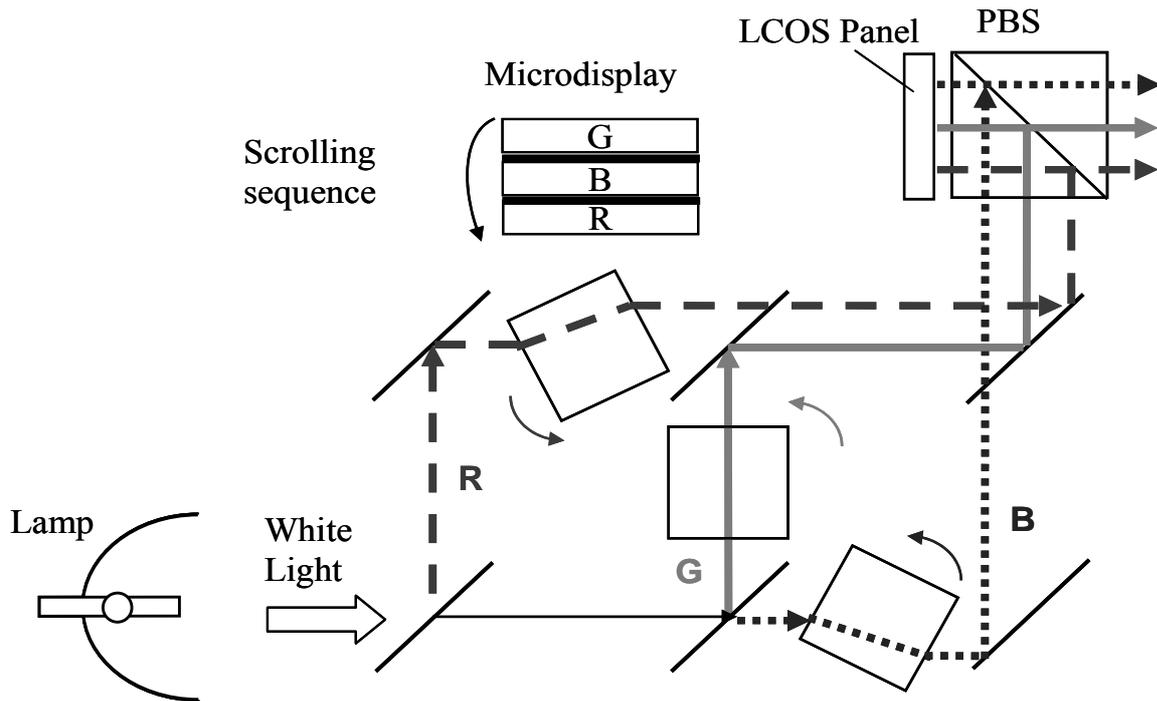


Figure 1.7 The time-sequential rotating-prism system.

JVC announced a single-panel system using a holographic color filter (HCF) with sub-pixelated architecture [13] as shown in Fig. 1.8. As white light encounters the HCF from a particular angle, it will be separated into R, G, B lights and directed to the corresponding sub-pixels. After modulated by the LC layer, the light will pass through the HCF again without diffractions. Finally, the light will be collected by the projection lens and displayed on the screen. This system has the advantage of high efficiency because three wavebands can be utilized simultaneously. However, the alignment of the HCF needs to be very precise which becomes a burden for yields.

Overall speaking, LCOS projection displays comprise various designs suitable for different applications. Several key issues of LCOS projection displays will be discussed in the next section.

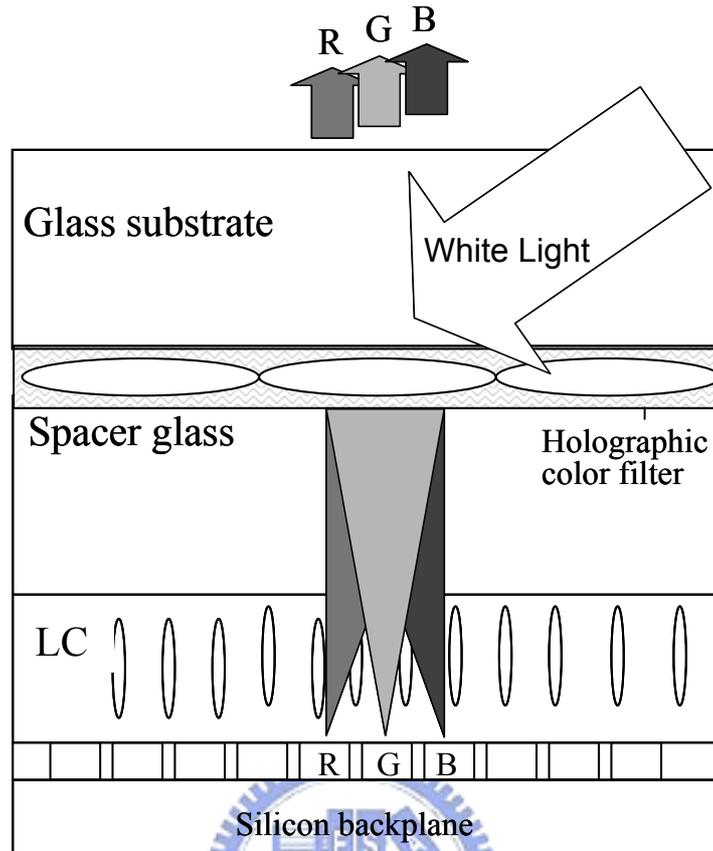


Figure 1.8 Single-panel LCOS system using holographic color filter.

## 1.2 The issues of LCOS projection displays

### 1.2.1 The issues of optical engines

There are different kinds of considerations for different optical engines. Basically, a lower f-number ( $F_{\#}$ ) is preferred because the light throughput is approximately inversely proportional to the square of  $F_{\#}$  [14]. However, the lower  $F_{\#}$  implies a larger incident angle which can cause depolarization when light passes through the PBS.

Typically, a PBS is formed utilizing the physical effect of Brewster angle reflection. Based on Fresnel's theory, the normalized reflectance of s-wave ( $R_s$ ) and p-wave ( $R_p$ ) when passing an interface between two media can be expressed as: [15]

$$R_s = \left( \frac{\cos\theta - \sqrt{n^2 - \sin^2\theta}}{\cos\theta + \sqrt{n^2 - \sin^2\theta}} \right)^2 \quad (1.1)$$

$$R_p = \left( \frac{n^2 \cos\theta - \sqrt{n^2 - \sin^2\theta}}{n^2 \cos\theta + \sqrt{n^2 - \sin^2\theta}} \right)^2 \quad (1.2)$$

where  $n$  is the relative index of refraction of the two media,  $\theta$  is the angle between the incident ray and the surface normal. The Brewster angle reflection occurs at the condition of  $\theta_B = \tan^{-1}n$ . At this condition, the reflected ray becomes linearly polarized with the electric vector transverse to the plane of incidence. The transmitted light is partially polarized as sketched in Fig. 1.9 (a). A calculated result of normalized reflectance with respect to the incident angle when light propagating from air to  $\text{Ti}_2\text{O}_3$  ( $n=2.45$ ) is shown in Fig. 1.9 (b). MacNeille and Banning enhanced this effect by increasing the number of interfaces at which reflection occurred using multiple layers of thin inorganic films [16]. Modern designs can reach over 99% reflectance of s-wave and over 95% of p-wave transmission.

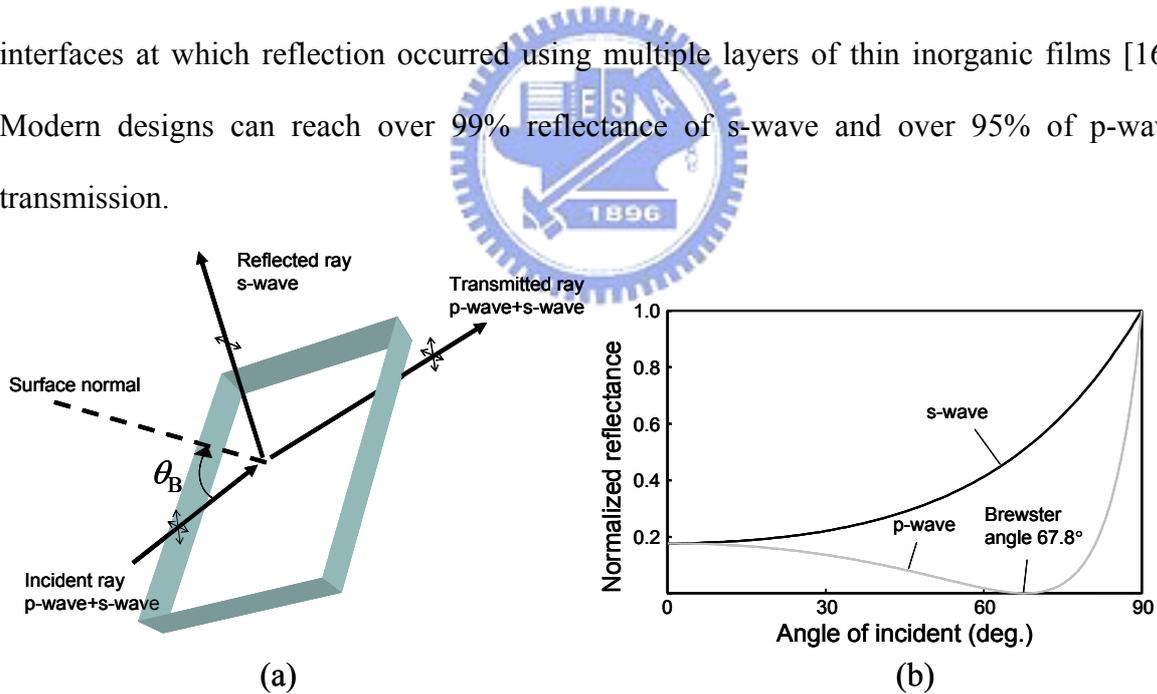


Figure 1.9 (a) Sketch of the Brewster angle reflection; (b) an calculated results of normalized reflectance with respect to incident angle when light propagating from air to  $\text{Ti}_2\text{O}_3$  ( $n=2.45$ ).

The weaknesses of the MacNeille PBS include sensitivity of transmission of p-wave and reflection of s-wave to the angle of incidence and wavelength [17]. The strong angular dependence of the reflectance can also be seen in Fig. 1.9 (b). For light with a small cone

angle, there can be a significant amount of p-wave in the reflected beam, leading to depolarization of light.

Alternatives for MacNeille PBS have been developed to earn allowance of angle deviations. These technologies include the wire-grid polarizer (WGP) [18], polymer multiple layer [19] and quarter-wave plate compensations [20]. Details of these technologies are beyond the scope of this thesis and will not be mentioned. Recently, WGPs have been employed in some high-end LCOS projection displays not only due to its stability over a great range of incident angle, but also because of its durability from thermal effect. Heat-induced problems could be significant owing to high light flux generated by UHP lamps.

## 1.2.2 The issues of LCOS panels

The demand of ever-increasingly high resolution of LCOS devices leads to a smaller pixel size. Recall that the pixel size can be as small as 5-8  $\mu\text{m}$  and the inter-pixel gaps are in sub-microns. However, several problems occur as the pixel size and the inter-pixel gaps are shrunk. For instance, the aperture ratio is decreased and the diffraction loss and fringe fields are both increased. How to maintain high brightness, high contrast ratio, high image sharpness and good dynamic response for a high-resolution LCOS projector is a challenging task.

Figure 1.10 sketches the fringing fields at the pixel edges when adjacent pixels operate at different voltages. As the inter-pixel gap is reduced, the lateral components of the fringing fields, generated by the voltage difference between the adjacent pixels, play a critical role in the optical performance. Different liquid crystal modes have different responses to these fringing fields. The influences of the fringing-field effect in different LC modes will be discussed in Chapter 3. Some other parameters of a LC cell, including the pretilt angle, cell thickness, electrode slopes and chiral dopant, are also related to this crucial effect.

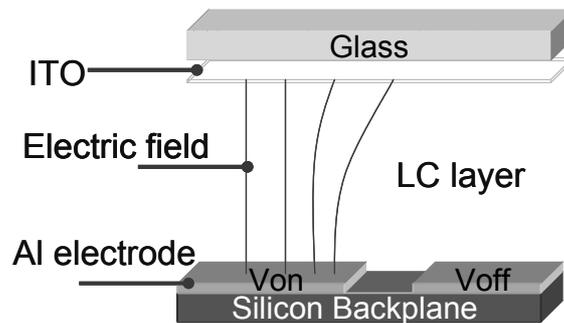


Figure 1.10 Sketch of the fringing fields at the pixel edges when adjacent pixels are operated at different voltages.

Another important effect generated from tiny pixel pitches is diffraction. The periodic pixel electrodes act as a reflective grating as the pixel pitches become comparable to wavelengths of visible light. Therefore, part of the reflected light is diffracted or scattered out of the projection system as sketched in Fig. 1.11. This intrinsic physical effect can cause significant light loss especially when a high-definition panel is employed. Detailed analyses of diffraction effect of LCOS devices will be introduced in Chap. 5.

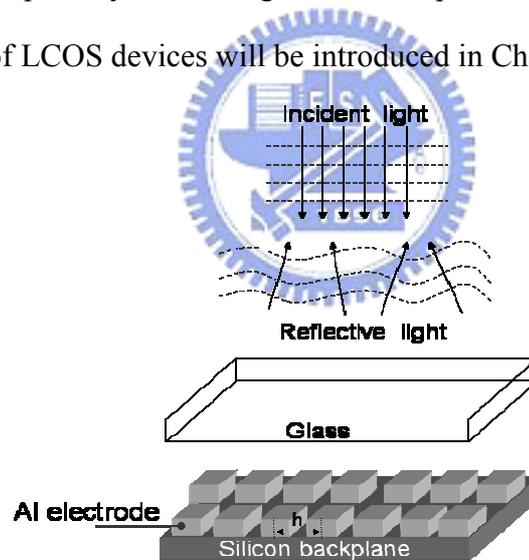


Figure 1.11 Sketch of the diffraction effect of LCOS devices.

### 1.3 Aims of the research

LCOS devices have great potential for microdisplay applications ranging from data projectors, large-screen rear-projection televisions (RPTVs) to near-to-eye (NTE) virtual projections devices. The major advantage of the single-crystalline silicon is the high electron mobility, which allows very small pixel structures to be fabricated on the silicon substrate. However, as we have mentioned, the fringing-field effect and the diffraction

effect are critical as the pixel pitch becomes too small. Efficiency can be decreased drastically due to diffraction loss. Fringing-field effects often cause poor image sharpness and degrade the dynamic response [21,22].

In this dissertation, we investigate the influences of fringing fields in different boundary conditions and distinct LC cell structures. Varying these parameters can give rise to different optical effects when light passes through the LC layer. Starting from understanding the LC director distributions under the influence of fringing fields, we are able to solve this long-standing problem. On the aspect of diffraction effect in high resolution LCOS devices, we developed an extended beam propagation method to simulate the optical performance of the devices when the pixel pitches become comparable to the visible wavelengths. By using this powerful tool, it is capable of designing a LCOS panel with least diffraction loss. In the followings, the basic theories and algorithm of simulations for LC director orientation and optical performances of LCOS devices are described in Chap. 2. Fringing-field effects in some commonly employed LC modes are investigated in Chap. 3. The influences of changing LC cell structure on fringing-field effect are also addressed in this chapter. In Chap. 4, we present a novel design called the circularly polarized light illuminated vertically aligned (CPVA) LCOS device which firstly eliminates the annoying fringing-field effect in vertically aligned (VA) LC mode. In Chap. 5, the analyses on diffraction effect of LCOS devices are studied by using BPM. A phase-compensated finger-on-plane mode is presented to save the light which is lost due to the strong diffraction in a conventional finger-on-plane LCOS device [22]. Finally, we summarize our work and make a brief conclusion. Suggestions are also given for future study.

## References

- [1] Y. Yamamoto, T. Morita, Y. Yamana, F. Funada and K. Awane. *Proc. 15<sup>th</sup> Intl. Research Conf. (Asia Display 95)*, pp.941 (1995).
- [2] J. R. Van Raalte, "A new schlieren light valve for television projection." *Applied Optics*, **9**, pp.2225 (1970).
- [3] P. M. Alt, "Single crystal silicon for high resolution displays." *Intl. Display Res. Conf. Record*, pp. M19-M22 (1997).
- [4] L. Arend, J. Lubin, J. Gille and J. Larimer, "Color breakup in sequential scanned LCDs." *Soc. Information Display Tech. Digest*, pp. 201 (1994).
- [5] E. Schnedler and H. von. Wijngaarde, "Ultrahigh-intensity short-arc long-life lamp system." *Soc. Information Display Tech. Digest*, paper 11.1, pp. 131 (1995).
- [6] A. H. J. van den Brandt, and W. A. G. Timmers, "Optical illumination system and projection apparatus comprising such a system." U.S. patent 5,098,184 (1992).
- [7] P. Michaloski and P. Tompkins, "Design and Analysis of illumination systems that use integrating rods or lens arrays. *Intl. Optical Design Conference Technical Digest*, pp-229 (1994).
- [8] Y. Itoh, J. I. Nakamura, K. Yoneno, H. Kamakura and N. Okamoto, "Ultra-high-efficiency LC projector using a polarized light illuminating system." *Soc. Information Display Tech. Digest*, pp. 993 (1997).
- [9] J. Rancourt, *Optical Thin-Films User Handbook* (SPIE press, 1996).
- [10] Unaxis Optics Inc., <http://optics.unaxis.com>.
- [11] M. D. Wand, W. N. Thurmes, R. T. Vohra, and K. M. More, "Advances in ferroelectric liquid crystals for microdisplay applications." *Soc. Information Display Tech. Digest*, pp. 157 (1996).
- [12] J. A. Shimizu, "Scrolling color LCOS for HDTV rear projection." *Soc. Information*

- Display Tech. Digest*, pp. 1072 (2001).
- [13] T. Yamazaki, M. Tokumi, T. Suzuki, S. Nakagaki and S. Shimizu, “The Single-Panel D-ILA Hologram Device for ILA™ Projection TV.” *Intl. Display Workshop*, pp. 1077 (2000).
- [14] M. L. Jepsen, M. J. Ammer, M. Bolotski, J. J. Drolet, A. Gupta, Y. Lai, D. Huffman, H. Shi and C. Vieri, “High resolution LCOS microdisplay for single-, double- or triple-panel projection systems.” *Displays* **23**, pp. 109 (2002).
- [15] G. R. Fowles, *Introduction to Modern Optics 2<sup>nd</sup> Edition* (Holt, Rinehart, and Winston, Inc., 1975).
- [16] S. M. MacNeille, “Beam Splitter.” U.S. patent 2,403,731 (1946).
- [17] E. H. Stupp and M. S. Brennesholtz, *Projection Displays* (John Wiley & Sons, 1999).
- [18] S. Arnold, E. Gardner, D. Hansen and R. Perkins, “An Improving Polarizing Beamsplitter LCOS Projection Display Based on Wire-Grid Polarizers.” *Soc. Information Display Tech. Digest*, pp. 1282 (2001).
- [19] M. F. Weber, C. A. Stover, L. R. Gilbert, T. J. Nevitt, and A. J. Ouderkirk, “Giant Birefringence Optics in Multilayer Polymer Mirrors.” *Science* **287**, pp.2451 (2000).
- [20] Y. Ji, J. Gandhi and M. Stefanov, *Soc. Information Display Tech. Digest*, pp.750 (1999).
- [21] S. Zhang, M. Lu, and K. H. Yang, *Soc. Information Display Tech. Digest*, pp.898 (2000).
- [22] W. Y. Chou, C. H. Hsu, S. W. Chang, H. C. Chiang and T. Y. Ho, *Jpn. J. Appl. Phys.* **41**, pp.7386 (2002).

# Chapter 2

## Theory and Numerical Simulation

### 2.1 Theories of deformations and optical properties of liquid crystals

To investigate the distributions of LC molecules under external fields, the continuum theory is often employed. It provides an insight of LC physic and was initiated by Oseen [1] and Zocher [2] back in 1933. Afterward, Frank had reexamined the theory critically and presented the theory of curvature elasticity [3]. With regard to the optical properties of nematic LCs, the optical rotation and birefringence effects are often induced. These phenomena had been studied by many authors, the most clear, rigorous and accessible reference being that of de Vries [4].

#### 2.1.1 Continuum theory of liquid crystals

Many important physical properties of LC can be explained by continuum theory disregarding the details of the structure on the molecular scale. When external fields are applied, the LC molecules are rotated according to the field strength; when the fields are withdrew, the LC molecules return back to their original alignments. This effect is similar to the elastic deformations in solids. Therefore, it can be predicted that the energy generated by the deformations of LC molecules has the same form as that described by Hooke's law.

LCs are either rod-like or disk-like molecules. In macroscopic point of view, LC molecules tend to align in a common direction, which is called "director"  $\mathbf{n}$ . The continuum theory describes the distortions of  $\mathbf{n}$  under some external forces. A good starting point is to explore the minimum energy condition. At first, some assumptions have to be addressed according to the characteristics of nematic:

1.  $\mathbf{n}$  is defined as a unit vector, i.e.  $\mathbf{n}\cdot\mathbf{n}=1$ .

2.  $\mathbf{n}$  and  $-\mathbf{n}$  are indistinguishable, i.e. there is no permanent dipole in nematic.
3. All properties are identical when the coordinate is rotated around  $\mathbf{n}$ , which is usually called  $C_\infty$  symmetry.
4. The reflective symmetry of the plane including  $\mathbf{n}$ . The properties of the system at two sides of the plane including  $\mathbf{n}$  are the same.

Despite the influence of the surface energies, the free energy density  $g_{lc}$  due to the distortion of  $\mathbf{n}$  can be expressed as:

$$g_{lc} = a_{ij} \mathbf{n}_{i,j} + a_{ijkl} \mathbf{n}_{i,j} \mathbf{n}_{k,l}, \quad (2.1)$$

where  $a_{ij}$  and  $a_{ijkl}$  are the constant coefficients depend on the material, and  $i, j, k, l = x, y, z$  which are the axes of a right-handed Cartesian coordinate system. This equation uses second-order approximation and omits the higher order terms. Based on the assumptions listed above, one can obtain a finally form of free energy density of a nematic as:

$$g_{lc} = \frac{1}{2} \left[ k_{11} (\nabla \cdot \mathbf{n})^2 + k_{22} (\mathbf{n} \cdot \nabla \times \mathbf{n})^2 + k_{33} (\mathbf{n} \times \nabla \times \mathbf{n})^2 \right], \quad (2.2)$$

where  $k_{ii}$ ,  $i=1, 2, 3$  are the elastic constants associated with three basic types of LC deformations, i.e. splay, twist and bend. It is shown in this equation that  $g=0$  when there is no deformation of  $\mathbf{n}$ . there

When nematic is doped with some chiral material, the LC directors present a helical structure as shown in Fig. 2.1.  $P_0$  denotes the natural pitch of the structure which represents the distance along the helical axis for the directors to rotate  $360^\circ$ . A right-handed twist structure gives a positive  $P_0$  and the left-handed twist structure gives a negative  $P_0$ . In this case, the fourth assumption is not satisfied. The orientations of LC directors are varied along the  $z$  axis in the natural balanced state. Therefore, an additional term must be added in Eq. (2.2) to interpret this phenomenon. The modified free energy density is given as:

$$g_{lc} = \frac{1}{2} \left[ k_{11} (\nabla \cdot \mathbf{n})^2 + k_{22} \left( \mathbf{n} \cdot \nabla \times \mathbf{n} + \frac{2\pi}{P_0} \right)^2 + k_{33} (\mathbf{n} \times \nabla \times \mathbf{n})^2 \right]. \quad (2.3)$$

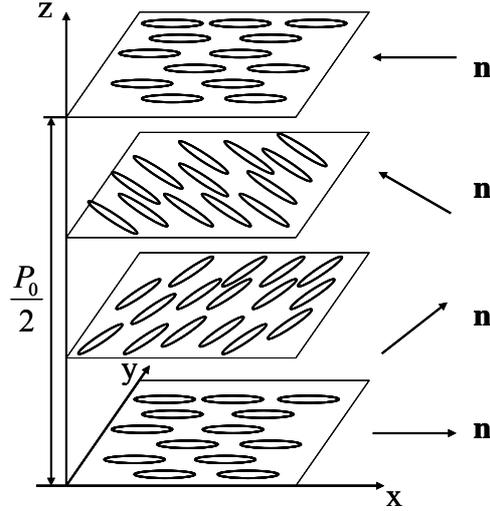


Figure 2.1 Structure of chiral nematic liquid crystals.  $P_0$  is the natural pitch.

### ***The effect of static electric field***

The influence of static electric field on nematic LC can be explored by understanding the anisotropy of its dielectric constant. Usually, the dielectric constant  $\epsilon$  can be expressed as a tensor:

$$\begin{aligned}\epsilon_{ij} &= \epsilon_{\perp} \delta_{ij} + \epsilon_a \mathbf{n}_i \mathbf{n}_j \\ \epsilon_a &= \epsilon_{//} - \epsilon_{\perp},\end{aligned}\tag{2.4}$$

where  $\delta_{ij}$  is Kronecker symbol ( $\delta_{ij}=1$  when  $i=j$ ; otherwise  $\delta_{ij}=0$ ;  $i, j=x, y, z$ ),  $\epsilon_{//}$  is the dielectric constant measured along  $\mathbf{n}$  and  $\epsilon_{\perp}$  is the dielectric constant measured perpendicular to  $\mathbf{n}$ . When external electric fields are applied on liquid crystal, the electric displacement  $\mathbf{D}$  can be given as:

$$\mathbf{D} = \epsilon_{\perp} \mathbf{E} + \epsilon_a (\mathbf{n} \cdot \mathbf{E}) \mathbf{n}.\tag{2.5}$$

Hence, the electric free energy  $g_e$  can be expressed as:

$$\begin{aligned}g_e &= \frac{1}{2} \mathbf{E} \cdot \mathbf{D} \\ &= \frac{1}{2} \left[ \epsilon_{\perp} \mathbf{E}^2 + \epsilon_a (\mathbf{n} \cdot \mathbf{E})^2 \right]\end{aligned}\tag{2.6}$$

Since the first term in Eq (2.6) is not related to the director distribution and introduce a constant value for the energy of the system, it can be ignored when deriving the minimum

energy condition. Therefore, the free energy density with external electric field can be expressed as:

$$\begin{aligned} \mathfrak{g}_{\text{tot}} &= \mathfrak{g}_{\text{lc}} - \mathfrak{g}_{\text{e}} \\ &= \frac{1}{2} \left[ k_{11} (\nabla \cdot \mathbf{n})^2 + k_{22} \left( \mathbf{n} \cdot \nabla \times \mathbf{n} + \frac{2\pi}{p_0} \right)^2 + k_{33} (\mathbf{n} \times \nabla \times \mathbf{n})^2 \right] - \frac{1}{2} \left[ \varepsilon_{\perp} \mathbf{E}^2 + \varepsilon_a (\mathbf{n} \cdot \mathbf{E})^2 \right] \end{aligned} \quad (2.7)$$

Note that this equation is under the assumption of strong boundary condition. For weak boundary condition, a surface energy term must be included. There are several various approaches [5-9], the details are beyond the scope of this thesis and will not be addressed.

### ***Euler-Lagrange equation***

To determine the director distribution, we have to minimize the energy generated by the LC deformations. For simplicity, we suppose that all parameters in Eq. (2.7) depend on z-direction only. Therefore, the total free energy is given as:

$$\begin{aligned} G_{\text{tot}} &= \int_{-d/2}^{d/2} \frac{1}{2} \left[ k_{11} (\nabla \cdot \mathbf{n})^2 + k_{22} \left( \mathbf{n} \cdot \nabla \times \mathbf{n} + \frac{2\pi}{p_0} \right)^2 + k_{33} (\mathbf{n} \times \nabla \times \mathbf{n})^2 \right] dz \\ &\quad - \int_{-d/2}^{d/2} \frac{1}{2} \left[ \varepsilon_{\perp} \mathbf{E}^2 + \varepsilon_a (\mathbf{n} \cdot \mathbf{E})^2 \right] dz \\ &= \int_{-d/2}^{d/2} \mathfrak{g}_{\text{tot}} \left( \mathbf{n}_i(z), \frac{d\mathbf{n}_i(z)}{dz}; z \right) dz, \end{aligned} \quad (2.8)$$

where  $i=x, y, z$  and  $d$  denotes the thickness of the LC layer. This is a function related to the integral path. Our purpose is to find a path,  $n_i(z)$ , from  $a$  to  $b$  which gives the minimum integral value  $G_m$ . In this case, an arbitrary path,  $n_i(z) + \alpha \delta n_i(z)$ , from  $a$  to  $b$  gives the value of  $G_{\text{tot}}$  as:

$$G_{\text{tot}}(\alpha) = \int_a^b \mathfrak{g}_{\text{tot}} \left( n_i(z) + \alpha \delta n_i(z), \frac{dn_i(z)}{dz} + \alpha \left( \frac{d \delta n_i(z)}{dz} \right) \right) dz, \quad (2.9)$$

where  $\alpha$  is a variable ranged from -1 to 1.  $G_{\text{tot}}(\alpha)$  is either larger or equal to  $G_m$ , which means:

$$\left. \frac{\partial}{\partial \alpha} G_{\text{tot}}(\alpha) \right|_{\alpha=0} = 0 \quad (2.10)$$

Hence,

$$\frac{\partial}{\partial \alpha} G_{\text{tot}}(\alpha) = \int_a^b \left[ \frac{\partial \mathbf{g}_{\text{tot}}}{\partial \mathbf{n}_i} \delta \mathbf{n}_i + \frac{\partial \mathbf{g}_{\text{tot}}}{\partial \left( \frac{d \mathbf{n}_i}{dz} \right)} \left( \frac{d \delta \mathbf{n}_i}{dz} \right) \right] dz = 0 \quad (2.11)$$

The second term in the integrand can be integrated by parts:

$$\int_a^b \frac{\partial \mathbf{g}_{\text{tot}}}{\partial \left( \frac{d \mathbf{n}_i}{dz} \right)} \left( \frac{d \delta \mathbf{n}_i}{dz} \right) dz = \frac{\partial \mathbf{g}_{\text{tot}}}{\partial \left( \frac{d \mathbf{n}_i}{dz} \right)} \delta \mathbf{n}_i \Big|_a^b - \int_a^b \frac{d}{dx} \left( \frac{\partial \mathbf{g}_{\text{tot}}}{\partial \left( \frac{d \mathbf{n}_i}{dz} \right)} \right) \delta \mathbf{n}_i dz \quad (2.12)$$

The integrated term vanishes because  $\delta \mathbf{n}_i(a) = \delta \mathbf{n}_i(b) = 0$ . Therefore, Eq. (2.11) becomes:

$$\begin{aligned} \frac{\partial}{\partial \alpha} G_{\text{tot}}(\alpha) &= \int_a^b \left[ \frac{\partial \mathbf{g}_{\text{tot}}}{\partial \mathbf{n}_i} \delta \mathbf{n}_i - \frac{d}{dx} \left( \frac{\partial \mathbf{g}_{\text{tot}}}{\partial \left( \frac{d \mathbf{n}_i}{dz} \right)} \right) \delta \mathbf{n}_i \right] dz \\ &= \int_a^b \left[ \frac{\partial \mathbf{g}_{\text{tot}}}{\partial \mathbf{n}_i} - \frac{d}{dx} \left( \frac{\partial \mathbf{g}_{\text{tot}}}{\partial \left( \frac{d \mathbf{n}_i}{dz} \right)} \right) \right] \delta \mathbf{n}_i dz \\ &= 0 \end{aligned} \quad (2.13)$$

Because  $\delta \mathbf{n}_i$  is an arbitrary function, the integrand in Eq. (2.13) must vanish itself:

$$\frac{\partial \mathbf{g}_{\text{tot}}}{\partial \mathbf{n}_i} - \frac{d}{dx} \left( \frac{\partial \mathbf{g}_{\text{tot}}}{\partial \left( \frac{d \mathbf{n}_i}{dz} \right)} \right) = 0 \quad (2.14)$$

This result is known as Euler-Lagrange equation which is commonly used for solving the static problems of LC director distribution.

## 2.1.2 Optical properties of an ideal helix: de Vries theory

As we mentioned previously, the LC directors present a helical structure when molecules possessing chirality are doped. The same structure is also found in pure cholesteric esters. Therefore, this helical structure is termed cholesteric. The general optical properties of an ideal cholesteric LCs (CLCs) contains many effects occurred in common LC devices [10,11]. The optical behaviors of light propagating in some commonly used LC modes, e.g. twisted nematic (TN), super-twisted nematic (STN) and homogenous, etc., are only the special cases of that in CLCs.

Let us recall the structure shown in Fig. 2.1. In this specific case,  $\mathbf{n}$  is rotated with a helix axis, i.e. the z-axis. We can describe  $\mathbf{n}$  in this ideal state as:

$$\begin{aligned} n_x &= \cos\phi \\ n_y &= \sin\phi \\ n_z &= 0 \\ \phi &= q_0z + \text{constant} \end{aligned} \tag{2.15}$$

where  $q_0=2\pi/P_0$ . In this configuration,  $\mathbf{n}$  is horizontal everywhere and it is usually called the “planar texture”. To analyze the optical properties of CLCs, the local dielectric constant at any point  $\mathbf{r}$  must be given at first:

$$\epsilon_{ij}(\mathbf{r}) = \epsilon_{\perp} \delta_{ij} + (\epsilon_{//} + \epsilon_{\perp}) n_i(\mathbf{r}) n_j(\mathbf{r}), \tag{2.16}$$

where  $i, j=x, y, z$ . It is noteworthy that although this equation looks the same as Eq. (2.5), the physical meanings are different. Eq. (2.16) accounts for the optical behaviors of light propagating inside a uniaxial material and Eq. (2.5) accounts for the anisotropy of electric properties with external fields. In Eq. (2.16), the dielectric constants can be related associated with the refraction indices as:

$$\epsilon_{\perp} = \epsilon_0 n_o^2, \quad \epsilon_{//} = \epsilon_0 n_e^2 \tag{2.17}$$

where  $\epsilon_0$  is the permittivity of vacuum,  $n_o$  is the ordinary refractive index of LC and  $n_e$  is the extraordinary refractive index of LC. When an electromagnetic wave of frequency ( $\omega$ )

propagates along the helix axis (i.e. the z-axis), the field components are:

$$\begin{pmatrix} E_x(zt) \\ E_y(zt) \end{pmatrix} = \text{Re} \begin{pmatrix} E_x(z)e^{-i\omega t} \\ E_y(z)e^{-i\omega t} \end{pmatrix} \quad (2.18)$$

where  $t$  represents time and  $\text{Re}$  stands for the real part. The electric field vectors must satisfy the well-known wave equation:

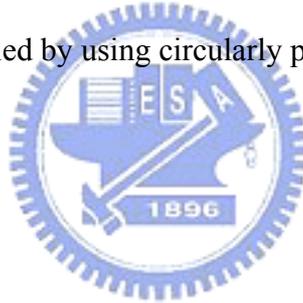
$$-\frac{d^2}{dz^2} \begin{pmatrix} E_x \\ E_y \end{pmatrix} = \left(\frac{\omega}{c}\right)^2 \varepsilon^*(z) \begin{pmatrix} E_x \\ E_y \end{pmatrix} \quad (2.19)$$

where  $c$  is the speed of light in vacuum and  $\varepsilon^*$  can be deduced from Eqs. (2.15) and (2.16) that:

$$\varepsilon^*(z) = \frac{\varepsilon_{//} + \varepsilon_{\perp}}{2} \begin{pmatrix} 1 & 0 \\ 0 & 1 \end{pmatrix} + \frac{\varepsilon_a}{2} \begin{pmatrix} \cos(2q_0 z) & \sin(2q_0 z) \\ \sin(2q_0 z) & -\cos(2q_0 z) \end{pmatrix} \quad (2.20)$$

The wave equation can be simplified by using circularly polarized light:

$$\begin{aligned} E^+ &= E_x + iE_y \\ E^- &= E_x - iE_y \end{aligned} \quad (2.21)$$



Hence, Eq. (2.19) becomes:

$$-\frac{d^2}{dz^2} \begin{pmatrix} E^+ \\ E^- \end{pmatrix} = \left(\frac{\omega}{c}\right)^2 \begin{pmatrix} k_0^2 & k_1^2 e^{2iq_0 z} \\ k_1^2 e^{-2iq_0 z} & k_0^2 \end{pmatrix} \begin{pmatrix} E^+ \\ E^- \end{pmatrix} \quad (2.22)$$

where

$$\begin{aligned} k_0^2 &= \left(\frac{\omega}{c}\right)^2 \frac{\varepsilon_{//} + \varepsilon_{\perp}}{2}, \\ k_1^2 &= \left(\frac{\omega}{c}\right)^2 \frac{\varepsilon_{//} - \varepsilon_{\perp}}{2} \end{aligned} \quad (2.23)$$

Solving Eq. (2.22) give the following forms of propagating waves:

$$\begin{aligned} E^+ &= ae^{i(l+q_0)z} \\ E^- &= be^{i(l-q_0)z} \end{aligned} \quad (2.24)$$

where  $a$  and  $b$  are constants. Substitute Eq. (2.24) into Eq. (2.22) gives the relations between the  $a$  and  $b$ :

$$\begin{aligned} [(1+q_0)^2 - k_0^2]a - k_1^2 b &= 0, \\ -k_1^2 a + [(1-q_0)^2 - k_0^2]b &= 0. \end{aligned} \quad (2.25)$$

The non-trivial solution of this equation is obtained only when the determinant vanishes:

$$(-k_0^2 + 1^2 + q_0^2)^2 - 4q_0^2 1^2 - k_1^4 = 0 \quad (2.26)$$

This equation gives the dispersion relation of CLCs, i.e. the relation between frequency  $\omega$  and wavenumber  $l$ . Figure 2.2 (a) shows a typical dispersion relation of CLCs with  $n_e=1.5578$ ,  $n_o=1.4748$  and  $P_0=0.25 \mu\text{m}$ . It is shown that the curve is separated into two branches by a band gap. The range of frequency of this band gap can be determined by setting  $l=0$  in Eq. (2.26):

$$k_0^2 - q_0^2 = \pm k_1^4 \quad (2.27)$$

Using Eq. (2.23), the boundaries of the band gap can be given as:

$$\omega_+(0) = \frac{c q_0}{n_o}, \quad \omega_-(0) = \frac{c q_0}{n_e} \quad (2.28)$$

where  $\omega_+(0)$  corresponds to the upper branch and  $\omega_-(0)$  corresponds to the lower branch.

For a incident wave with fixed  $\omega$ , we can have four eigenmodes. Two propagate along  $+z$  direction (transmissive modes) and two propagate along  $-z$  direction (reflective modes).

Here we focus on the transmissive modes, i. e.  $\partial\omega/\partial l > 0$ .

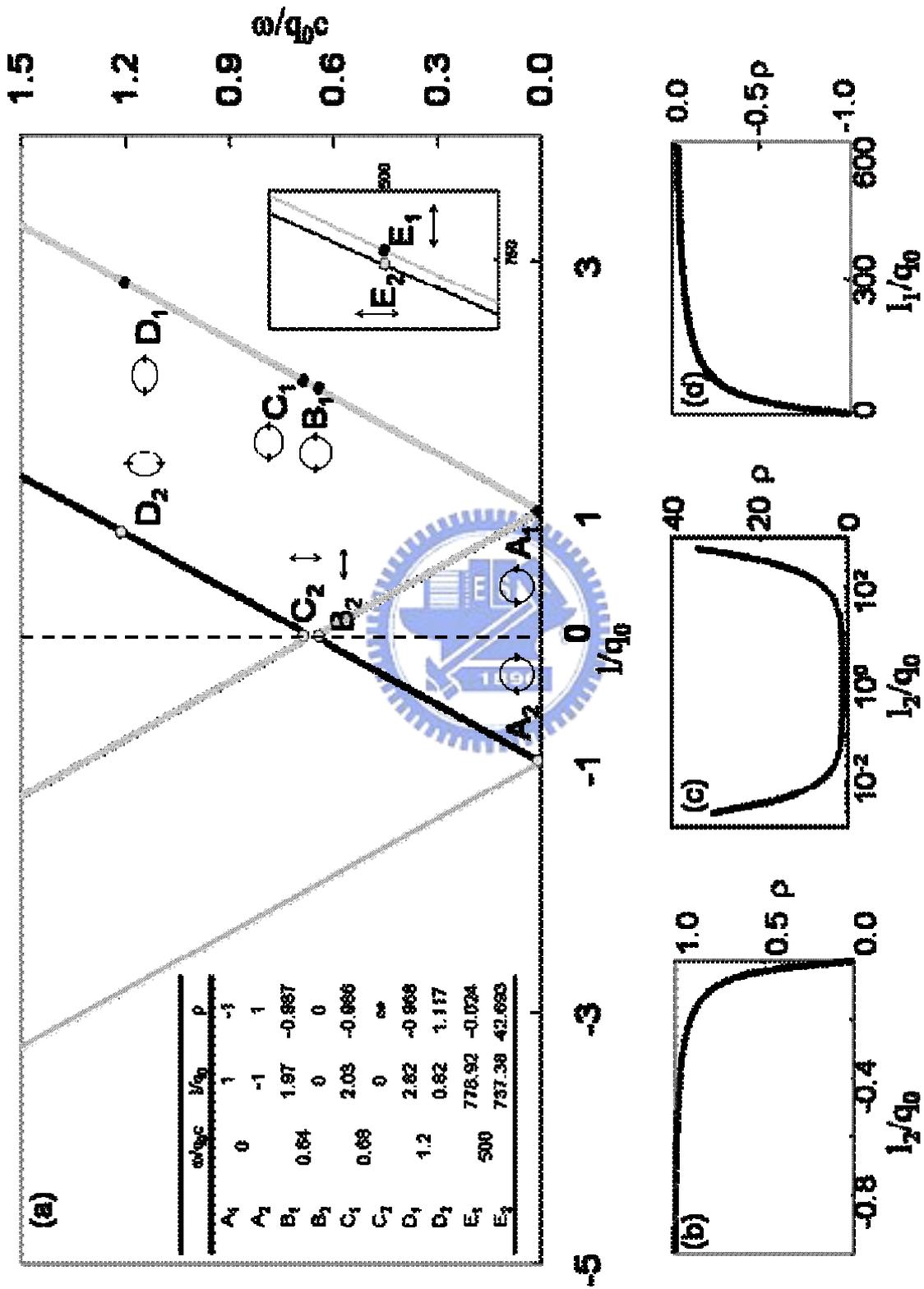


Figure 2.2 (a) The dispersion relation of a CLC with  $n_e=1.5578$ ,  $n_o=1.4748$  and  $P_{\bar{y}}=0.25 \mu\text{m}$ ; the insert denotes the characteristics of eigenmodes at some specific frequencies; (b) Calculated ellipticity with respect to  $l_2/q_0$  when  $-1 < l_2/q_0 < 0$ ; (c) Calculated ellipticity with respect to  $l_2/q_0$  when  $0 < l_2/q_0 < 10^{-3}$ ; (d) Calculated ellipticity with respect to  $l_1/q_0$  when  $0 < l_1/q_0 < 600$ .

The reflective modes have similar behaviors. The wavenumber of the modes can be derived from Eq. (2.26):

$$\begin{aligned} l_1(\omega)^2 &= (q_0^2 + k_0^2) + \sqrt{4k_0^2q_0^2 + k_1^4}, \\ l_2(\omega)^2 &= (q_0^2 + k_0^2) - \sqrt{4k_0^2q_0^2 + k_1^4}. \end{aligned} \quad (2.29)$$

The polarization states of the eigenmodes can be deduced using the definition of ellipticity:

$$\rho = \frac{a-b}{a+b}. \quad (2.30)$$

according to Eq. (2.25), we have

$$\frac{a}{b} = \frac{k_1^2}{(1+q_0)^2 - k_0^2} = \frac{(1-q_0)^2 - k_0^2}{k_1^2} \quad (2.31)$$

Therefore, Eq. (2.30) becomes

$$\begin{aligned} \rho &= \frac{k_1^2 - (1+q_0)^2 + k_0^2}{k_1^2 + (1+q_0)^2 - k_0^2} = \frac{[(1-q_0)^2 - k_0^2] - k_1^2}{(1-q_0)^2 - k_0^2 + k_1^2} \\ &= \frac{k_1^2 - (1+q_0)^2 + k_0^2 + [(1-q_0)^2 - k_0^2] - k_1^2}{k_1^2 + (1+q_0)^2 - k_0^2 + (1-q_0)^2 - k_0^2 + k_1^2} \\ &= \frac{2lq_0}{k_0^2 - l^2 - q_0^2 - k_1^2} \end{aligned} \quad (2.32)$$

By using Eq. (2.26), we can rewrite Eq. (2.32) as

$$\rho = \frac{2lq_0}{\pm s^2 - k_1^2} \quad (2.33)$$

where

$$s^2 = \sqrt{k_1^4 + 4q_0^2l^2} \quad (2.34)$$

The sign of  $s$  in Eq. (2.33) depends on the branch used for  $\omega(l)$  as shown in Fig. (2.2).

Using Eq. (2.33), we calculate the frequency-dependent ellipticities of the eigenmodes as shown in Fig. 2.2 (b)-(d). They can be roughly divided into three regimes:

1. Elliptical Regime:  $\omega > \omega \geq 0$  and  $2q_0c/\Delta n \gg \omega > \omega_+$ . There are two elliptical regimes separated by the band gap of Bragg reflection. The eigenmodes are elliptically polarized with opposite sense of handedness. For  $\omega=0$ , the ellipticities become  $\pm 1$ , which indicates the eigenmodes become circularly polarized in this particular case, i. e. denoted by  $A_1$

and  $A_2$  in Fig. 2.2 (a).

2. Bragg Regime:  $\omega_+ > \omega > \omega_-$ . In this regime,  $l_2$  is imaginary which indicates that the corresponding eigenmode becomes an evanescent wave. On the other hand, the eigenmode correspond to  $l_1$  has its ellipticity close to -1. Thus, the transmitted wave is almost (but not really) left-handed circularly polarized. Recall that  $P_0 = 0.25 \mu\text{m} > 0$  corresponds to a right-handed helix. Hence, it can be concluded that the transmitted wave is almost circularly polarized with opposite rotational sense to that of the helix structure, and the reflective wave will have its rotational sense identical to that of the helix structure. For an extreme case when  $n_e = n_o$ , the band gap shrinks to one frequency  $\omega = cq_0/n_o$ . The corresponding wavelength  $\lambda = n_o P_0$  is in agreement with the usual Bragg reflection condition. For the evanescent wave, the wavenumber can be expressed as:

$$l_2(\omega) = i\kappa = i \left[ \sqrt{4k_0^2 q_0^2 + k_1^4} - (q_0^2 + k_0^2) \right]^{\frac{1}{2}} \quad (2.35)$$

From Eq. (2.24), we have the field vector written as:

$$\begin{aligned} E^+ &= a e^{i(l_2 + q_0)z} = a e^{-\kappa z + i q_0 z} = A e^{i\phi_a} e^{-\kappa z + i q_0 z}, \\ E^- &= b e^{i(l_2 - q_0)z} = b e^{-\kappa z - i q_0 z} = B e^{i\phi_b} e^{-\kappa z - i q_0 z}. \end{aligned} \quad (2.36)$$

where  $a$  and  $b$  can be imaginary which are then expressed as real numbers,  $A$  and  $B$ , multiplied by phasors,  $\exp(i\phi_a)$  and  $\exp(i\phi_b)$ . Based on Eq. (2.25), we have

$$\begin{aligned} b &= \frac{(i\kappa + q_0)^2 - k_0^2}{k_1^2} a \\ &= \frac{(i\kappa + q_0)^2 - k_0^2}{k_1^2} (A \cos \phi_a + i A \sin \phi_a) \\ &= B \cos \phi_b + i B \sin \phi_b \end{aligned} \quad (2.37)$$

Therefore, we can derive the relationship between  $A$  and  $B$ , that is

$$\begin{aligned} \frac{B}{A} &= \frac{[q_0^2 - k_0^2 - \kappa^2] \cos \phi_a - 2\kappa q_0 A \sin \phi_a}{k_1^2 \cos \phi_b} \\ &= \frac{[q_0^2 - k_0^2 - \kappa^2] \sin \phi_a + 2\kappa q_0 A \cos \phi_a}{k_1^2 \sin \phi_b} \end{aligned} \quad (2.38)$$

When  $|A| = |B|$ , the light is linearly polarized. Otherwise, the light is in general

elliptically polarized. The angle between the long axis of polarization ellipse and the local director is  $(\phi_a - \phi_b)/2$ . From Eq. (2.38), the angle can be derived as:

$$\tan(\phi_b - \phi_a) = \frac{2\kappa q_0}{[q_0^2 - k_0^2 - \kappa^2]}. \quad (2.39)$$

Figure 2.3 shows the calculate  $B/A$  and  $\phi_b - \phi_a$  with respect to frequency. As shown in the Fig., the evanescent wave is linearly polarized. The vibration direction of electric field is varied from parallel to perpendicular to the local director  $\mathbf{n}$  when changing the frequency from  $\omega_-$  to  $\omega_+$ .

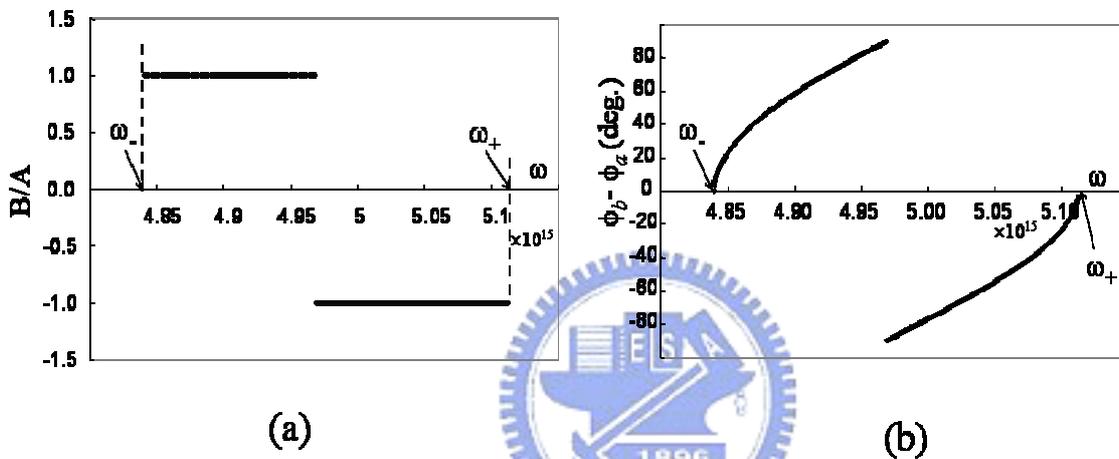


Fig. 2.3 The calculate (a)  $B/A$  and (b)  $\phi_b - \phi_a$  with respect to frequency.

3. Mauguin Regime:  $\omega \gg 2q_0c/\Delta n$ . In this high frequency regime, the eigenmodes have their ellipticities either near-zero or near-infinity, which means they are almost linear polarized parallel or perpendicular to the local LC director. As shown in the insert diagram of Fig. 2.2 (a), E1 and E2 indicate the case when  $\omega = 500q_0c$ , the ellipticities become -0.024 and 42.693.

Table 2.1 summarizes the properties of eigenmodes in each regimes.

Table 2.1 The properties of eigenmodes in each regimes.

$\omega$	$l_1(\omega) = \left[ (q_0^2 + k_0^2) + \sqrt{4k_0^2 q_0^2 + k_1^4} \right]^{1/2}$	$\rho_1(\omega) = \frac{2l_1 q_0}{-\sqrt{k_1^4 + 4q_0^2 l_1^2 - k_1^2}}$	$\text{Re}(l_2)$	$\rho_2$	Regime
$\omega \in \left[ \frac{\sqrt{2}q_0 c}{\Delta n}, \omega_+ \right]$	$A_1 \cdot l_1(0) = l_{A1} = +q_0,$ $l_1(\omega) \geq q_0 > 0.$	$\rho_1(0) = \rho_{A1} = -1,$ $0 > \rho_1(\omega) \sim -1.$	$-\left[ (q_0^2 + k_0^2) - \sqrt{4k_0^2 q_0^2 + k_1^4} \right]^{1/2}$ $A_2 \cdot l_2(0) = l_{A2} = -q_0,$ $0 > l_2(\omega) \geq -q_0.$	$\rho_2(\omega) = \frac{2l_2 q_0}{-\sqrt{k_1^4 + 4q_0^2 l_2^2 - k_1^2}}$ $\rho_2(0) = \rho_{A2} = 1,$ $1 \geq \rho_2(\omega) > 0.$	<b>Elliptical</b>
$\omega \in \left[ \omega_+, \frac{2q_0 c}{\Delta n} \right]$	$B_1 \cdot l_1(\omega_-) = l_{B1},$ $C_1 \cdot l_1(\omega_+) = l_{C1},$ $l_{C1} > l_{B1}.$	$\rho_1(\omega_-) = \rho_{B1},$ $\rho_1(\omega_+) = \rho_{C1},$ $0 > \rho_{C1} > \rho_{B1} > -1.$	$B_2 \cdot l_2(\omega_-) = 0,$ $C_2 \cdot l_2(\omega_+) = 0.$	$\rho_{B2}(\omega_-) = 0,$ $\rho_{C2}(\omega_+) = \infty.$	<b>Bragg</b>
$\frac{2q_0 c}{\Delta n} > \omega > \omega_+$	$D_1 \cdot l_1(\omega) = l_{D1},$ $l_{D1} > l_{C1}$	$0 > \rho_{D1} > \rho_{C1}$	$\left[ (q_0^2 + k_0^2) - \sqrt{4k_0^2 q_0^2 + k_1^4} \right]^{1/2}$ $D_2 \cdot l_2(\omega) = l_{D2},$ $l_{D2} > 0$	$\rho_2(\omega) = \frac{2l_2 q_0}{-\sqrt{k_1^4 + 4q_0^2 l_2^2 - k_1^2}}$ $\rho_{D2} > -1$	<b>Elliptical</b>
$\omega \in \left[ \frac{2q_0 c}{\Delta n}, \omega_+ \right]$	$E_1 \cdot l_1(\omega) = l_{E1},$ $l_{E1} > l_{D1}$	$\rho_{E1} \sim 0$	$E_1 \cdot l_2(\omega) = l_{E2},$ $l_{E2} > l_{D2}$	$\rho_{E2} \sim \infty$	<b>Mauguin</b>

## 2.2 Numerical Simulations

Numerical simulation is often utilized to analyze the performance of liquid crystal displays. To calculate the distribution of LC director, one can use Eq. (2.14) for searching the minimum energy condition once the initial and boundary conditions are given. In this case, the free energy density is expressed in vector-form as Eq. (2.7). Some literatures expressed the free energy density in tensor-form to maintain the equivalence of  $\mathbf{n}$  and  $-\mathbf{n}$  [12-14]. However, simulations using tensor-form was reported to cause transformations between topologically inequivalent states [15]. In view of this, the vector form is adopted in our research.

Two numerical methods are often employed, i.e. finite difference method [16] and finite element method [17]. In two dimensional (2D) simulations, finite difference method splits the simulated area into grids, which can be mismatched with boundaries of the area. This problem can be solved by using finite element method, which uses polygons to fit in the shapes of the area. In our simulations, a commercial software, 2dimMOS (from autronic-MELCHERS GmbH) [18], which uses finite element method is employed to calculate the director profile at first. The optical performance is then calculated by Jones matrix method or beam propagation method as will be introduced in the followings. The latter one includes the diffraction effect which may cause serious problem in LCOS projection system.

### 2.2.1 Jones matrix method

The most commonly used method to simulate the optical performance is the Jones matrix method [11,19]. Consider a plane wave propagates in a homogenous medium, its electric field is a function of space  $\mathbf{r}$  and time  $t$ , which can be written as:

$$\mathbf{E}(\mathbf{r}, t) = \mathbf{A}e^{i(\omega t - \mathbf{k} \cdot \mathbf{r} + \varphi)} \quad (2.40)$$

where  $\omega$  is the angular frequency,  $\mathbf{k}$  is the wavevector,  $\mathbf{A}$  is a constant vector and  $\varphi$  is the initial phase. Due to the nature of transverse waves, the electric field vector is always perpendicular to the direction of propagation. For a wave propagates along the z-direction, the field vectors can be written as:

$$\begin{aligned} E_x &= A_x \cos(\omega t - k_1 z + \varphi_x) \\ E_y &= A_y \cos(\omega t - k_2 z + \varphi_y) \end{aligned} \quad (2.41)$$

The phase difference between the x and y components are:

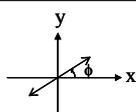
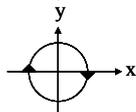
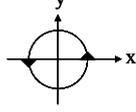
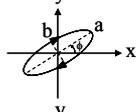
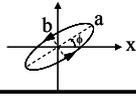
$$\delta = (\varphi_y - k_2 z) - (\varphi_x - k_1 z) = \varphi'_y - \varphi'_x \quad (2.42)$$

If we neglect the common parts related to time in Eq. (2.41), the field vectors can be expressed as a column vector named Jones vector:

$$\mathbf{J} = \begin{pmatrix} E_x \\ E_y \end{pmatrix} = \begin{pmatrix} A_x e^{i\varphi'_x} \\ A_y e^{i\varphi'_y} \end{pmatrix} = e^{i\varphi'_x} \begin{pmatrix} A_x \\ A_y e^{i\delta} \end{pmatrix} \quad (2.43)$$

Note that Jones vector is not a vector in real physical space; rather it is a vector in an abstract mathematical space which denotes the polarization state of light. Table 2.2 lists various polarization states represented by Jones vector.

Table. 2.2 Jones vectors corresponding to various polarization states.

Polarization State	Jones Vector
	$\begin{pmatrix} \cos \phi \\ \sin \phi \end{pmatrix}$
	$\frac{1}{\sqrt{2}} \begin{pmatrix} 1 \\ i \end{pmatrix}$
	$\frac{1}{\sqrt{2}} \begin{pmatrix} 1 \\ -i \end{pmatrix}$
	$\begin{pmatrix} a \cos \phi + ib \sin \phi \\ a \sin \phi - ib \cos \phi \end{pmatrix}$
	$\begin{pmatrix} a \cos \phi - ib \sin \phi \\ a \sin \phi + ib \cos \phi \end{pmatrix}$

When light propagates in a birefringence material, the field vector can be given as:

$$\begin{aligned} E_{x,out} &= E_{x,in} e^{-ik_0 n_e d} = E_{x,in} e^{i\varphi_e} \\ E_{y,out} &= E_{y,in} e^{-ik_0 n_o d} = E_{y,in} e^{i\varphi_o} \end{aligned} \quad (2.44)$$

where  $k_0$  represents the wavenumber in vacuum and  $d$  is the thickness of the material. Eq. (2.44) can be written in the matrix form as:

$$\begin{aligned} \begin{pmatrix} E_{x,out} \\ E_{y,out} \end{pmatrix} &= \begin{pmatrix} e^{-i\frac{2\pi}{\lambda} n_e d} & 0 \\ 0 & e^{-i\frac{2\pi}{\lambda} n_o d} \end{pmatrix} \begin{pmatrix} E_{x,in} \\ E_{y,in} \end{pmatrix} \\ &= \begin{pmatrix} e^{i\varphi_e} & 0 \\ 0 & e^{i\varphi_o} \end{pmatrix} \begin{pmatrix} E_{x,in} \\ E_{y,in} \end{pmatrix} \\ &= \mathbf{M} \begin{pmatrix} E_{x,in} \\ E_{y,in} \end{pmatrix} \end{aligned} \quad (2.45)$$

This is so-called the Jones matrix method. The Jones matrix,  $\mathbf{M}$ , is a  $2 \times 2$  transformation matrix, it characterizes the modulation of polarization state of a normally incident light.

When light propagates through a twisted nematic (TN) liquid crystal layer with twist angle  $\phi_t$  and phase difference  $\Gamma = k_0 d (n_{eff} - n_o)$ . In this condition, the local optical axis is a function of position. The represented Jones matrix can be derived by subdividing the LC layer into a large number,  $N$ , of thin layers as shown in Fig. 2.4. Each layer can be treated as a homogeneous wave plate. Assume the variations between the thin layers are linear, i.e. each sub-layer has a phase retardation of  $\Gamma/N$  and is oriented at azimuthal angle of  $\rho, 2\rho, 3\rho, \dots, (N-1)\rho, N\rho$  with  $\rho = \phi_t/N$ . Under this assumption, the Jones matrix of the  $n^{\text{th}}$  sub-layer is:

$$\mathbf{M}_n = \mathbf{R}(-n\rho) \cdot \begin{pmatrix} e^{-i\Gamma/2N} & 0 \\ 0 & e^{i\Gamma/2N} \end{pmatrix} \cdot \mathbf{R}(n\rho) \quad (2.46)$$

where  $\mathbf{R}$  represents the rotational matrix:

$$\mathbf{R}(\theta) = \begin{pmatrix} \cos \theta & \sin \theta \\ -\sin \theta & \cos \theta \end{pmatrix} \quad (2.47)$$

By multiplying all the sub-layer matrices together, we obtain

$$\begin{aligned}
M &= M_N \cdot M_{N-1} \cdot \dots \cdot M_3 \cdot M_2 \cdot M_1 \\
&= \prod_{n=1}^{n=N} \left[ R(-n\rho) \cdot \begin{pmatrix} e^{-i\Gamma/2N} & 0 \\ 0 & e^{i\Gamma/2N} \end{pmatrix} \cdot R(n\rho) \right] \\
&= R(-\phi_t) \cdot \left[ \begin{pmatrix} e^{-i\Gamma/2N} & 0 \\ 0 & e^{i\Gamma/2N} \end{pmatrix} \cdot R\left(\frac{\phi_t}{N}\right) \right]^N.
\end{aligned} \tag{2.48}$$

When  $N$  tends to infinite ( $N \rightarrow \infty$ ), by using Chebyshev's identity [20], the above equation can be further simplified to be

$$M = R(-\phi_t) \cdot \begin{pmatrix} \cos X - i \frac{\Gamma \sin X}{2 X} & \phi_t \frac{\sin X}{X} \\ -\phi_t \frac{\sin X}{X} & \cos X + i \frac{\Gamma \sin X}{2 X} \end{pmatrix} \tag{2.49}$$

where  $X = \sqrt{\phi_t^2 + \left(\frac{\Gamma}{2}\right)^2}$ .

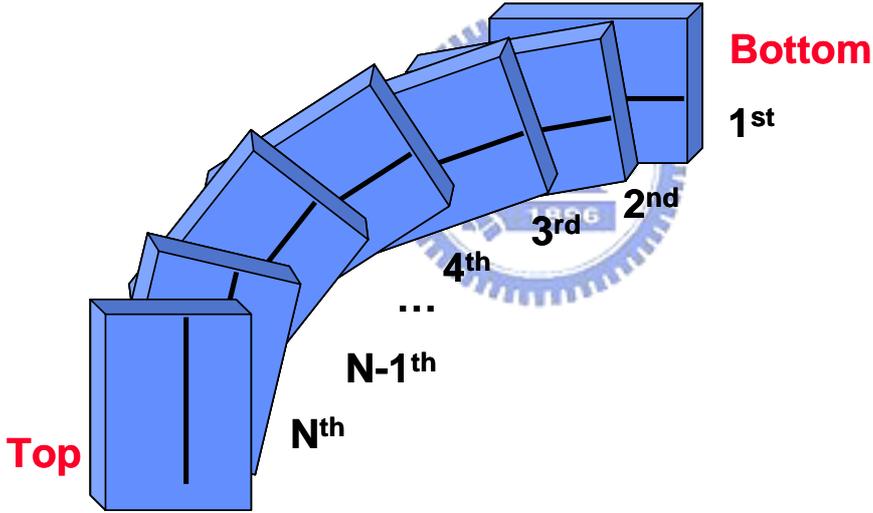


Fig. 2.4 The represented Jones matrix can be derived by subdividing the LC layer into a large number,  $N$ , of thin layers.

When the LC layer is sandwiched by two crossed polarizers, the output electric field can be given as:

$$E_{\text{out}} = \begin{pmatrix} -\sin \beta & \cos \beta \end{pmatrix} \cdot R(-\phi_t) \cdot \begin{pmatrix} \cos X - i \frac{\Gamma \sin X}{2 X} & \phi_t \frac{\sin X}{X} \\ -\phi_t \frac{\sin X}{X} & \cos X + i \frac{\Gamma \sin X}{2 X} \end{pmatrix} \begin{pmatrix} \cos \beta \\ \sin \beta \end{pmatrix} \tag{2.50}$$

where  $\beta$  is the angle between the transmission axis of linear polarizer and the entrance LC director. Finally, the normalized transmittance can be calculated as  $T_{\perp} = |E_{\text{out}}|^2$ .

For reflective LC device, the incident light passes through the LC layer twice. The director distribution encountered by reflective waves is the mirror image of the original one. For example, in Fig. 2.5, a reflective LC device with left-handed twist structure is equivalent to a transmissive LC layer with right-handed twist structure plus a transmissive LC layer with left-handed twist structure. The normalized reflectance can be expressed as [21]:

$$R_{//} = \left| (\cos \beta \quad \sin \beta) \begin{pmatrix} \cos X - i \frac{\Gamma \sin X}{2 X} & -\phi_t \frac{\sin X}{X} \\ \phi_t \frac{\sin X}{X} & \cos X + i \frac{\Gamma \sin X}{2 X} \end{pmatrix} \begin{pmatrix} \cos X - i \frac{\Gamma \sin X}{2 X} & \phi_t \frac{\sin X}{X} \\ -\phi_t \frac{\sin X}{X} & \cos X + i \frac{\Gamma \sin X}{2 X} \end{pmatrix} \begin{pmatrix} \cos \beta \\ \sin \beta \end{pmatrix} \right|^2 \quad (2.51)$$

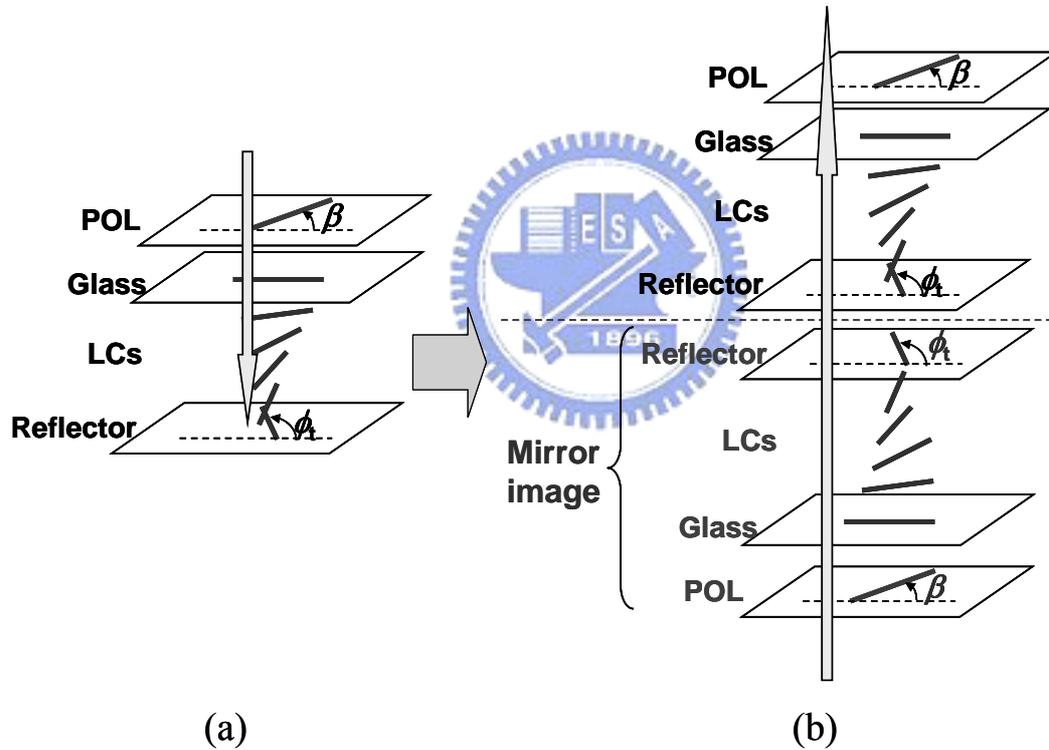


Fig. 2.5 Sketch of the mirror image of a left-handed twist LC cell.

In numerical calculations, the LC layer is divided into slabs. Each slab can be treated as an uniform TN cell. For LCOS system, PBS is employed to meet the crossed-polarizer condition as mentioned in Chap. 1. Some LC modes must include compensation films to optimize the optical performance. Eventually, Eq. (2.51) is modified to be

$$M = \begin{bmatrix} -\sin \beta & \cos \beta \end{bmatrix} J_F \prod_{n=N'}^1 \begin{bmatrix} \cos X_n - i \frac{\Gamma_n \sin X_n}{2 X_n} & -\phi_n \frac{\sin X_n}{X_n} \\ \phi_n \frac{\sin X_n}{X_n} & \cos X_n + i \frac{\Gamma_n \sin X_n}{2 X_n} \end{bmatrix} \prod_{n=1}^{N'} \begin{bmatrix} \cos X_n - i \frac{\Gamma_n \sin X_n}{2 X_n} & \phi_n \frac{\sin X_n}{X_n} \\ -\phi_n \frac{\sin X_n}{X_n} & \cos X_n + i \frac{\Gamma_n \sin X_n}{2 X_n} \end{bmatrix} J_F \begin{bmatrix} \cos \beta \\ \sin \beta \end{bmatrix}, \quad (2.52)$$

where

$$J_F = R(-\alpha) \begin{bmatrix} \exp(-i \frac{\delta}{2}) & 0 \\ 0 & \exp(i \frac{\delta}{2}) \end{bmatrix} R(\alpha) \quad (2.53)$$

is the Jones matrix of the compensation film,  $\alpha$  is the angle between optical axis of the compensation film and x-axis,  $\delta$  is the phase retardation of the compensation film, and  $\phi_n$  is the twist angle of the  $n^{\text{th}}$  slab.  $X_n = [\phi_n^2 + (\Gamma_n/2)^2]^{1/2}$  and  $\Gamma_n = \frac{2\pi d}{\lambda N} \Delta n$ , where  $d$  is the cell gap,  $\lambda$  is the wavelength, and  $\Delta n = n_e n_o / (n_o^2 \cos^2 \theta_t + n_e^2 \sin^2 \theta_t)^{1/2}$  is the effective birefringence related to the LC tilt angle  $\theta_t$  in the  $n^{\text{th}}$  slab.. All the angle definitions are illustrated in Fig. 2.6.

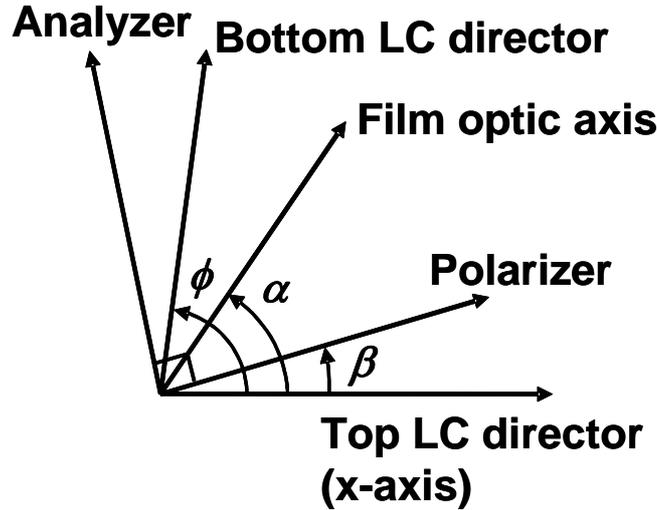


Fig. 2.6 The angle definitions in numerical calculations.

## 2.2.2 Beam propagation method

Jones matrix method mentioned above as well as other extended matrix-type solvers [22,23] are based on the assumption of a stratified medium. Fig. 2.7 (a) sketches the concept of these methods. As shown in the figure, the LC layer is divided into  $N \times M$  grids. Each grid is a slab of homogenous anisotropy material. Therefore, the light scattering and diffraction effects are excluded in these calculations. They are reliable only in the regime where the liquid crystal profiles are maintained uniformly over a scale far exceeding the optical wavelength.

In LCOS devices, the pixel pitches can be comparable to the wavelength, which means that the diffraction effect may have severe influences to the optical performance. The beam propagation method (BPM) has been proven useful in this condition [24,25]. This method is a numerical approach to the solution of Maxwell's curl equations. Unlike the matrix-type methods, the BPM considers the scattering and diffraction effects during the light propagation. Furthermore, the computational efficiency of BPM is much higher than that of the sophisticated finite-difference time domain (FDTD) method [26-28] and their results are almost identical when the liquid crystal (LC) layer is illuminated within  $\pm 30^\circ$  [25]. Fig. 2.7 (b) sketches the concepts of BPM. Basically, it develops an operational relationship between the field components at two planes separated by a sufficiently small propagation step  $\Delta z$ . The excitation field is propagated from the entrance to the exit plane by the repeated application of this operational relationship.

In this section, the concept and capabilities of BPM are reviewed.

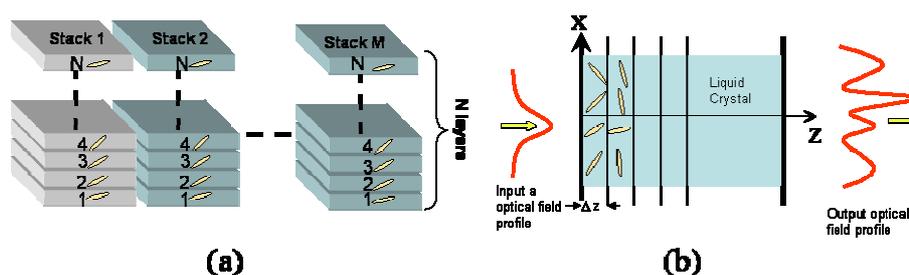


Fig. 2.7 Sketches of the concepts of the (a) Jones matrix method and (b) the beam propagation method.

## Scalar, Paraxial BPM

We firstly restrict the incident wave to be a scalar field. The wave equation can be given based on the well-known Helmholtz equation:

$$\frac{\partial^2 \Phi}{\partial x^2} + \frac{\partial^2 \Phi}{\partial y^2} + \frac{\partial^2 \Phi}{\partial z^2} + k(x, y, z)^2 \Phi = 0 \quad (2.54)$$

Here the scalar electric field is expressed as  $E(x, y, z, t) = \Phi(x, y, z)e^{-i\omega t}$  and  $k$  is the spatially dependent wavenumber. Other than the scalar assumption, this equation is exact. The field can be written as the product of a slowly varying envelope times a fast varying reference oscillating term:

$$\Phi(x, y, z) = u(x, y, z)e^{ik^*z} \quad (2.55)$$

where  $k^*$  is a constant to represent the average phase variation of the field  $\Phi$ , and is called the reference wavenumber. Inserting Eq. (2.55) into Eq. (2.54), we obtain

$$\frac{\partial^2 u}{\partial z^2} + 2ik^* \frac{\partial u}{\partial z} + \frac{\partial^2 u}{\partial x^2} + \frac{\partial^2 u}{\partial y^2} + (k^2 - k^{*2})u = 0 \quad (2.56)$$

Assuming the variation of  $u$  with  $z$  is sufficiently slow so that the first term in Eq. (2.56) can be neglected. It is also referred to as the paraxial approximation. Therefore, Eq. (2.56) can be rewritten as:

$$\frac{\partial u}{\partial z} = \frac{i}{2k^*} \left( \frac{\partial^2 u}{\partial x^2} + \frac{\partial^2 u}{\partial y^2} + (k^2 - k^{*2})u \right) \quad (2.57)$$

This is the basic three-dimensional (3D) BPM equation.

For numerical solution, the finite-difference approach based on the Crank-Nicholson scheme is often adopted [24]. The field in the transverse  $xy$  plane is represented at discrete points on discrete planes along the longitudinal or propagation direction, i.e.  $z$ -direction. The purpose is to derive the numerical equations that determine the field at the next  $z$  plane. For simplicity, the approach is limited in two-dimensional (2D) analyses, i.e. omitting the  $y$ -dependent term.

Let  $u_i^r$  denotes the field at transverse grid point  $i$  and longitudinal plane  $r$ . The grid points and planes are equally spaced by  $\Delta x$  and  $\Delta z$ , respectively. Eq. (2.57) can be written in the discrete form based on the Crank-Nicholson method:

$$\frac{u_i^{r+1} - u_i^r}{\Delta z} = \frac{i}{2k^*} \left( \frac{\delta^2}{\Delta x^2} + k_i^{r+1/2} - k^* \right) \frac{u_i^{r+1} + u_i^r}{2} \quad (2.58)$$

where  $\delta^2$  is the standard second-order difference operator,  $\delta^2 u_i = u_{i+1} + u_{i-1} - 2u_i$ . Eq. (2.58) can be rearranged into a standard tridiagonal matrix equation for the unknown field  $u_i^{r+1}$  in terms of known quantities as:

$$a_i u_{i-1}^{r+1} + b_i u_i^{r+1} + c_i u_{i+1}^{r+1} = d_i \quad (2.59)$$

where  $a$ ,  $b$ ,  $c$ , and  $d$  are known coefficients. Therefore, the solutions can be obtained by using the lower-upper (LU) decomposition [24].

### **Wide-Angle BPM**

The restriction of paraxiality on BPM is due to neglecting the  $\partial^2 u / \partial z^2$  term. If the  $\partial u / \partial z$  term is treated as a variable, one can obtain a first-order differential equation in  $z$  by solving Eq. (2.56):

$$\frac{\partial u}{\partial z} = ik^* (\sqrt{1+P} - 1)u, \quad (2.60)$$

$$P \equiv \frac{1}{k^*} \left( \frac{\partial^2}{\partial x^2} + \frac{\partial^2}{\partial y^2} + (k^2 - k^{*2}) \right).$$

This equation is exact that there is no paraxial approximation. However, the differential operator  $P$  in the radical introduces difficulties for solving the equation. To solve this problem, one approach is to use a Taylor expansion. Another method is to use Padé approximation which was reported to be more accurate than the Taylor expansion for the same order of terms [29]. Using Padé approximation, Eq. (2.60) can be modified as:

$$\frac{\partial u}{\partial z} = ik^* \frac{N_m(P)}{D_n(P)} u \quad (2.61)$$

where  $N_m$  and  $D_n$  are polynomials of  $P$ , and  $(m,n)$  is the order of approximation. The higher order it is, the more accurate result can be obtained in wide-angle problem. Table (2.3) lists

the first few terms of the Padé series.

Table 2.3 The first few terms of the Padé series.

Padé Order (m,n)	$N_m$	$D_m$
(1,0)	$P/2$	1
(1.1)	$P/2$	$1+P/4$
(2.2)	$P/2+ P^2/4$	$1+3P/4+P^2/16$

### ***Wide-Angle BPM for Liquid Crystal Device***

When light propagates in a liquid crystal device, the spatially dependent dielectric constant  $\varepsilon(x,z)$  can be written as a tensor:

$$\begin{aligned}
 \varepsilon(x, z) &= \begin{bmatrix} \varepsilon_{xx} & \varepsilon_{xy} & \varepsilon_{xz} \\ \varepsilon_{yx} & \varepsilon_{yy} & \varepsilon_{yz} \\ \varepsilon_{zx} & \varepsilon_{zy} & \varepsilon_{zz} \end{bmatrix} \\
 &= \varepsilon_0 \begin{bmatrix} n_o^2 + \Delta\varepsilon_r \cos^2 \theta \cos^2 \phi & \Delta\varepsilon_r \cos^2 \theta \sin \phi \cos \phi & \Delta\varepsilon_r \sin \theta \cos \theta \sin \phi \\ \Delta\varepsilon_r \cos^2 \theta \sin \phi \cos \phi & n_o^2 + \Delta\varepsilon_r \cos^2 \theta \cos^2 \phi & \Delta\varepsilon_r \sin \theta \cos \theta \cos \phi \\ \Delta\varepsilon_r \sin \theta \cos \theta \cos \phi & \Delta\varepsilon_r \sin \theta \cos \theta \sin \phi & n_o^2 + \Delta\varepsilon_r \sin^2 \theta \end{bmatrix} \\
 \Delta\varepsilon_r &= n_e^2 - n_o^2
 \end{aligned} \tag{2.62}$$

where  $\theta$  and  $\phi$  are the tilt and azimuthal angle of LC director, respectively. In this case, the scalar assumption in Eq. (2.54) is not appropriate for solving the wave equation. The polarization of light has to be included by recognizing that the electric and magnetic fields are vectors, i.e.  $\mathbf{E}=\mathbf{E}_x\mathbf{x}+\mathbf{E}_y\mathbf{y}+\mathbf{E}_z\mathbf{z}$  and  $\mathbf{H}=\mathbf{H}_x\mathbf{x}+\mathbf{H}_y\mathbf{y}+\mathbf{H}_z\mathbf{z}$ . From Maxwell's Equations, a set of coupled equations can be given as:

$$\frac{\partial^2 E_y}{\partial x^2} + \frac{\partial^2 E_y}{\partial z^2} + k_0^2 \left( \varepsilon_{yy} - \varepsilon_{yz} \frac{\tilde{b}}{\tilde{a}} - \varepsilon_{yx} \frac{\tilde{c}}{\tilde{a}} \right) E_y - \frac{j\omega\mu_0}{\tilde{a}} \left( \tilde{d} \frac{\partial H_y}{\partial x} - \tilde{e} \frac{\partial H_y}{\partial z} \right) = 0 \tag{2.63}$$

$$\begin{aligned}
& j\omega\epsilon_0 \left[ \frac{\partial}{\partial z} \left( \frac{c}{a} \right) - \frac{\partial}{\partial x} \left( \frac{b}{a} \right) \right] E_y + j\omega\epsilon_0 \left( \frac{c}{a} \frac{\partial E_y}{\partial z} - \frac{b}{a} \frac{\partial E_y}{\partial x} \right) + \frac{\epsilon_{xx}}{a} \frac{\partial^2 H_y}{\partial x^2} \\
& + \frac{\epsilon_{zz}}{a} \frac{\partial^2 H_y}{\partial z^2} + 2 \frac{\epsilon_{xz}}{a} \frac{\partial^2 H_y}{\partial x \partial z} + \left[ \frac{\partial}{\partial x} \left( \frac{\epsilon_{xx}}{a} \right) + \frac{\partial}{\partial z} \left( \frac{\epsilon_{xz}}{a} \right) \right] \frac{\partial H_y}{\partial x} + \\
& \left[ \frac{\partial}{\partial x} \left( \frac{\epsilon_{zx}}{a} \right) + \frac{\partial}{\partial z} \left( \frac{\epsilon_{zz}}{a} \right) \right] \frac{\partial H_y}{\partial z} + k_0^2 H_y = 0
\end{aligned} \tag{2.64}$$

where  $\mu_0$  is the permeability of vacuum and

$$\begin{aligned}
\tilde{a} &= \epsilon_{xx}\epsilon_{zz} - \epsilon_{zx}\epsilon_{xz}, \\
\tilde{b} &= \epsilon_{xx}\epsilon_{zy} - \epsilon_{zx}\epsilon_{xy}, \\
\tilde{c} &= \epsilon_{xy}\epsilon_{zz} - \epsilon_{zy}\epsilon_{xz}, \\
\tilde{d} &= \epsilon_{yz}\epsilon_{xx} - \epsilon_{yx}\epsilon_{xz}, \\
\tilde{e} &= \epsilon_{yx}\epsilon_{zz} - \epsilon_{yz}\epsilon_{zx}.
\end{aligned} \tag{2.65}$$

Under the slowly varying assumption, the field components can be written as:

$$\begin{aligned}
E_y(x, z) &= \mathcal{E}_y(x, z) \exp(-jk^*z), \\
H_y(x, z) &= \mathcal{H}_y(x, z) \exp(-jk^*z).
\end{aligned} \tag{2.66}$$

Substituting Eq. (2.66) in Eqs. (2.64) and (2.65), we have the following equations:

$$\begin{bmatrix} 1 & 0 \\ 0 & q \end{bmatrix} \frac{\partial^2}{\partial z^2} \begin{bmatrix} \mathcal{E}_y \\ \mathcal{H}_y \end{bmatrix} + \begin{bmatrix} R_{11} & R_{12} \\ R_{21} & R_{22} \end{bmatrix} + \begin{bmatrix} 0 & 0 \\ 0 & S_{22} \frac{\partial}{\partial x} \end{bmatrix} \left\{ \frac{\partial}{\partial z} \begin{bmatrix} \mathcal{E}_y \\ \mathcal{H}_y \end{bmatrix} \right\} + \begin{bmatrix} A_{11} & A_{12} \\ A_{21} & A_{22} \end{bmatrix} \begin{bmatrix} \mathcal{E}_y \\ \mathcal{H}_y \end{bmatrix} = 0$$

(2.67)

where

$$\begin{bmatrix} R_{11} & R_{12} \\ R_{21} & R_{22} \end{bmatrix} = \begin{bmatrix} -2jk^* & j\omega\mu_0 \frac{\tilde{e}}{a} \\ j\omega\epsilon_0 \frac{\tilde{c}}{a} & -2jk^* \frac{\epsilon_{zz}}{a} + \frac{\partial}{\partial x} \left( \frac{\epsilon_{zx}}{a} \right) + \frac{\partial}{\partial z} \left( \frac{\epsilon_{zz}}{a} \right) \end{bmatrix} \tag{2.68}$$

$$\begin{bmatrix} A_{11} & A_{12} \\ A_{21} & A_{22} \end{bmatrix} = \begin{bmatrix} P_{11} & P_{12} \\ P_{21} & P_{22} \end{bmatrix} \frac{\partial^2}{\partial x^2} + \begin{bmatrix} Q_{11} & Q_{12} \\ Q_{21} & Q_{22} \end{bmatrix} \frac{\partial}{\partial x} + \begin{bmatrix} T_{11} & T_{12} \\ T_{21} & T_{22} \end{bmatrix} \tag{2.69}$$

$$\begin{bmatrix} P_{11} & P_{12} \\ P_{21} & P_{22} \end{bmatrix} = \begin{bmatrix} 1 & 0 \\ 0 & \frac{\epsilon_{xx}}{a} \end{bmatrix} \tag{2.70}$$

$$\begin{bmatrix} Q_{11} & Q_{12} \\ Q_{21} & Q_{22} \end{bmatrix} = \begin{bmatrix} 0 & -j\omega\mu_0 \frac{\tilde{d}}{\tilde{a}} \\ -j\omega\varepsilon_0 \frac{\tilde{b}}{\tilde{a}} & -2jk^* \frac{\varepsilon_{xz}}{\tilde{a}} + \frac{\partial}{\partial x} \left( \frac{\varepsilon_{xx}}{\tilde{a}} \right) + \frac{\partial}{\partial z} \left( \frac{\varepsilon_{xz}}{\tilde{a}} \right) \end{bmatrix} \quad (2.71)$$

$$\begin{bmatrix} T_{11} & T_{12} \\ T_{21} & T_{22} \end{bmatrix} = \begin{bmatrix} k_0^2 \left( \varepsilon_{yy} - \varepsilon_{yz} \frac{\tilde{b}}{\tilde{a}} - \varepsilon_{yx} \frac{\tilde{c}}{\tilde{a}} \right) - k^{*2} & k^* \omega\mu_0 \frac{\tilde{e}}{\tilde{a}} \\ k^* \omega\varepsilon_0 \frac{\tilde{c}}{\tilde{a}} + j\omega\varepsilon_0 \left[ -\frac{\partial}{\partial x} \left( \frac{\tilde{b}}{\tilde{a}} \right) + \frac{\partial}{\partial z} \left( \frac{\tilde{c}}{\tilde{a}} \right) \right] & k_0^2 - \frac{\varepsilon_{zz}}{a} k^{*2} - jk^* \left[ \frac{\partial}{\partial x} \left( \frac{\varepsilon_{zx}}{\tilde{a}} \right) + \frac{\partial}{\partial z} \left( \frac{\varepsilon_{zz}}{\tilde{a}} \right) \right] \end{bmatrix} \quad (2.72)$$

$$q = \frac{\varepsilon_{zz}}{\tilde{a}} \quad (2.73)$$

$$S_{22} = 2 \frac{\varepsilon_{xz}}{\tilde{a}} \quad (2.74)$$

The wide-angle scheme can be formed by using the Padé recurrence relation as mentioned previously. From Eq. (2.67), we can have the following operational relation:

$$\frac{\partial}{\partial z} = - \frac{[A]}{\begin{bmatrix} 1 & 0 \\ 0 & q \end{bmatrix} \frac{\partial}{\partial z} + [R] + [S]} \quad (2.75)$$

This equation suggests the recurrence relation as:

$$\begin{aligned} \frac{\partial}{\partial z} \Big|_{n+1} &= - \frac{[A]}{\begin{bmatrix} 1 & 0 \\ 0 & q \end{bmatrix} \frac{\partial}{\partial z} \Big|_n + [R] + [S]}, \\ \frac{\partial}{\partial z} \Big|_0 &= 0. \end{aligned} \quad (2.76)$$

When setting  $n=0$ , Eq. (2.76) gives the result identical to that under paraxial assumption (i.e. the second-order differential term is omitted). When  $n=1$ , we have  $\partial/\partial z|_1 = -([R]+[S])^{-1}[A]$ . The contribution of matrix  $[S]$  is weak compared to  $[R]$  and is negligible in this case. Therefore, Eq. (2.67) can be expressed by

$$\left\{ [R] - \begin{bmatrix} 1 & 0 \\ 0 & q \end{bmatrix} [R]^{-1} [A] + [S] \right\} \frac{\partial}{\partial z} \begin{bmatrix} \mathcal{E}_y \\ \mathcal{H}_y \end{bmatrix} = -[A] \begin{bmatrix} \mathcal{E}_y \\ \mathcal{H}_y \end{bmatrix} \quad (2.77)$$

After applying the Crank-Nicolson finite-difference scheme with a weight parameter  $\alpha$

( $0.5 < \alpha < 1$ ), the discrete form of Eq. (2.77) is given as:

$$\begin{aligned} & \left\{ \left[ R^{r+1/2} \right] + \left[ S^{r+1/2} \right] + \left[ C^{r+1/2}(\alpha) \left[ A^{r+1/2} \right] \right\} \begin{bmatrix} \mathcal{E}_y^{r+1/2} \\ \mathcal{H}_y^{r+1/2} \end{bmatrix} \\ & = \left\{ \left[ R^{r+1/2} \right] + \left[ S^{r+1/2} \right] + \left[ C^{r+1/2}(\alpha - 1) \left[ A^{r+1/2} \right] \right\} \begin{bmatrix} \mathcal{E}_y^{r+1/2} \\ \mathcal{H}_y^{r+1/2} \end{bmatrix} \end{aligned} \quad (2.78)$$

where

$$[C(\alpha)] = \begin{bmatrix} \alpha \Delta z - \frac{1}{|R|} R_{22} & \frac{1}{|R|} R_{22} \\ \frac{q}{|R|} R_{21} & \alpha \Delta z - \frac{q}{|R|} R_{11} \end{bmatrix}. \quad (2.79)$$

and superscript  $r=1, 2, \dots, n$  indicates the propagation step of the discretized axial plane, i.e.,  $z=r\Delta z$  assuming that  $z$  is the propagation direction of the light. By unfolding Eq. (2.78), a sparse linear system can be formed to represent the relation between the known value of  $\mathcal{E}_y^r$ ,  $\mathcal{H}_y^r$  and the unknown value  $\mathcal{E}_y^{r+1}$ ,  $\mathcal{H}_y^{r+1}$ . In order to prevent artificial reflections from the boundary, transparent boundary condition (TBC) is utilized to ensure that the outgoing radiation passes through the boundary freely [30]. Finally, the following sparse linear system can be expressed as followed:

$$\begin{bmatrix} [X_{11}(\theta, \phi)] & [X_{12}(\theta, \phi)] \\ [X_{21}(\theta, \phi)] & [X_{22}(\theta, \phi)] \end{bmatrix} \begin{bmatrix} \mathcal{E}_y^{r+1/2} \\ \mathcal{H}_y^{r+1/2} \end{bmatrix} = \begin{bmatrix} [B_1(\mathcal{E}_y^r, \mathcal{H}_y^r)] \\ [B_2(\mathcal{E}_y^r, \mathcal{H}_y^r)] \end{bmatrix}. \quad (2.80)$$

Each of the sub-blocks  $[X_{i,j}]$  with  $i,j=1,2$  corresponds to a tridiagonal matrix. Both  $B_1$  and  $B_2$  are functions related to  $\mathcal{E}_y^r$  and  $\mathcal{H}_y^r$ . By solving Eq. (2.80) with an initial condition of a plane wave propagating along the  $z$  direction, we can obtain information that includes the amplitude and phase of the propagating light wave. The incident angle  $\theta_i$  can be changed by modifying the initial condition, that is

$$\begin{aligned} \mathcal{E}_y(x,0) &= \mathcal{E}_y(0,0) \exp[-jk_0 x \sin(\theta_i)] \\ \mathcal{H}_y(x,0) &= \mathcal{H}_y(0,0) \exp[-jk_0 x \sin(\theta_i)] \end{aligned} \quad (2.81)$$

## Extended Wide-Angle BPM for Reflective Liquid Crystal Devices

The reflective propagation process of the light wave can be derived by sending the light into the mirror image of the LC molecular distribution, as shown in Fig. 2.5. Therefore, the reflective transverse fields,  $\mathcal{E}'_y$  and  $\mathcal{H}'_y$ , of the LCOS device can be described as follows:

$$\begin{aligned}\mathcal{E}'_y{}^1 &= R_{g,p} \times \mathcal{E}_y^n \\ \mathcal{H}'_y{}^1 &= R_{g,p} \times \mathcal{H}_y^n\end{aligned}\quad (2.82a)$$

$$\begin{bmatrix} [X_{11}(-\theta, \phi)] & [X_{12}(-\theta, \phi)] \\ [X_{21}(-\theta, \phi)] & [X_{22}(-\theta, \phi)] \end{bmatrix} \begin{bmatrix} [\mathcal{E}'_y{}^{r+1}] \\ [[\mathcal{H}'_y{}^{r+1}]] \end{bmatrix} = \begin{bmatrix} [I_3([\mathcal{E}'_y{}^r, \mathcal{H}'_y{}^r])] \\ [I_4([\mathcal{E}'_y{}^r, \mathcal{H}'_y{}^r])] \end{bmatrix}, \quad (2.82b)$$

where  $R_p$  and  $R_g$  represent the reflectance of the reflective pixels and the interpixel gap, respectively. From Eq. (1), we obtain

$$-\frac{\partial \mathcal{H}'_y}{\partial z} = j\omega\epsilon_0(\epsilon_{xx}\mathcal{E}'_x + \epsilon_{xy}\mathcal{E}'_y + \epsilon_{xz}\mathcal{E}'_z) \quad (2.83a)$$

$$\frac{\partial \mathcal{H}'_y}{\partial x} = j\omega\epsilon_0(\epsilon_{zx}\mathcal{E}'_x + \epsilon_{zy}\mathcal{E}'_y + \epsilon_{zz}\mathcal{E}'_z). \quad (2.83b)$$

The reflected fields polarized in the x and z directions (i.e.,  $\mathcal{E}'_x$  and  $\mathcal{E}'_z$ ) can be derived from Eqs. (2.83a) and (2.83b):

$$\mathcal{E}'_x = -\frac{1}{j\omega\epsilon_0\tilde{a}} \left( \epsilon_{zz}^* \frac{\partial \mathcal{H}'_y}{\partial z} + \epsilon_{xz}^* \frac{\partial \mathcal{H}'_y}{\partial x} \right) - \frac{\tilde{c}}{\tilde{a}} \mathcal{E}'_y, \quad (2.84a)$$

$$\mathcal{E}'_z = \frac{1}{j\omega\epsilon_0\tilde{a}} \left( \epsilon_{xx}^* \frac{\partial \mathcal{H}'_y}{\partial x} + \epsilon_{zx}^* \frac{\partial \mathcal{H}'_y}{\partial z} \right) - \frac{\tilde{b}}{\tilde{a}} \mathcal{E}'_y. \quad (2.84b)$$

So far we have obtained the information of all the components of the reflective wave. Further analyses on 2D reflectance profile and angular spectrum can be given as will be mentioned in Chapter 5.

## References

- [1] C. W. Oseen, "The theory of liquid crystals." *Trans. Faraday Soc.*, **29**, pp.883 (1933).
- [2] H. Zocher, "The theory of liquid crystals." *Trans. Faraday Soc.*, **29**, pp.945 (1933).
- [3] F. C. Frank, "Liquid Crystals: On the theory of liquid crystals." *Discuss Faraday Soc.*, **25**, pp.19 (1958).
- [4] H. de Vries, *Acta Crystallogr.*, **4**, pp.219 (1951).
- [5] A. Rapini and M. Papoular, *J. Phys.* **30** C4-54 (1969).
- [6] K. H. Yang, *Appl. Phys. Lett.*, **43**, pp.171 (1983).
- [7] A. Sugimura and G. R. Luckhurst, *Phys. Rev. E* **52**, 681 (1995).
- [8] W. Zhao, C.-X. Wu and M. Iwamoto, *Phys. Rev. E* **62**, R1481 (2000).
- [9] O. K. C. Tsui, F. K. Lee, B. Zhang and P. Sheng, *Phys. Rev. E* **69**, 021704 (2004).
- [10] P. G. de Gennes and J. Prost. *The Physics of Liquid Crystals 2<sup>nd</sup> Edition* (Clarendon Press, 1993).
- [11] P. Yeh and C. Gu, *Optics of Liquid Crystal Displays* (John Wiley & Sons, 1999).
- [12] D. Berreman and S. Meiboom, "Tensor representation of Oseen-Frank strain energy in uniaxial cholesterics." *Physical Review A* **30**, pp.1955 (1984).
- [13] G. Haas, M. Fritsch, H. Wöhler and D. Mlynski, "Simulation of Reverse-Tilt Disclinations in LCDs." *Soc. Information Display Tech. Digest*, pp.102 (1990).
- [14] S. Dickmann, J. Eschler, O. Cossalter and D. Mlynski, "Simulation of LCDs Including Elastic Anisotropy and Inhomogeneous Fields." *Soc. Information Display Tech. Digest*, pp. 638 (1993).
- [15] J. E. Anderson, P. E. Watson and P.J. Bos, "Shortcomings of the Q Tensor Method for Modelling Liquid Crystal Devices." *Soc. Information Display Tech. Digest*, paper 16.3 (1999).
- [16] J. E. Anderson, P. E. Watson and P.J. Bos, *LC3D Liquid Crystal Display 3-D Director*

*Simulation Software and Technology Guide* (Artech House, Boston, 2001).

- [17] J. Jin, *The Finite Element Method in Electromagnetics 2<sup>nd</sup> Edition*, (John Wiley & Sons, New York, 2002).
- [18] autronic-MELCHERS GmbH, <http://www.autronic-melchers.com>.
- [19] R. C. Jones, *J. Opt. Soc. A.* **31**, pp.488 (1941).
- [20] A. Yariv and P. Yeh, *Optical Waves in Crystals* (Wiley, 1984).
- [21] S. T. Wu and D. K. Yang, *Reflective Liquid Crystal Displays* (Wiley-SID, New York, 2001).
- [22] D. W. Berreman, *J. Opt. Soc. Am.* **62**, pp.502 (1972).
- [23] A. Lien: *Appl. Phys. Lett.* **57**, pp.2767 (1990).
- [24] E. E. Kriezis and S. J. Elston: *J. Mod. Opt.* **46**, pp.1201 (1999).
- [25] E. E. Kriezis and S. J. Elston: *Appl. Opt.* **39**, pp.5707 (2000).
- [26] B. Witzigmann, P. Regli and W. Fichtner: *J. Opt. Soc. Am. A* **15**, pp.753 (1998).
- [27] E. E. Kriezis and S. J. Elston: *Opt. Commun.* **165**, pp.99 (1999).
- [28] E. E. Kriezis and S. J. Elston: *Opt. Commun.* **177** pp.69 (2000).
- [29] G. R. Hadley, *Opt. Lett.* **17**, pp.1426 (1992).
- [30] G. R. Hadley: *IEEE J. Quantum Electron.* **28** pp.363 (1992).

# Chapter 3

## Fringing-Field Effects of LCOS Devices

### 3.1 Introduction

As mentioned in Chapter 1, the fringing fields generated by voltage difference between neighboring pixels are critical to the optical performance of LCOS devices. Many parameters of LC cell are influential to the fringing-field-effect. In this chapter, we present detailed analyses of liquid crystal panels in various molecular alignment conditions, polarizer angles, and LC phase retardation values. These parameters determine the optical mechanisms employed, including birefringence effect and polarization rotation effect. The LC operation modes can be classified as twisted and non-twisted modes depending on their initial director profile. Here in the twisted category, the commonly employed mixed-mode twist nematic (MTN) [1] and the twist nematic (TN) modes [2] are studied, while in the non-twisted category we analyze the film-compensated homogenous (FCH) [3] and vertically aligned (VA) modes [4]. The influence of cell structures including the effects of electrode slope, cell thickness and pixel pitch are also compared. Furthermore, the fringing-field induced distortions of LC directors may cause delay in moving images. The dynamic behaviors of LCOS panel when switched from the dark-bright-dark state to the all-bright pixel configuration are discussed in the last part of this chapter.

### 3.2 Liquid crystal operation modes

In this section, we simulate the static electro-optical properties in eight LC operation modes. Figure 3.1 shows the cell structure used for the two-dimensional simulations of the LC director distributions and light efficiency. The cell gap is adjusted to obtain the required  $d\Delta n$  for each mode, where  $d$  is the cell gap and  $\Delta n$  is the LC birefringence. The pixel size is  $15\ \mu\text{m}$  and the inter-pixel gap is  $0.9\ \mu\text{m}$ . A passivation layer is deposited on the Al electrode

for protection and leveling the inter-pixel gap. The LC director orientations are calculated by the commercial software 2dimMOS. Afterwards, the voltage-dependent reflectance is obtained by Jones matrix method with the mirror image of the director profiles. Here, we assume that the reflectance of the reflective pixels (Rp) and the inter-pixel gap (Rg) are 1 and 0, respectively. The LC parameters used for simulations are listed in Table 3.1.

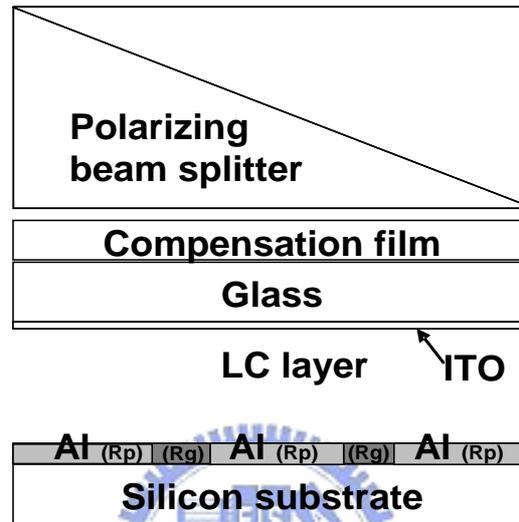


Fig. 3.1 The LC cell structure used for the two-dimensional simulations.

Table. 3.1 The LC parameters used for the simulations.

	Mixed-mode twist nematic (MTN)	Twist nematic mode (TN)	Vertically aligned mode (VA)	Film-compensated homogenous aligned mode (FCH)
$K_{11}$	13.1	13.9	16.7	13.4
$K_{22}$	10	10	7	6
$K_{33}$	22.3	21.5	18.1	19
$n_e$	1.5931	1.5604	1.5578	1.626
$n_o$	1.4865	1.4758	1.4748	1.499
$\epsilon_{//}$	10.1	10.5	3.6	10.5
$\epsilon_{\perp}$	3.3	3.5	7.8	3.6

### 3.2.1 Twisted LC modes

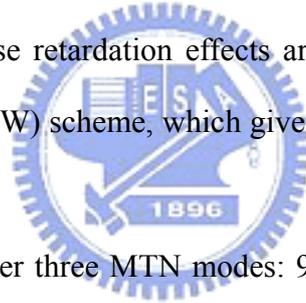
For a twisted LC cell with a large value of phase retardation  $d\Delta n$  compare to the wavelength  $\lambda$ , the Mauguin's condition as mentioned in Chap. 2 can be satisfied, that is

$$d\Delta n \gg \lambda; d = \phi / q_0,$$

$$\omega \gg 2\pi q_0 c / (\phi_i \Delta n) \gg 2q_0 c / \Delta n,$$

where  $\phi_t$  is the twist angle. Thus, the eignemodes are linearly polarized light which follow the twist of the LC directors reasonably well. This is so-called the polarization rotation effect, which is commonly utilized in TN-LCDs. When  $d\Delta n$  becomes smaller, the polarization rotation effect is incomplete and the phase retardation effect must be imposed to enhance the light modulation efficiency. Base on the light modulation mechanism, the twisted LC operation modes can be subdivided into two categories [5]:

- (1) TN modes. In these modes, the  $d\Delta n$  values are large and the angle  $\beta$  (referring to Fig. 2.6) is normally zero. Therefore, the corresponding light modulation mechanism in such cells is polarization rotation effect. TN modes are often operated at normally black (NB) scheme, which gives a dark state when no voltage is applied on the panel.
- (2) MTN modes. The  $d\Delta n$  values in such cells are smaller and usually  $\beta \neq 0$ . Both polarization rotation and phase retardation effects are present. MTN modes are often operated at normally white (NW) scheme, which gives a bright state when no voltage is applied on the panel.



In the followings, we will consider three MTN modes: 90°-MTN [1,6], film-compensated 63.6°-MTN [7], and film-compensated 45°-MTN [8]; three TN modes: 63.6°-TN [9], 45°-TN [10] and 52°-TN [11].

### **3.2.1.1 Mixed-mode twisted nematic (MTN)**

#### ***NW 90°-MTN Mode***

This mode has twist angle  $\phi_t=90^\circ$  and  $\beta=20^\circ$ . The required phase retardation  $d\Delta n$  is about 240 nm for normally white operation. Figure 3.2 (a) shows the one-dimensional (1D) simulation results on the voltage-dependent normalized reflectance using broadband red (R:620-680 nm), green (G:520-560 nm) and blue (B:420-480 nm) lights. As shown in the figure, the maximum reflectance of this mode is only about 88%. Based on the curve, we let the turned-on voltage ( $V_{on}$ ) to be 5 volts and the turned-off voltage ( $V_{off}$ ) to be 0.7 volts.

Figure 3.2 (b) shows the calculated iso-contrast contour viewing diagram for the broadband green channel. The polar angle corresponding to 1000:1 contrast ratio exceeds  $8^\circ$ . Although the property of viewing angle is less critical in projection displays, a wide acceptance angle allows a small F-number projection lens to be used which greatly improves the display brightness [12].

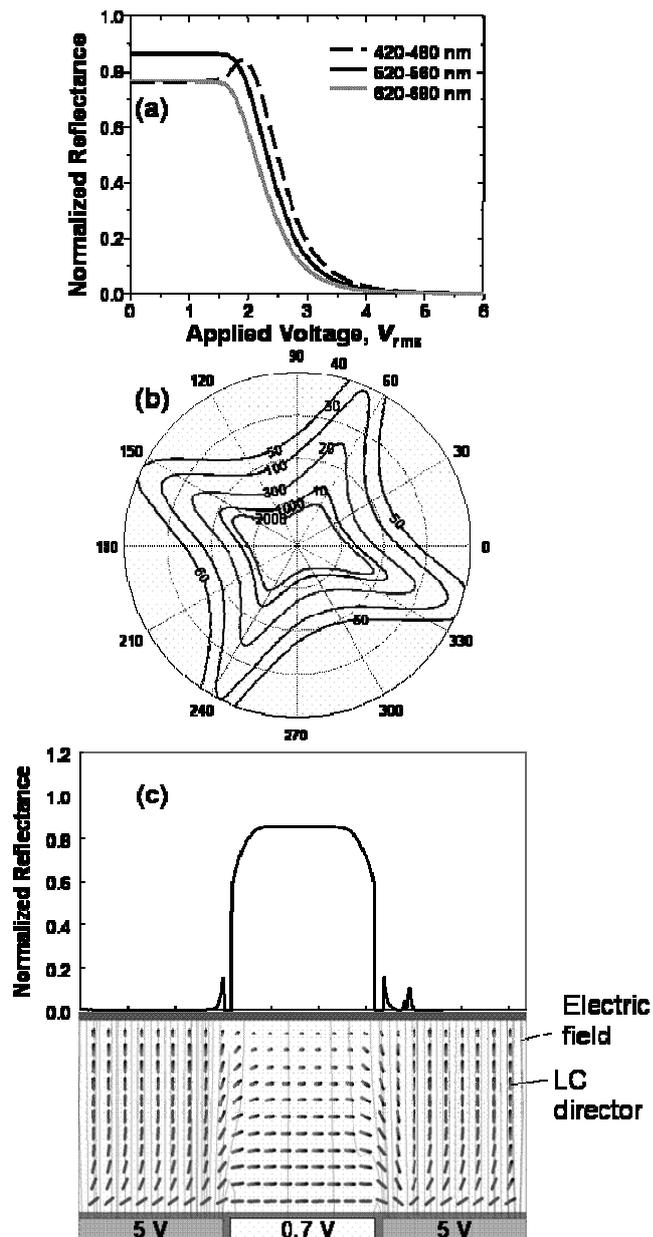


Fig. 3.2 Simulated results of (a) the broad band RV curve, (b) the broad band green light iso-contrast viewing diagram, and (c) the LC director and the reflectance profiles of NW  $90^\circ$ -MTN mode with  $\beta=20^\circ$  and  $d\Delta n=240$  nm.

Figure 3.2 (c) shows the 2D simulation results of the LC director profile and the reflectance calculated by Jones matrix method for the dark-bright-dark pixel configuration with 2.8  $\mu\text{m}$  cell gap and  $2^\circ$  pretilt angle at green band (540 nm). In this condition, the fringing fields are the strongest. As shown in the 2D LC director profile, the fringing fields at the pixel edges will penetrate into the adjacent pixels and induce light leakage in the dark pixels. This effect will degrade the contrast ratio as well as the image sharpness.

The advantages of this mode are the high contrast ratio owing to the natural surface phase compensation of the two orthogonal boundary layers and the relatively small fringing-field effect. The calculated 2D flat field contrast ratio exceeds 6000:1 for the normally incident light. The shortcoming of this  $90^\circ$  MTN mode is that its maximum optical filled factor is  $\sim 84.7\%$  at the dark-bright-dark configuration. Here we define the optical filled factor as

$$F = \frac{1}{S} \int R_{\text{bright}} \quad (3.1)$$

where  $S$  denotes the dimension of the turned-on pixels and  $R_{\text{bright}}$  is the normalized reflectance within the bright pixel area. Changing the twist angle to  $80^\circ$  would boost the filled factor to  $\sim 95\%$ . However, the contrast ratio decreases drastically because of incomplete surface phase compensation.

### NW Film-Compensated 63.6°-MTN Mode

The normalized reflectance  $R_{\perp}$  of a reflective twisted LC cell under crossed-polarizer condition can be given as\*:

$$R_{\perp} = \left| \begin{pmatrix} -\sin \beta & \cos \beta \end{pmatrix} \begin{pmatrix} \cos X - i \frac{\Gamma \sin X}{2} & -\phi_t \frac{\sin X}{X} \\ \phi_t \frac{\sin X}{X} & \cos X + i \frac{\Gamma \sin X}{2} \end{pmatrix} \begin{pmatrix} \cos X - i \frac{\Gamma \sin X}{2} & \phi_t \frac{\sin X}{X} \\ -\phi_t \frac{\sin X}{X} & \cos X + i \frac{\Gamma \sin X}{2} \end{pmatrix} \begin{pmatrix} \cos \beta \\ \sin \beta \end{pmatrix} \right|^2 \quad (3.2)$$

By further expanding Eq. (3.2),  $R_{\perp}$  can be given as:

$$R_{\perp} = \left( \Gamma \frac{\sin X}{X} \right)^2 \left( \sin 2\beta \cos X - \frac{\phi_t}{X} \cos 2\beta \sin X \right)^2 \quad (3.3)$$

When setting  $\beta=0^\circ$ , Eq. (3.3) becomes:

$$R_{\perp} = \left[ \frac{2\phi_t(\Gamma/2)}{\phi_t^2 + (\Gamma/2)^2} \right]^2 \sin^4 X. \quad (3.4)$$

From this equation,  $R_{\perp}=100\%$  can be obtained when setting  $\phi_t=\sqrt{2}\pi/4$  ( $63.6^\circ$ ) and  $d\Delta n/\lambda=\sqrt{2}/4$ . This mode has the advantage of high reflectance; however, a very high voltage is needed to obtain a good dark state due to the absence of intrinsic phase compensation. In order to operate at lower voltage, a uniaxial film is employed. Figure 3.3 (a) shows the 1D simulated results of the voltage-dependent reflectance curve under broadband incident light when a uniaxial film with  $\alpha=110^\circ$  (referring to Fig. 2.6) and  $(d\Delta n)_{\text{film}}=24$  nm is applied. The required phase retardation  $d\Delta n$  of the LC cell is 203 nm and entrance polarizer angle is set at  $\beta=0^\circ$ . As shown in Fig. 3.3 (a), the maximum reflectance slightly decreases to 97% due to the effect of the compensation film. Figure 3.3 (b) plots the calculated results of iso-contrast viewing diagram under broadband green light with  $V_{\text{on}}=5$  V and  $V_{\text{off}}=0.7$  V. The contour line for 1000:1 contrast ratio reaches  $10^\circ$  viewing cone. Figure 3.3 (c) demonstrates the 2D simulated results of the LC director profile and the reflectance for the dark-bright-dark pixel configuration with  $2.4 \mu\text{m}$  cell gap. The light leakages still exists at the dark pixels due to the influence of fringing fields.

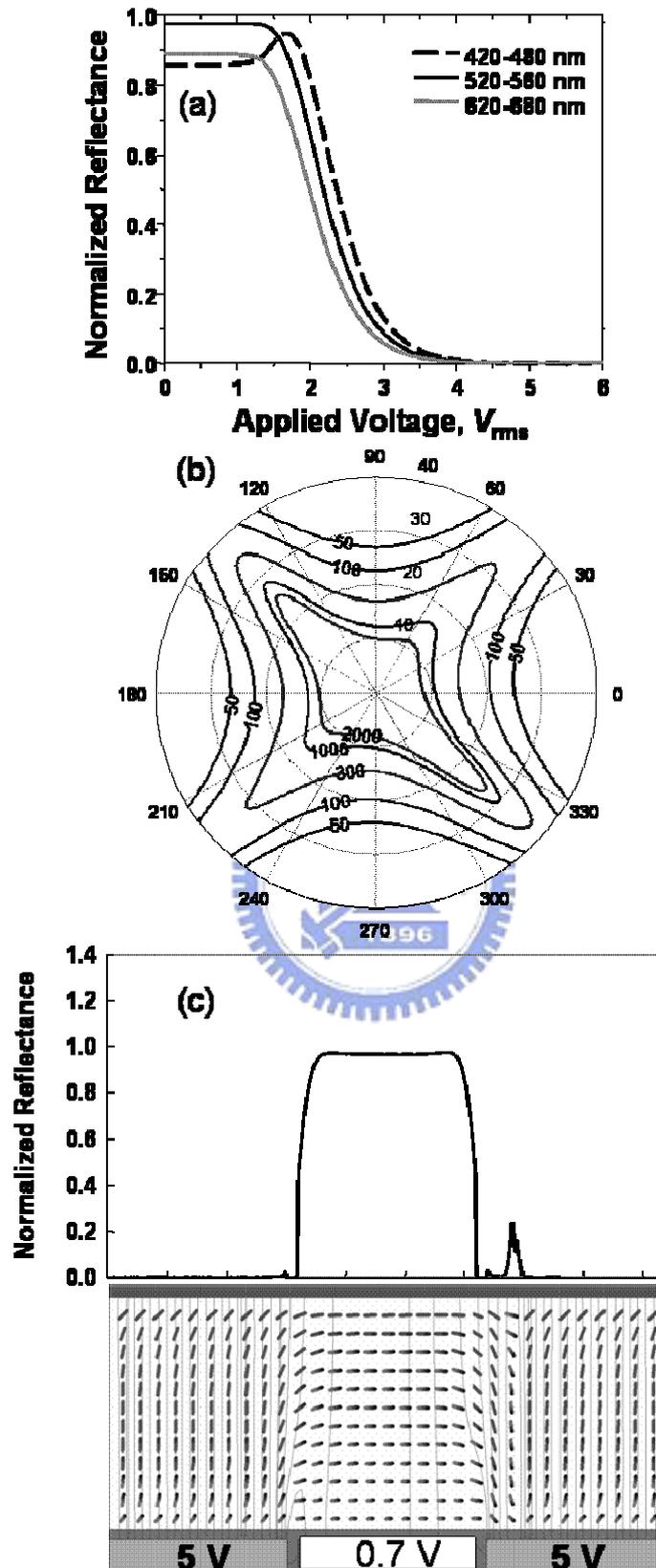


Fig. 3.3 Simulated results of (a) the broad band RV curve, (b) the broad band green light iso-contrast viewing diagram, and (c) the LC director and the reflectance profiles of 63.6°-MTN mode with  $\beta=0^\circ$ ,  $d\Delta n=203$  nm,  $(d\Delta n)_{film}=24$  nm, and  $110^\circ$  film angle related to x-axis.

In addition, the optical filled factor is only about 92.7% since the maximum  $R_{\perp}$  can not reach 100%. When setting  $\beta=4^{\circ}$ ,  $d\Delta n=212$  nm,  $(d\Delta n)_{\text{film}}=15$  nm, and  $\alpha=136^{\circ}$ , the maximum  $R_{\perp}$  can be boosted up to 99%. In this circumstance, more birefringence effect is introduced to enhance the reflectance. However, a stronger fringing field occurs and results in a lower  $F$ . Thus, this tradeoff is not worth taking.

### ***NW Film-Compensated 45°-MTN Mode***

The film-compensated 45° MTN cell has twist angle  $\phi_t=45^{\circ}$  and  $\beta=78^{\circ}$ . The required phase retardation  $d\Delta n$  is only 195 nm for normally white operation. To obtain a good dark state at lower voltage, a uniaxial film with  $\alpha=110^{\circ}$  and  $(d\Delta n)_{\text{film}}=27$  nm is added. Figure 3.4 (a) shows the 1D simulated results of the voltage-dependent reflectance curve under broadband R, G and B lights. The maximum reflectance of this mode can reach 100% and on-state voltage is 5V. Figure 3.4 (b) shows the calculated results of iso-contrast viewing diagram under broadband green light with  $V_{\text{on}}=5.0$  V and  $V_{\text{off}}=0.7$  V. We can see that the contour line for 1000:1 contrast ratio exceeds  $10^{\circ}$  polar angle in all directions. This large viewing cone results from the small  $d\Delta n$  value. Figure 3.4 (c) demonstrates the 2D simulation results of the LC director profile and the reflectance for the dark-bright-dark pixel configuration with 2.3  $\mu\text{m}$  cell gap. It is shown that its response to fringing fields is similar to other two MTN modes as we have discussed. Among them, 90°-MTN cell has the smallest and 63.6°-MTN has the largest light leakages in the dark-pixel areas.

The advantages of the film-compensated 45°-MTN mode are twofold: high optical filled factor (up to 96.7%) and low  $d\Delta n$  value which, in turn, leads to a thin cell gap and fast response time. Therefore, this mode is particularly attractive for color sequential displays using a single LC panel. However, the dark state of this mode is not as good as that of 90°-MTN mode since the complete compensation only occurs at certain wavelengths. Besides, the required compensation film has a relatively small  $d\Delta n$  value which is not easy to fabricate. The film needs to be laminated onto the surface of the polarizing beam splitter.

Any artifacts or bubbles during the lamination process would be magnified and projected to the screen. Moreover, the film has to withstand high power illumination from the arc lamp.

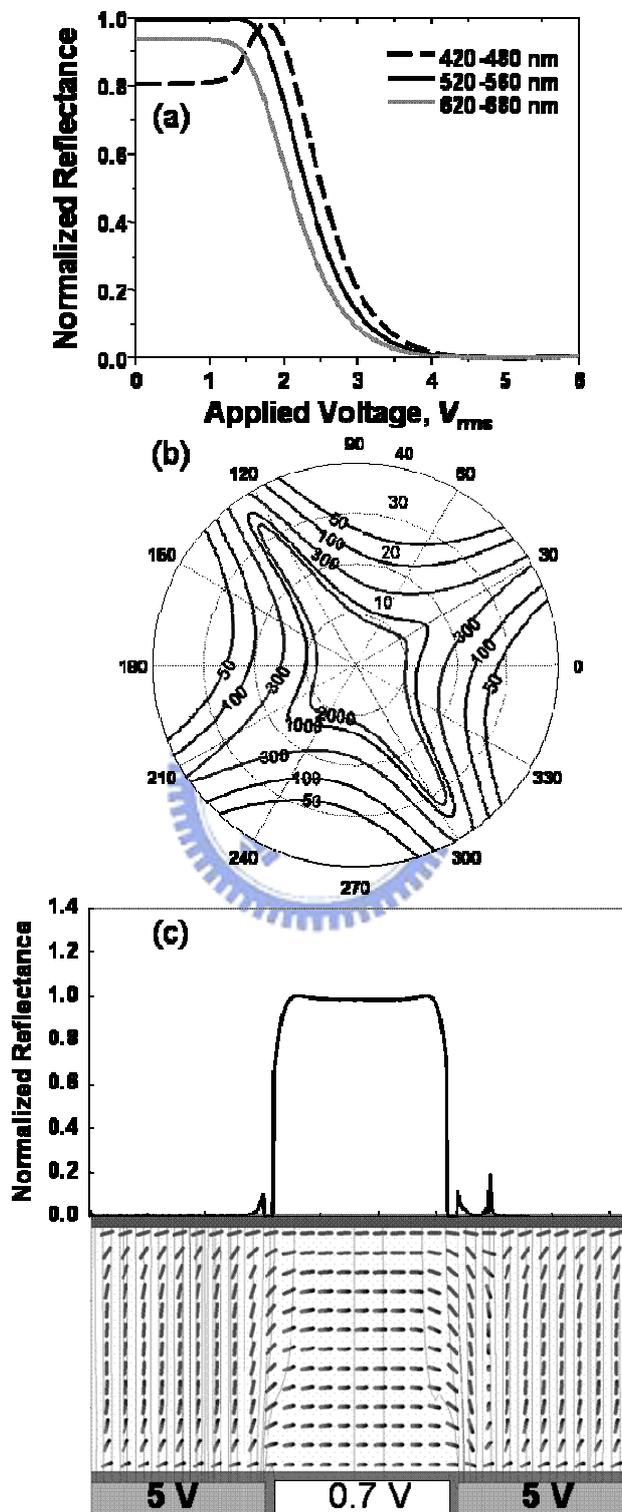


Fig. 3.4 Simulated results of (a) the broad band RV curve, (b) the broad band green light iso-contrast viewing diagram, and (c) the LC director and the reflectance profiles of 45°-MTN mode with  $\beta=78^\circ$ ,  $d\Delta n=195$  nm,  $(d\Delta n)_{film}=27$  nm, and  $110^\circ$  film angle related to x-axis.

### 3.2.1.2 Twisted nematic modes (TN)

#### *NB 63.6°-TN Mode*

As in 63.6°-MTN mode, this mode also has twist angle  $\phi_t=63.6^\circ$  and beta angle  $\beta=0^\circ$ , but without any compensation film. When  $d\Delta n=512$  nm, it can be operated in normally black mode, however, its bright state is greatly affected by the  $d/P_0$  ratio. Figure 3.5 (a) shows the 1D simulated results of the voltage-dependent reflectance curve with  $d/P_0=0.6$ . Unlike the MTN devices, NB TN mode has the advantage of relatively low on-state voltage because the LC molecules only need to tilt up slightly to reach the maximum reflectance. As shown in Fig. 3.5 (a),  $R_{\perp}=1$  is reached when the applied voltage is merely 3.3 V. Another advantage of the NB 63.6°-TN mode is that it does not require a compensation film. Hence, the cost is reduced. Figure 3.5 (b) shows the calculated results of the iso-contrast viewing diagram under broadband green light with  $V_{on}=3.3$  V and  $V_{off}=0.7$  V. The 1000:1 contrast ratio contour line exceeds  $12^\circ$  viewing cone.

When considering the 2D LC director profile, the chiral dopant plays an important role in the fringing-field effect. Figure 3.5 (c) demonstrates the 2D simulated results with  $d/P_0=0.6$  and  $d=4.8$   $\mu\text{m}$ . We find that the chiral dopant reorients the LC molecules and induces severe LC distortions. These distortions extend from the bright-pixel to the dark-pixel areas, which optically generate many unwanted light fringes. Hence, the contrast ratio is very poor in this condition. In order to obtain high reflectance and high contrast ratio simultaneously, we can reduce the cell gap to minimize the fringing-field effect. Adjusting the  $d/P_0$  ratio can also achieve a better performance in this mode. Figure 3.6 shows the dependency of contrast ratio on  $d/P_0$  ratio in the 63.6°-TN mode with  $d=2.1$   $\mu\text{m}$ . As shown in this figure, the largest contrast ratio ( $\sim 110:1$ ) occurs at around  $d/P_0=0.45$ . Besides, a too large or too small  $d/P_0$  ratio will deteriorate the contrast ratio.

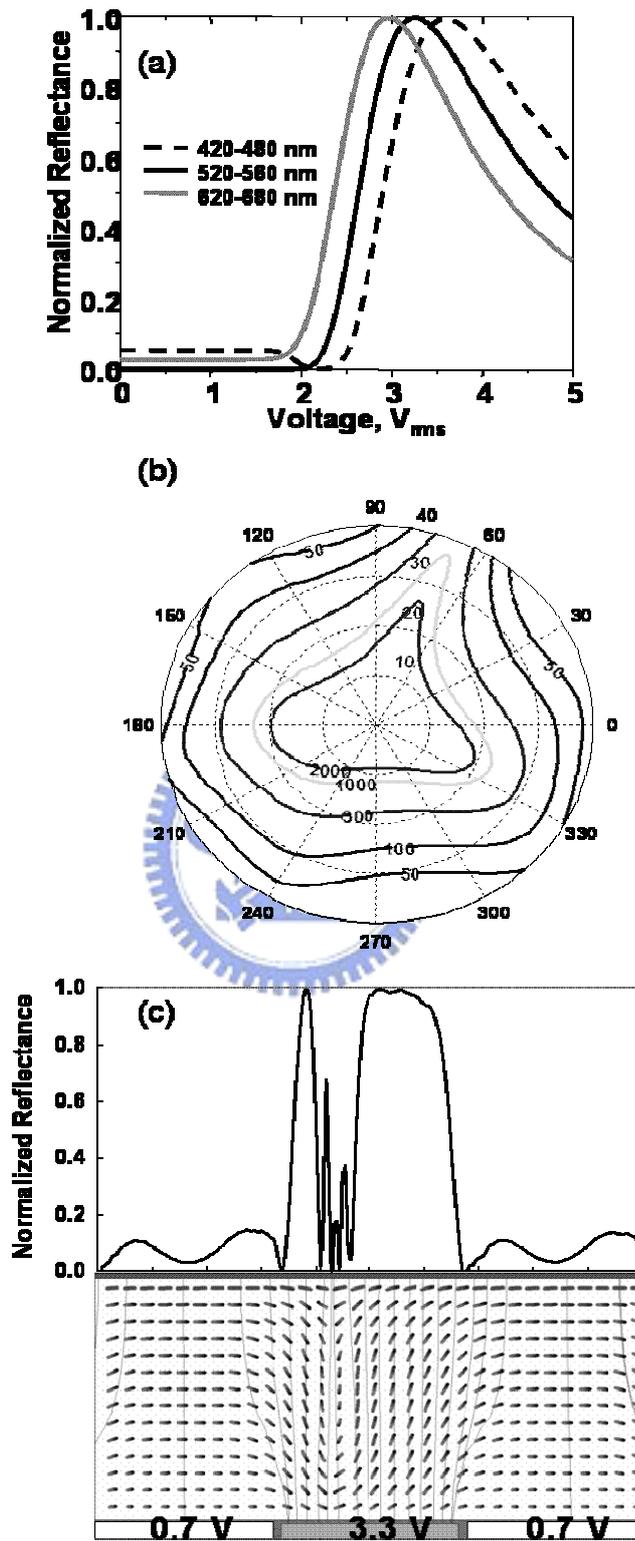


Fig. 3.5 Simulated results of (a) the broad band RV curve, (b) the broad band green light iso-contrast viewing diagram, and (c) the LC director and the reflectance profiles of NB 63.6°-TN mode with  $\beta=0^\circ$ ,  $d\Delta n=508$  nm, and  $d/p=0.6$ .

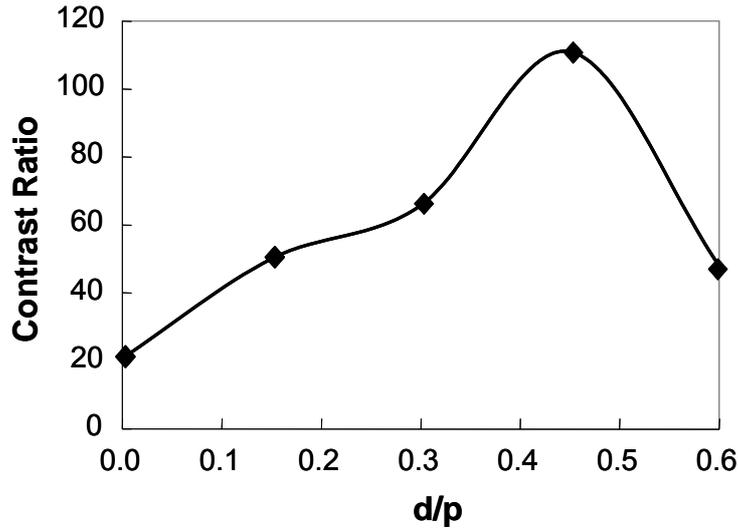


Fig. 3.6 Calculated results of the contrast ratio with respect to  $d/p$  ratio for  $63.6^\circ$ -TN mode with  $d=2.1 \mu\text{m}$ .

### ***NB 45°-TN Mode***

This mode was first reported by Grinberg et al [10]. The cell parameters are as follows: twist angle  $\phi_t=45^\circ$ ,  $\beta=0^\circ$ ,  $d\Delta n=533 \text{ nm}$ , and  $d/P_0=0$ . Figure 3.7 (a) depicts the 1D simulated voltage-dependent reflectance curves. The turned-on voltage is only 2.8 V due to the high  $d\Delta n$  value. However, the maximum normalized reflectance  $R_\perp$  is only 96%. Adding chiral dopant in LC may increase the reflectance; however, the director distortions generated by fringing fields become more severe and the response time is increased. Moreover, a negative chiral dopant (i.e., opposite to the LC twist sense) will cause instability to the LC twist structure. Figure 3.7 (b) shows the calculated results of iso-contrast viewing diagram. Within the  $10^\circ$  viewing cone, the contrast ratio exceeds 1000:1. The 2D simulation results with  $d=5 \mu\text{m}$  are demonstrated in Fig. 3.7 (c). The calculated optical filled factor is 70.6%. We find that the light leakages caused by fringing fields are much more severe than those in the MTN cells due to the relatively thick cell gap. It is found that the whole bright area is shifted into the right-hand dark pixel. This effect will cause image blurs and deteriorate the contrast ratio. We can also reduce the cell gap to minimize the fringing-field effect. By using  $2.2 \mu\text{m}$  cell gap, the bright area is shifted back to the normal position and the optical filled factor is about 85.6%; however, a high

birefringence ( $\Delta n=0.24$ ) material is necessary to meet such a cell gap requirement. The simulation results are shown in Fig. 3.8.

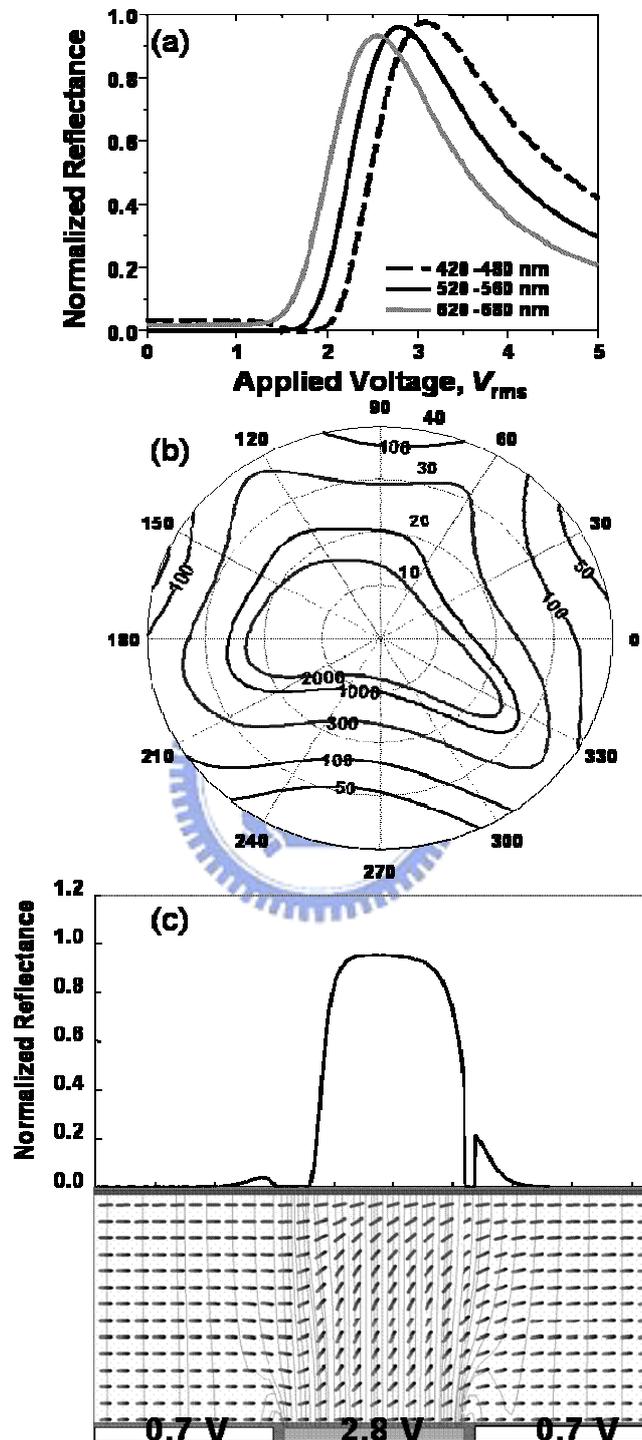


Fig. 3.7 Simulated results of (a) the broad band RV curve, (b) the broad band green light iso-contrast viewing diagram, and (c) the LC director and the reflectance profiles of NB 45°-TN mode with  $\beta=0^\circ$ ,  $d\Delta n=533$  nm.

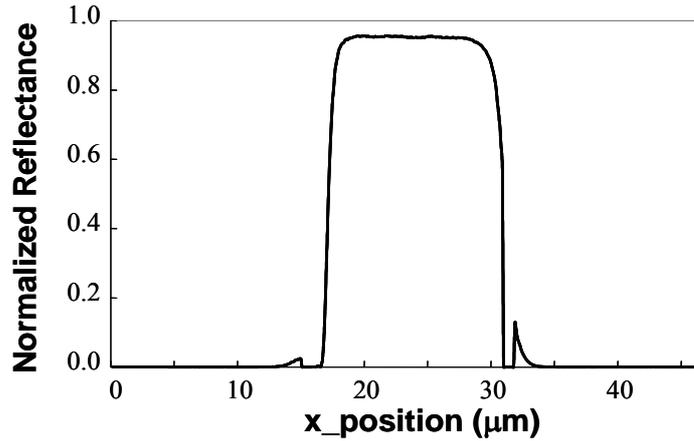


Fig. 3.8 Simulated reflectance of NB 45°-TN mode with  $d=2.2 \mu\text{m}$ .

### ***NB 52°-TN Mode***

This mode has  $\phi_i=52^\circ$ ,  $\beta=0^\circ$  and  $d/P_0=0$ . The main advantage of this mode is that its maximum normalized reflectance can reach 100% without using any chiral dopant [11]. For  $\phi_i \neq 52^\circ$ , chiral material must be employed to boost the reflectance to 100%. However, as we have already mentioned, chiral dopant is unfavorable in many aspects. Figure 3.9 (a) plots the 1D simulated voltage-dependent reflectance curves with  $d\Delta n=517 \text{ nm}$ . Figure 3.9 (b) shows the calculated results of iso-contrast viewing diagram with  $V_{\text{on}}=2.8 \text{ V}$  and  $V_{\text{off}}=0.7 \text{ V}$  under a broadband green light. Similarly, the contour line for 1000:1 contrast ratio goes beyond  $10^\circ$ . Basically, the performance of NB 52°-TN mode is very similar to that of NB 45°-TN mode except for a higher reflectance. Both modes have low operating voltage, but suffer from severe fringing-field effect. Figure 3.9 (c) demonstrates the 2D simulated results with  $d=4.8 \mu\text{m}$ . The calculated optical filled factor is 79.6%. Similarly, an optical bounce at the left-hand dark pixel and the shifted bright area into the right-hand dark pixel is revealed due to the fringing-field effect. The effect is even stronger than that in the 45°-TN. By reducing the cell gap to  $d=2.2 \mu\text{m}$  (by using  $\Delta n=0.24$ ), the fringing fields are suppressed significantly and the calculated optical filled factor is raised to 91.5%. The results are shown in Fig. 3.10.

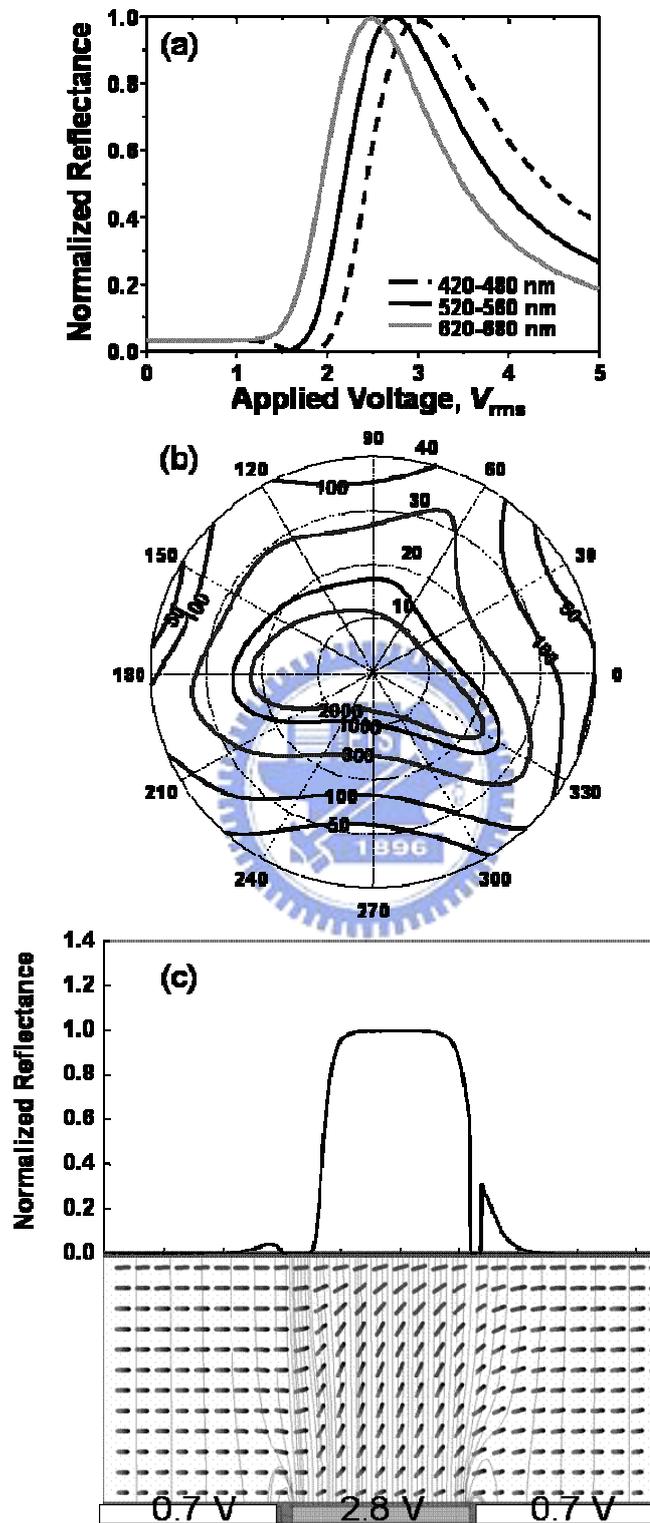


Fig. 3.9 Simulation results of (a) the broad band RV curve, (b) the broad band green light iso-contrast viewing diagram, and (c) the LC director and the reflectance profile of NB 52°-TN mode with  $\beta=0^\circ$ ,  $d\Delta n=517$  nm.

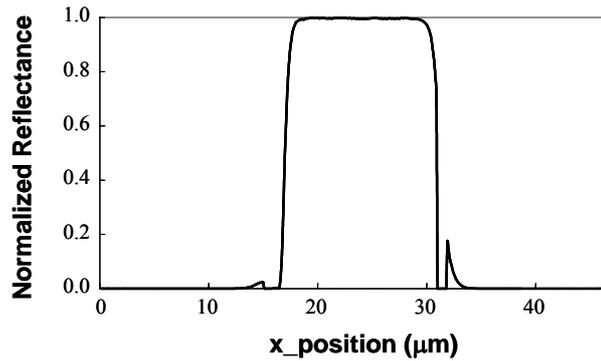


Fig. 3.10 Simulated reflectance of NB 52°-TN mode with  $d=2.2 \mu\text{m}$ .

## 3.2.2 Non-twisted LC modes

### 3.2.2.1 Vertically aligned mode (VA)

For VA mode, the LC molecules are aligned nearly perpendicular to the substrate surfaces, except for a small ( $\sim 2^\circ$ ) pretilt angle. The LC material employed should have a negative dielectric anisotropy. Since the residual phase of the dark state is very small, VA mode exhibits a very good contrast ratio between two crossed polarizers. Moreover, the contrast ratio is relatively insensitive to the incident wavelength, cell gap, and operation temperature fluctuation. Hence, VA mode holds promise for LCOS application. Figure 3.11 (a) shows the 1D simulated voltage-dependent reflectance curves of a VA cell with  $d\Delta n=192 \text{ nm}$ . The contrast ratio of the reflective VA cell exceeds 2000:1 at any off-normal angle along the vertical and horizontal directions. However, the contrast ratio is poor at the  $45^\circ$  and  $135^\circ$  azimuthal angles. To improve the viewing angle performance, a negative c-plate is needed.<sup>19</sup> Figure 3.11 (b) shows the calculated results when a negative c-plate with  $(d\Delta n)_{\text{film}}=-183 \text{ nm}$  is employed. We see the contour lines corresponding to 2000:1 and 1000:1 contrast ratio reach  $17^\circ$  and  $22^\circ$  polar angle, respectively.

Although VA mode has several advantages, it has a serious problem on the strong fringing-field effect. Figure 3.11 (c) demonstrates the 2D simulated results with  $2.3 \mu\text{m}$  cell gap. As shown in the figure, the dark pixels have an excellent black state. However, the fringing field induces a relatively wide dark line near the right edge of the bright pixels.

This dark line splits the bright pixel into two unequal parts and drastically reduces the optical filled factor. The integrated optical filled factor is only 70.2%. In addition, the LC distortions caused by fringing fields even encumber the dynamic switching of the image and produce a very slow transition in the dynamic process, as will be addressed later.

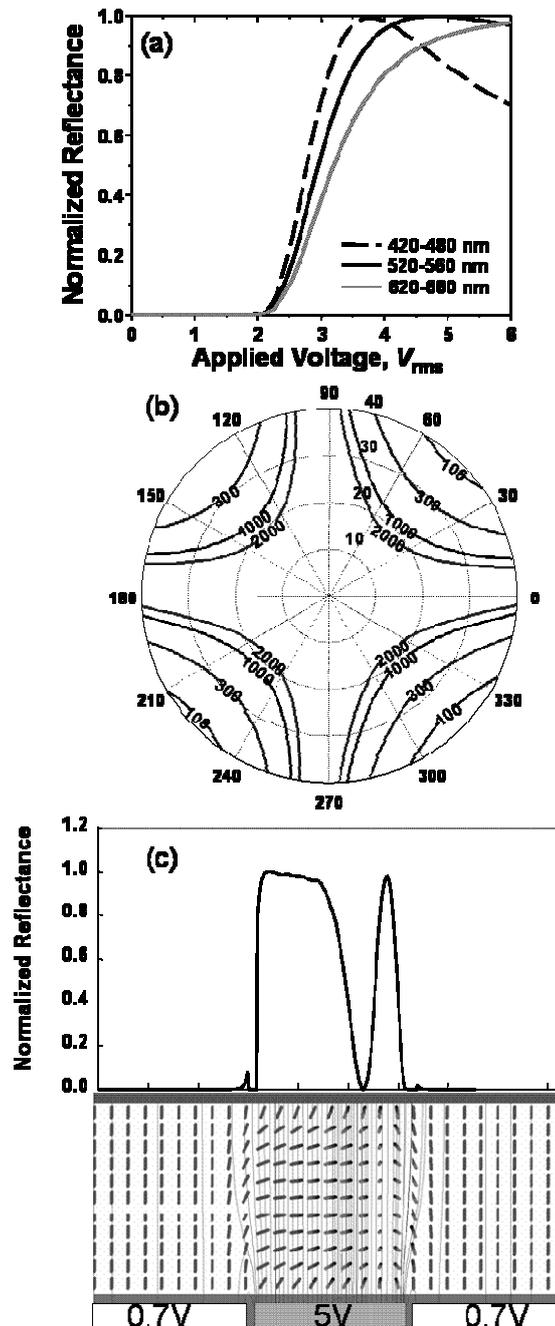


Fig. 3.11 Simulation results of (a) the broad band RV curve, (b) the broad band green light iso-contrast viewing diagram, and (c) the LC director and the reflectance profile of VA mode with  $\beta=45^\circ$ ,  $d\Delta n=192$  nm and  $(d\Delta n)_{c-film}=183$  nm.

### 3.2.2.2 Film-compensated homogenous mode (FCH)

A homogeneous cell is known for its fast response time. However, its dark state voltage is too high unless a phase retardation film is used [11]. The principal axis of the film is oriented to be orthogonal to the LC axis such that their phase retardations are subtractive:

$$\delta = \frac{4\pi(d_1\Delta n_1 - d_2\Delta n_2)}{\lambda} \quad (3.5)$$

Where  $d_{1,2}$  and  $\Delta n_{1,2}$  represent the cell gap and birefringence of the LC cell and compensation film, respectively. Fig. 3.12 (a) shows the simulated green band reflectance profile for homogeneous cell without any compensation film. The phase retardation of LC cell  $d_1\Delta n_1$  is 184 nm and  $\beta$  angle is  $45^\circ$ . The on pixel is set at 4 volts and the adjacent off pixels are set at 1.5 volts. In this condition, the dark state is poor due to the residual phase from the boundary layers. After carefully choosing a compensation film with suitable phase retardation, the residual phase can be eliminated. Fig. 3.12 (b) gives the simulated reflectance profile of a FCH with  $d_2\Delta n_2=52$  nm. As shown in the figure, the dark state in this condition is much better. However, the light leakages due to the fringing-field effect still appear at the dark pixels which are obstacles for realizing high image quality.

The main advantage of FCH mode is the low  $d\Delta n$  value. It guarantees a thin cell gap which efficiently boost the optical response time of the LC cell. A drawback of this mode is the narrow range of dark-state voltage, which means that any thermal fluctuation may cause light leakage in the dark state. Using smaller  $d_2\Delta n_2$  can widen the range of dark-state voltage. However, a higher voltage must be applied to ensure a good dark state.

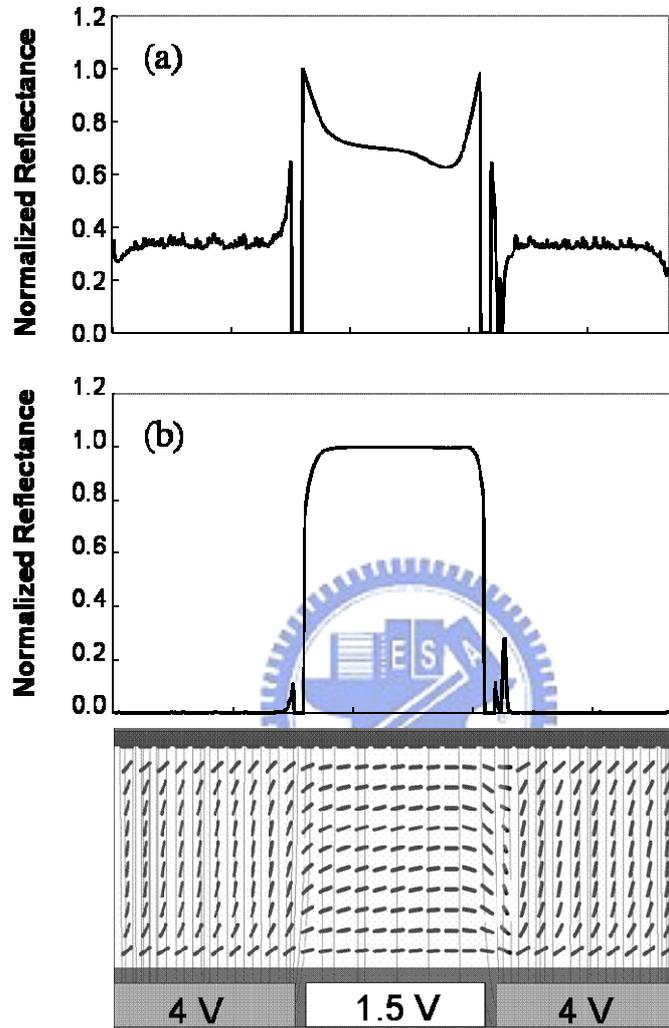


Fig. 3.12 The simulated green band reflectance profile of FCH mode,  $d_1\Delta n_1 = 184$ ,  $\beta = 45^\circ$  (a) without compensation film, and (b) with compensation film,  $d_2\Delta n_2 = 52$  nm.

### 3.3 Influences of the cell structures

#### 3.3.1 The effect of pixel pitch

Obviously, the fringing-field effect is strongly influenced by pixel pitch [13]. When pixel pitch decreases, fringing fields become stronger. When the pixel pitch is larger, the region influenced by fringing fields occupies smaller fraction of the adjacent pixels area as shown in Fig. 3.13. Figure 3.14 shows the simulated pixel pitch dependent contrast ratio for each mode with dark-bright-dark pixel configuration. As the pixel size decreases, the contrast ratio decreases. Based on the figure, the MTN modes can reach higher contrast ratio than the TN modes by taking the advantage of smaller fringing-field effect in every pixel pitch. Among all the modes, the  $63.6^\circ$ -TN mode has the lowest contrast ratio. This mode suffers strong fringing-field effect due to the influences of chiral dopants and, as a result, the contrast ratio is limited to  $\sim 15:1$ . It is also noteworthy from the figure that the contrast ratio of the  $90^\circ$ -MTN cell is higher than that of the VA mode after the pixel pitch becomes smaller than  $14\ \mu\text{m}$ . Because the  $90^\circ$ -MTN is relatively not sensitive to the fringing-field effect, the contrast ratios maintain at around 220 after the pixel pitch reduced to  $12\sim 14\ \mu\text{m}$ . Hence, the  $90^\circ$ -MTN should be considered a promising candidate when designing a high resolution display.

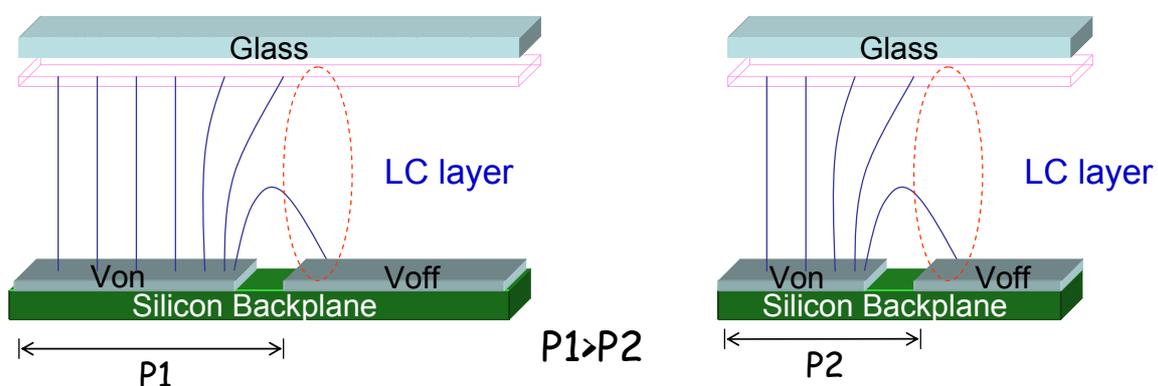


Fig. 3.13 Sketch of the influence of the pixel pitch to the fringing-field effect.

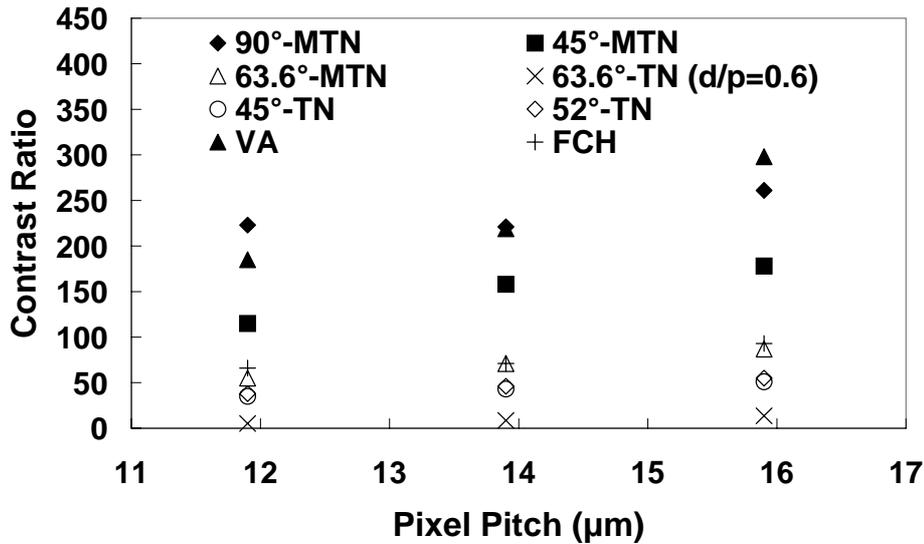


Fig. 3.14 Calculated contrast ratio of each LC operation mode at dark-bright-dark state with respect to the pixel size.

### 3.3.2 The effect of cell thickness

Cell gap is another important factor affecting the fringing-field effect. The fringing field is restrained when the cell gap is small. Figure 3.15 demonstrates the concept of reducing fringing field by shrinking cell gap. As shown in the figure, the electric fields only slightly extend to the adjacent pixel when the cell gap is small. As the cell gap increases, the fringing fields stretch out more. The cell gap effect is especially important when the TN cells are employed. In a TN cell, the LC  $d\Delta n$  value must be large enough to satisfy the polarization rotation effect. Therefore, a thicker cell gap is usually used in TN cells.

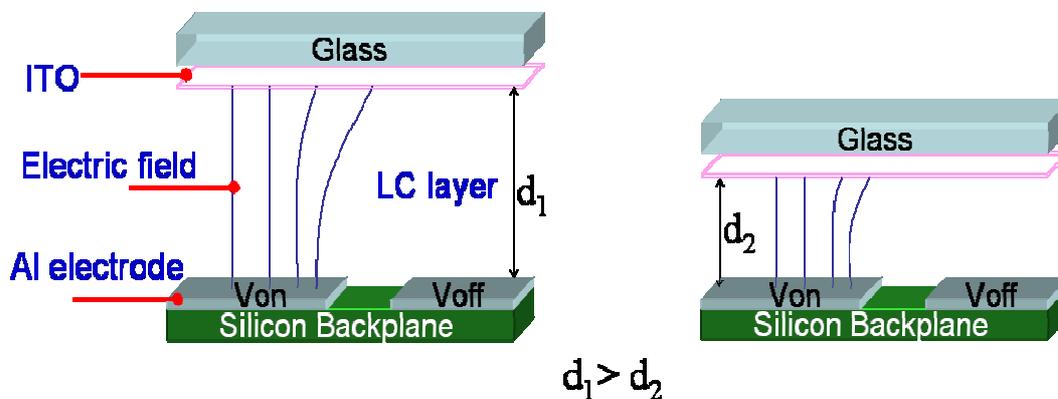


Fig. 3.15 Sketch of the effect of cell gap.

Figure 3.16 summarizes the contrast ratios for the aforementioned NB TN modes under different cell gaps. As shown in the figure, a very poor contrast ( $\sim 50:1$ ) is obtained when the cell gap is around  $5 \mu\text{m}$ . With the cell gap is reduced to  $\sim 2 \mu\text{m}$ , the contrast ratio exceeds  $500:1$  for both  $45^\circ\text{-TN}$  and  $52^\circ\text{-TN}$  modes. Although the contrast ratio of  $63.6^\circ\text{-TN}$  mode also rises as the cell gap shrinks, the chiral dopant still causes disorder in the cell and limits the contrast ratio. For such a small cell gap ( $\sim 2 \mu\text{m}$ ), high birefringence LC materials with  $\Delta n \sim 0.24$  must be used to satisfy the  $d\Delta n$  requirements. For the VA and MTN modes, the phase retardation of the LC cell do not need to be as high as those of TN modes since the birefringence effect is involved. Therefore, a thinner cell gap can be achieved without using a high birefringence LC material. High optical efficiency and contrast ratio can be obtained when using a thinner cell gap. However, the influence of the cell gap for VA mode is not so obvious. The distortions of LC directors in the bright pixel are triggered by small fringing fields and extend to the adjacent regime in a long dynamic process. The optical filled factor is only slightly improved from  $70.2\%$  to  $71.8\%$  even the cell gap is reduced to  $1 \mu\text{m}$ . A newly developed method for eliminating the fringing-field effect of VA cell will be addressed in Chap. 4.

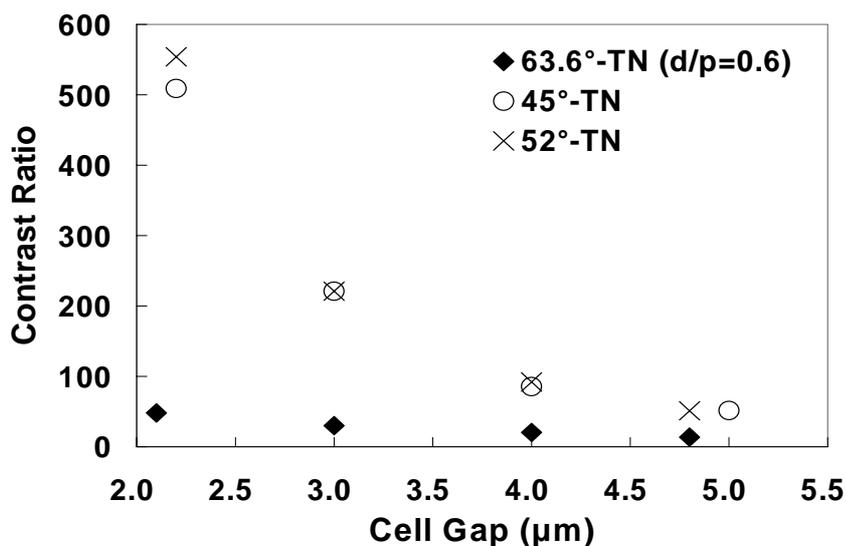


Fig. 3.16 Calculated contrast ratio of  $63.6^\circ\text{-TN}$ ,  $45^\circ\text{-TN}$  and  $52^\circ\text{-TN}$  at dark-bright-dark state with respect to cell gap.

### 3.3.3 The effect of pretilt angle

Pretilt angle is also found to be influential to the fringing-field effect, especially in VA mode LCOS devices [14]. Fig. 3.17 sketches the effect of pretilt angle to a negative liquid crystal. As shown in the figure, the LC molecules with high pretilt angle can be reverse-tilted easily even when the fringing field is only slightly bended. Under the same condition, the LC molecules with lower pretilt angle are maintained normal-tilted, which means the LC distortions area will be smaller. Fig 3.18 (a) shows the simulated reflectance profiles of VA cells at dark-bright-dark state with their pretilt angles varies from  $85^\circ$  to  $88^\circ$ . The pixel pitch is  $15\ \mu\text{m}$  and the interpixel is  $0.9\ \mu\text{m}$ . As shown in the figure, the dark stripe in the bright pixel moves more toward the inter-pixel gap area when lower pretilt angle is adopted. The calculated optical filled factor is presented in Fig. 3.18 (b). It is shown that the optical filled factor can be slightly raised as a lower pretilt angle is employed. In addition, the dynamic response of the LCOS panel when switched from the dark-bright-dark state to the all-bright state is faster for those with lower pretilt angle as shown in Fig. 3.19. However, since the LC distortions still exist, the improvement is very limited. Furthermore, since lowering pretilt angle will reduce the contrast ratio significantly, the tradeoff may not be worth-taken.

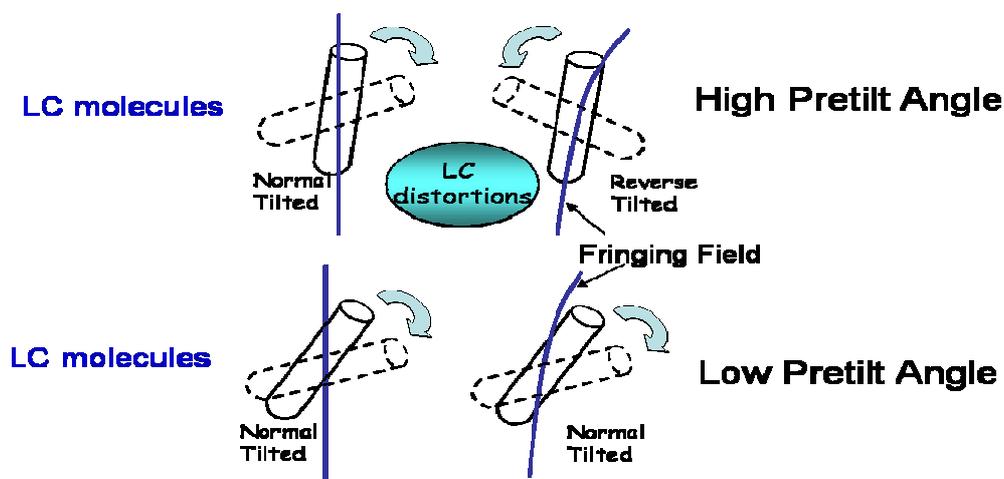


Fig. 3.17 Sketch of the effect of pretilt angle to negative liquid crystal molecules.

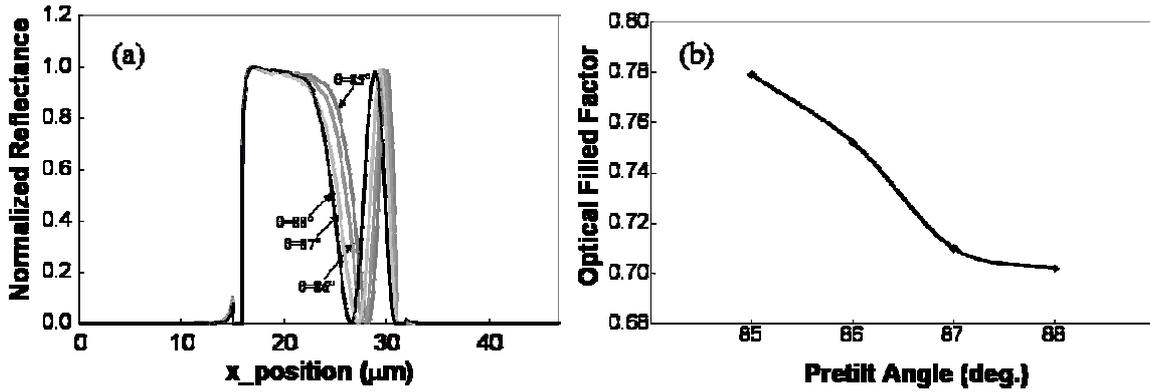


Fig. 3.18 (a) Simulated reflectance profiles of VA mode at dark-bright-dark state with pretilt angle varies from 85° to 88°, and (b) the calculated optical filled factor with respect to the pretilt angle.

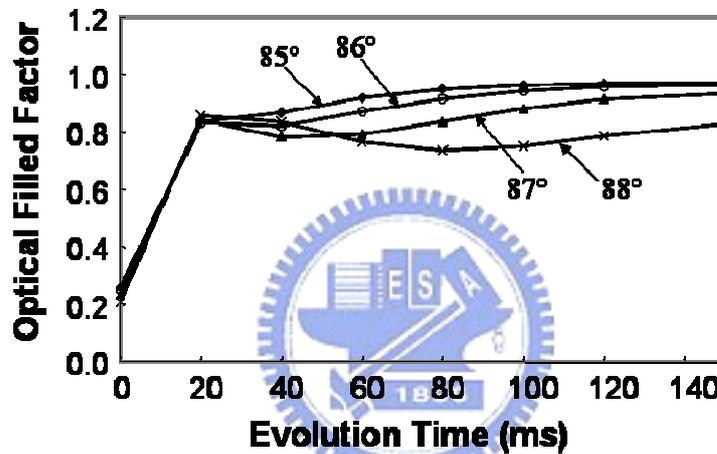


Fig. 3.19 Calculated optical filled factor with respect to evolution time of VA cell after switched from dark-bright-dark state to the all-bright state with pretilt angle varies from 85° to 88°.

### 3.3.4 Electrode slope effect

During the manufacturing process, the electrode edges may not be as steep as we presume. There should be a finite electrode slope which may influence the distributions of fringing fields near the pixel edges [15,16]. The slope of electrode is sketched in Fig. 3.20(a) and defined as  $s=h/b$ , where  $h$  is the thickness of the aluminum electrode, and  $b$  is the length difference between the electrode top and the bottom. Here we analyze the effect of electrode slope for the three most attracting LC operation mode that we have mentioned: 90°-MTN, film-compensated 45°-MTN and VA modes. Figure 3.20(b) presents the calculated contrast ratio with respect to the electrode slope ranging from 0.3 to  $\infty$  when the

panel is operated at the dark-bright-dark state. Based on the calculated results, VA mode has its contrast ratio decreased monotonically as the electrode slope decreases. Therefore, the electrode slope should be as close to infinity as possible. For 90°-MTN mode, we can find a minimum contrast ratio when the slope is around 1. Either a higher or lower slope can give a higher contrast ratio. For film-compensated 45°-MTN, the calculated contrast ratio is not that sensitive to the electrode slope. Nevertheless, we can still obtain the highest contrast ratio when the sharp electrode ( $s=\infty$ ) is employed. The detailed mechanism of this phenomenon is beyond the scope of this thesis and will not be discussed.

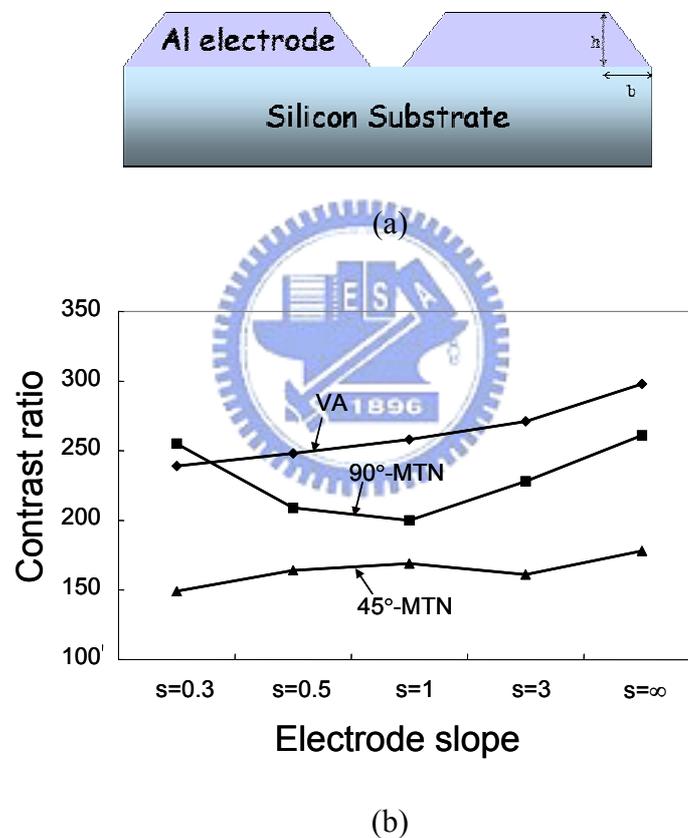


Fig. 3.20 (a) Sketch of the electrode slope; (b) Calculated contrast ratio with respect to the electrode slope ranging from 0.3 to  $\infty$  at dark-bright-dark state for 90°-MTN, 45°-MTN and VA mode.

### 3.4 Dynamic response of the panel switched from the dark-bright-dark state to the all-bright state

The response time of LCOS devices are usually faster than those of the direct view displays due to its relative thinner cell gap. For MTN and FCH cells, the response time is

relative fast due to its thin cell gap. For TN modes, the requirement of larger cell gaps results in much longer response time. In addition, an even longer time is needed to reach the stable state if chiral dopants are added in the LC mixture. The use of a thinner cell gap with a high birefringence material would help to reduce the response time for the TN modes. It is noteworthy that the dynamic behaviors of LCOS devices are influenced by the LC distortions generated by fringing fields. This phenomenon is especially obvious in VA mode when the panel is switched from the dark-bright-dark to the all-bright patterns. Although the cell gap of a VA cell is only around  $2\ \mu\text{m}$ , it still takes a long time to reach the stable state [17,18]. Figure 3.21 shows the calculated transient states for such a VA cell with  $d=2.3\ \mu\text{m}$  and  $\theta=88^\circ$ . The fringing-field-caused LC distortions take an extreme long time to be relaxed back to the normal condition. This relaxation time is influenced by the LC viscosity and the boundary conditions. As shown in the figure, the light efficiency is only 65.6% after 90 ms. Under such conditions, image blurring will occur for a moving object and, thus, the image quality is drastically deteriorated.

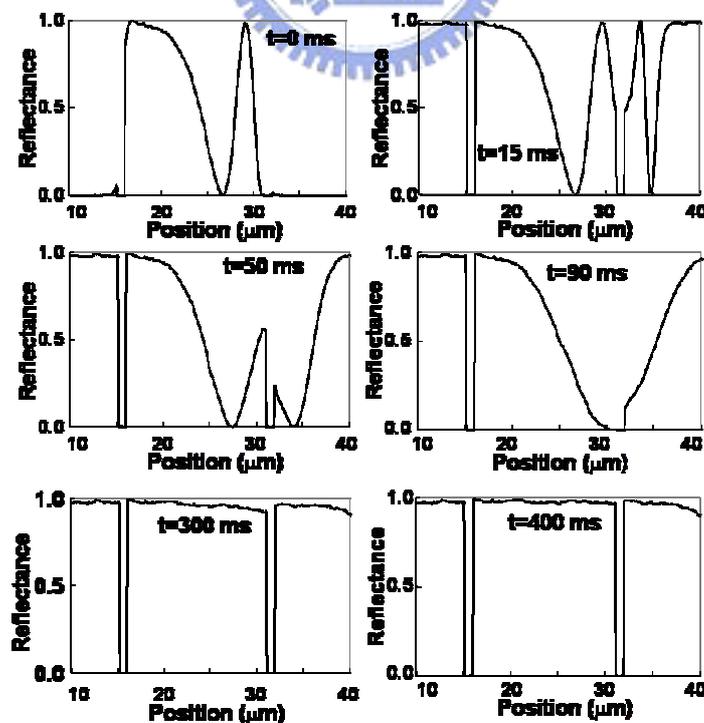


Fig. 3.21 The calculated transient states of VA mode when switching from the dark-bright-dark state to the all bright state. The cell gap is  $2.3\ \mu\text{m}$  and the pretilt angle is  $88^\circ$ .

### 3.5 Conclusion

Detailed analyses on fringing-field effects of twisted and non-twisted LC modes for LCOS devices are presented. Overall speaking, NW MTN modes have weaker fringing-field effect because of the thinner cell gap. However, a uniaxial compensation film is needed to obtain a good dark state at low applied voltage for the twist angle less than  $90^\circ$ . For NB TN modes, the fringing-field effect is strong due to the thick cell gap. Reducing cell gap can minimize the fringing fields effectively and improve contrast ratio. However, high birefringence material must be used to satisfy the large  $d\Delta n$  requirement. Adding chiral dopant for improving reflectance would cause severe disorders of the LC directors. The tradeoff may not be worth of taking.

For non-twisted LC operation modes, FCH and VA cells were analyzed. For FCH mode, the dark state needs to be compensated using a retardation film. Although the low  $d\Delta n$  value guarantees a fast response time, the light leakages caused by fringing fields significantly decrease the image quality of this mode. For VA mode, the contrast ratio is very high due to the extremely small residual phase in the voltage-off state. The main problem of VA mode is that the strong fringing field produces a broad dark line in the bright pixels in the dark-bright-dark pixel configurations. The dark lines decrease the optical efficiency drastically. Furthermore, the transient states evolution of the disclination line in VA mode is very slow after changing the applied voltages. This would blur the dynamic images.

The influences of pixel pitch, cell gap, pretilt angle and electrode slope to the optical performance of LCOS devices are also discussed in this chapter. Based on the simulated results, smaller pixel pitch presents stronger fringing-field effect. Decreasing cell gap effectively reduce the fringing-field effect in TN modes. However, the requirement of high birefringence LC material limits its application. Lowering pretilt angle in VA mode can

slightly release the fringing-field effect. The tradeoff of lower contrast ratio in this condition may not be worth taken. The electrode slope is also an important factor to fringing-field effect. It was demonstrated that the sharp electrode gives the best performance for VA, 90°-MTN and 45°-MTN modes.

Table 3.2 compares the performance of the LC operation modes that we have analyzed. We found that two of them are especially attractive for LCOS applications. First, the 45°-MTN mode has the advantages of high reflectance, high optical filled factor and relatively weak fringing-field effect. Furthermore, the fast response makes it particularly suitable for time-sequential devices. Second, when considerations all come to contrast ratio, VA mode is still very promising. The main drawback is its strong fringing-field effects in both static and transient states. A novel VA-LCOS device utilizing the properties of circularly polarized light has successfully eliminated the fringing-field-caused problem as will be introduced in the next chapter.

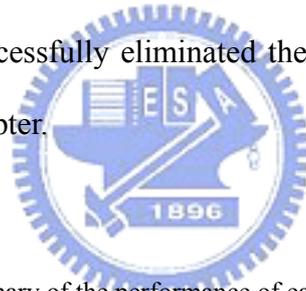


Table 3.2 Summary of the performance of each LC operation mode.

	90°-MTN	63.6°-MTN	45°-MTN	63.6°-TN	45°-TN	52°-TN	VA	FCH
Optical Filled Factor (%)	84.7	92.7	96.7	70.6	70.6	79.6	70.2	98.3
Max Reflectance(%)	87	99	100	100	96	100	100	100
Contrast Ratio (checkerboard)	261	87	178	14	51	55	298	93
Viewing Cone (1000:1)	8°	11°	10°	12°	10°	10°	22°	
Fringing Field Effect	Weak	Normal	Normal	Severe	Strong	Strong	Severe	Normal
Others Issues		need film	need film	need high birefringence	need high birefringence	need high birefringence	Need c-plate	need film

## References

- [1] S. T. Wu and C. S. Wu, *Appl. Phys. Lett.* **68**, 1455 (1996).
- [2] M. Schadt and W. Helfrich, "Voltage-dependent optical activity of a twisted nematic liquid crystal." *Appl. Phys. Lett.* **18**, 127 (1971).
- [3] S. T. Wu and C. S. Wu, "A biaxial film-compensated thin homogenous cell for reflective liquid crystal display." *J. Appl. Phys.* **83**, 4096 (1998).
- [4] M. F. Schiekkel and K. Fahewnschon, *Appl. Phys. Lett.* **19**, 391 (1971).
- [5] S. T. Wu, C. S. Wu and C. L. Kuo, *Jpn. J. Appl. Phys.* **36**, pp.2721 (1997).
- [6] S. T. Wu and D. K. Yang, *Reflective Liquid Crystal Displays* (Wiley-SID, New York, 2001).
- [7] T. Sonehara, *Jpn. J. Appl. Phys.* **29**, L1231 (1990).
- [8] P. Janssen, J. A. Shimizu, J. Dean and R. Albu, *Displays* **23**, 99 (2002).
- [9] T. Sonehara and O. Okumura, *Japan Display '89*, pp.192 (1989).
- [10] J. Grinberg, A. Jacobson, W. Bleha, L. Boswell, G. Myer, *Opt. Eng.* **14**, 217 (1975).
- [11] X. Zhu and S. T. Wu, "Normally black reflective twisted-nematic cell for microdisplay application." *J. Appl. Phys.* **95**, 7660 (2004).
- [12] M. L. Jepsen, M. J. Ammer, M. Bolotski, J. J. Drolet, A. Gupta, Y. Lai, D. Huffman, H. Shi and C. Vieri, "High resolution LCOS microdisplay for single-, double- or triple-panel projection systems." *Displays* **23**, pp. 109 (2002).
- [13] Y. Ji, J. Gandhi and M. Stefanov, *Soc. Information Display Tech. Digest* **30**, 750 (1999).
- [14] D. Cuypers, H. De Smet, A. Van Calster, *Intl. Display Workshop '04*, p.1679 (2004).
- [15] Kuan-Hsu Fan Chiang, Shin-Tson Wu and Shu-Hsia Chen, *Intl. Display Workshop '01*, p.1723 (2001).
- [16] K. H. Fan Chiang, S. T. Wu, and S. H. Chen, *Jpn. J. Appl. Phys.* **41**, 4577 (2002).

[17] S. Zhang, M. Lu, and K. H. Yang, *Soc. Information Display Tech. Digest*, **31**, 898 (2000).

[18] M. Lu and K. H. Yang, *Asian Soc. Information Display Tech. Digest*, **31**, 30 (2000).



## Chapter 4

# Circularly Polarized Light Illuminated Vertically Aligned LCOS Device

### 4.1 Introduction

The influences of the fringing-field effect in different LC modes have been investigated in the last chapter. Among them, the vertically aligned (VA) LCOS is particularly promising because of its inherent high contrast ratio. However, the light loss of a VA-LCOS due to the fringing-field effect is relatively high ( $>30\%$ ) when a linearly polarized light is employed [1,2]; this device is abbreviated as LPVA cell for convenience. Hence, the sharpness and brightness of the displayed images are deteriorated tremendously. Moreover, the optical transition time of the LPVA LCOS switched from the alternate bright and dark states to the all-bright state is extremely slow which results in blurred images as have been already mentioned previously [3,4].

In this chapter, we demonstrate a novel device called the circularly polarized light illuminated vertically aligned (CPVA) liquid crystal cell which not only preserves the light in the presence of the lateral fringing field but also gives a fast optical switching time ( $<10$  ms) to eliminate the blurring of the moving images [5,6]. We first simulate the LC directors distribution and optical performances of the CPVA and the LPVA cells and then apply the de Vries theory to interpret these optical properties. Finally, we present the confirming experimental results using a LCOS device.

Although our analyses are concentrated on the reflective LCOS devices because of their severe fringing-field effect, these treatments can be applied equally well to the transmissive microdisplays, such as HTPS and LTPS panels.

## 4.2 Simulation results

Figures 4.1 (a) and (b) depict the optical configurations used for the CPVA and LPCA device studies, respectively. As shown in Fig. 4.1 (a), the incident light is linearly polarized by a polarizing beam splitter (PBS) along the x-axis. The light will then traverse through the LC layer, whose rubbing direction deviates from the x-axis by an angle  $\beta=45^\circ$ .

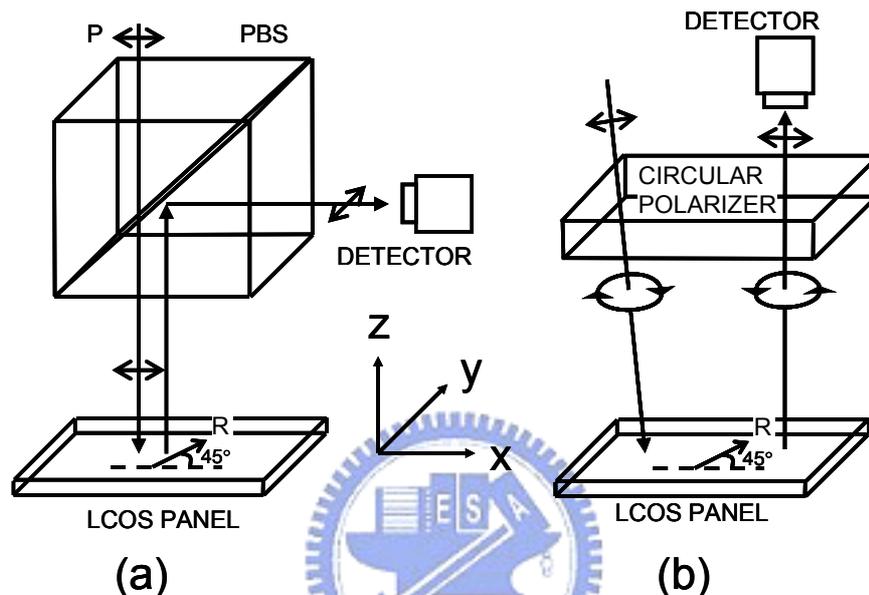


Fig. 4.1 Schematic drawing of the systems used for (a) the LPVA device and (b) the CPVA device. PBS=polarizing beam splitter; P=polarization axis, R is the LC alignment direction at the front surface.

The reflective pixel electrodes fabricated in the device will reflect the light back to the LC layer. After passing the LC layer the second time, the outgoing light will be analyzed by the PBS and directed to the detector. For the CPVA device, a broadband circular polarizer is used instead of the PBS, as shown in Fig. 4.1 (b). Therefore, the incident light is circularly polarized and modulated by the LC cell. After traversing through the LC layer twice, the light will be analyzed by the same circular polarizer and directed to the detector. For the following simulations and experimental results, the LCOS panel is operated at the alternate bright and dark states with the on-state voltage  $V_{on}=5$  V and the off-state voltage  $V_{off}=0$  V. Here the turn-on voltage corresponds to the maximum reflectance. The pixel size is  $11.5 \mu\text{m}$ , the inter-pixel gap is  $0.5 \mu\text{m}$ , and the cell gap  $d=2.6 \mu\text{m}$ . The LC pretilt angle  $\theta=88^\circ$

and the LC material used for simulations is Merck MLC-6608; its extraordinary refractive index  $n_e=1.5578$ , ordinary refractive index  $n_o=1.4748$ , and dielectric anisotropy  $\Delta\epsilon=-4.2$ .

Figure 4.2 presents the simulated results of the LC director distribution and the corresponding reflectance profiles,  $R_{CP}(x)$  [top] and  $R_{LP}(x)$  [middle], at the dark-bright-dark state [bottom] for the CPVA and the LPVA systems. And Fig. 4.3 shows the calculated azimuthal angles ( $\phi$ ) of the LC directors along the z direction at the specified x positions,  $x=x_1, x_a, x_b$  and  $x_2$  as denoted in Fig. 4.2. From Fig. 4.2, the fringing fields penetrate into the voltage-off pixels from both right and left edges of the voltage-on pixel. Without the electric field, the director  $\mathbf{n}$  of this vertically aligned cell is parallel in a plane with an azimuthal angle of  $45^\circ$  from the x-axis. With the field on, the LC directors on the substrate surfaces are pinned due to the strong anchoring boundary condition. The largest polar angle appears near the middle plane because the negative type ( $\Delta\epsilon<0$ ) LC molecules tend to orient themselves perpendicular to the electric field. Therefore, the director profile can be regarded as a screw-like structure with its helical axis along z-axis and have opposite rotational sense in the upper and lower parts.

With regard to the optical properties, it is shown in Fig. 4.2 that there are two LC domains separated at  $x_b$ , where the dark line occurs on the bright pixel of the LPVA system. At  $x_b$ , nearly all the directors are aligned in the y direction. On the left and right sides, the directors have their maximum twist angles smaller and larger than  $45^\circ$ , respectively. In the LPVA cell, a reflectance peak is displayed in each domain, i.e.  $R_{LP}(x_a)$  and  $R_{LP}(x_2)$ , while  $R_{LP}(x_b)$  displaying a minimum reflectance. The  $R_{LP}(x)$  is lying between  $R_{LP}(x_a)$  (which is  $\sim R_{LP}(x_2)$ ), and  $R_{LP}(x_b)$  in the rest area of the voltage-on pixel. The accumulated light loss is as high as 30%. On the contrary,  $R_{CP}(x)$  is not influenced by the director distortions in the x-y plane leading to a high sharpness and high brightness image in the CPVA cell.

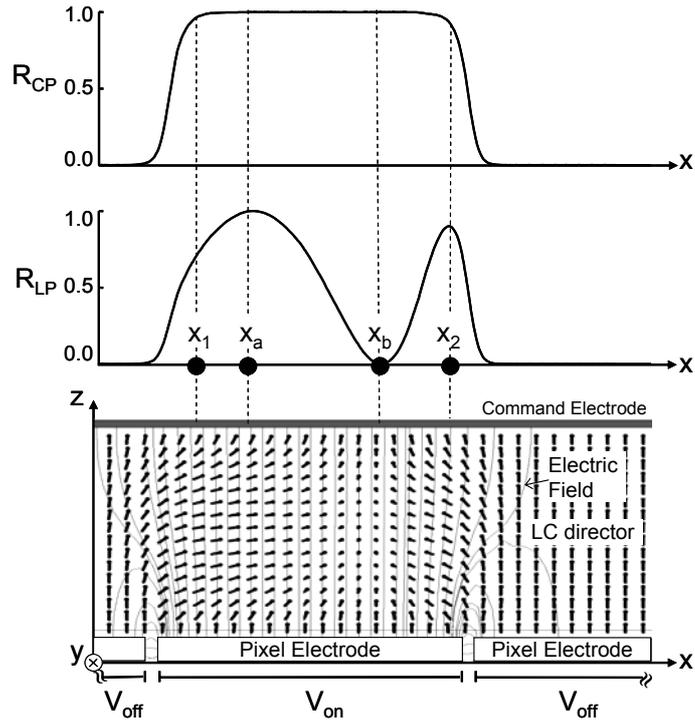


Fig. 4.2 The simulated LC director distribution and the corresponding reflectance profiles,  $R_{LP}(x)$  and  $R_{CP}(x)$ , at the alternate dark and bright state for the CPVA and the LPVA systems, respectively. The on-state voltage  $V_{on}=5$  V and the off-state voltage  $V_{off}=0$ .

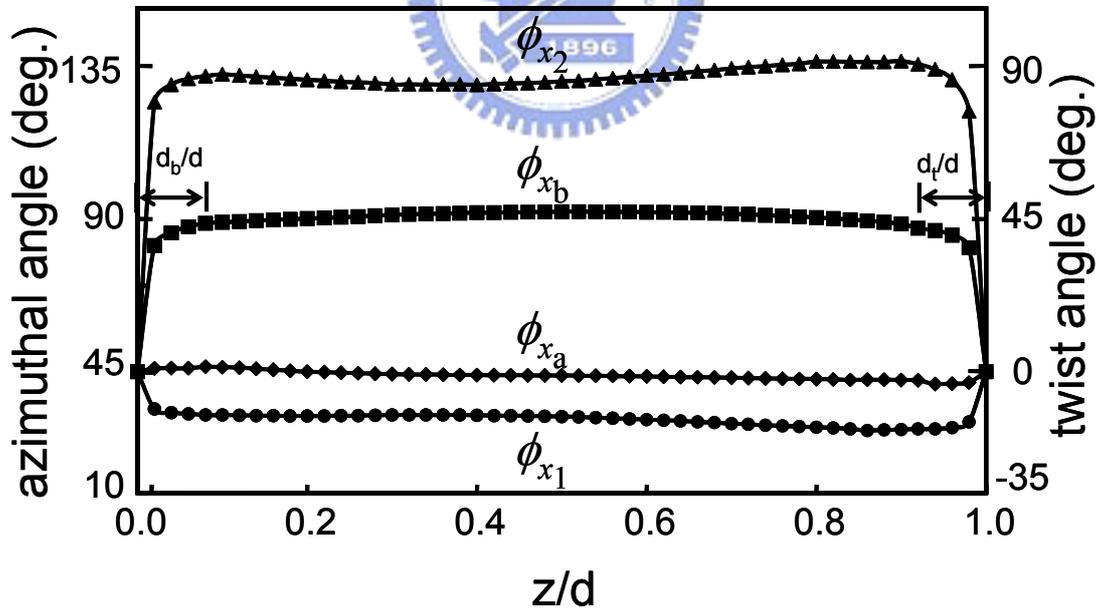


Fig. 4.3 Calculated azimuthal angles ( $\phi$ ) of the LC directors along the  $z$  direction at  $x=x_1, x_a, x_b$  and  $x_2$  as denoted in Fig. 4.2.

### 4.3 Theoretical interpretation

As mentioned above, the LC director profile can be regarded as a screw-like structure with spatially varying pitch,  $P_0(z)$ . Some studies have been made in such structure with different models of  $P_0(z)$  [7,8]. Here we interpret the optical properties qualitatively by de Vries theory [9-11] for simplicity. Assuming a wave propagates along the helical axis of an ideal helical structure with a fixed pitch  $P_0$ . In general, there are two eigenwaves propagating in the same direction. Their eigenvalues  $l_i$ ,  $i=1,2$ , satisfy the dispersion relation which can be derived from solving the Maxwell's equations supplemented by the constitutive equation as derived in Chap. 2:

$$(-k_0^2 + l_i^2 + q_0^2)^2 - 4q_0^2 l_i^2 - k_1^4 = 0 \quad (4.1)$$

where

$$k_0^2 = \left(\frac{2\pi}{\lambda}\right)^2 \frac{(n_e^2 + n_o^2)}{2} \quad (4.2)$$

$$k_1^2 = \left(\frac{2\pi}{\lambda}\right)^2 \frac{(n_e^2 - n_o^2)}{2} \quad (4.3)$$



where  $q_0=2\pi/P_0$  and  $\lambda$  is the wavelength of the incident light. When  $P_0$  and  $\lambda$  are known, one can obtain the ellipticity of the eigenwaves as:

$$\rho = \frac{2l_i q_0}{\pm \sqrt{k_1^4 + 4q_0^2 l_i^2} - k_1^2}, \quad (4.4)$$

where  $l_i$  can be derived from Eq. (4.1) as:

$$l_i = \sqrt{k_0^2 + q_0^2 \pm \sqrt{4k_0^2 q_0^2 + k_1^4}} \quad (4.5)$$

The eigenwaves, whose polarization ellipse axes are either parallel or perpendicular to  $\mathbf{n}$ , have their phase difference accumulated to  $(l_1 - l_2)z$ . From Eq. (4.4), if  $P_0 \gg \lambda \gg P_0(n_e - n_o)$ , then  $\rho \rightarrow \pm 1$ . In this regime, the eigenwaves are almost circularly polarized, which means the oscillation direction of a linear wave will be rotated after passing the LC layer. The optical rotatory power  $\psi$  (the amount of rotation per unit length) is given as:

$$\psi = \frac{k_1^4}{8q_0(k_0^2 - q_0^2)} \quad (4.6)$$

Also from Eq. (4.4), if  $\lambda \ll P_0(n_e - n_o)$ , then  $\rho \rightarrow 0$  or  $\infty$ . In this regime, the eigenwaves are almost linearly polarized at the direction parallel or perpendicular to  $\mathbf{n}$ .

In the CPVA system, the light is preserved in the region of  $x_1 < x < x_2$  as presented by the reflectance profile  $R_{cp}(x)$  in Fig. 4.2. This can be understood easily by the above arguments with an approximated model, which is a non-twisted LC layer sandwiched between two twisted layers. In Fig. 4.3, the twisted regimes near the substrates ( $0 < z < d_b$ ) and ( $d_t < z < d$ ) having their eigenwaves circularly polarized since the effective pitch ( $1.32\mu\text{m} < |P_0| < 1.87\mu\text{m}$ ) satisfies the condition of  $P_0 \gg \lambda \gg P_0(n_e - n_o)$  for the visible light. The circularly polarized light remains its polarization state after passing the top-twisted regime. Note that a circularly polarized light can be regarded as the superposition of any two orthogonal linearly polarized waves with the same amplitude and  $\pi/2$  phase difference. The non-twisted uniform regime ( $d_b < z < d - d_t$ ), as shown in Fig. 4.3, with linearly polarized eigenwaves provides a phase difference, say  $\delta = \pi/2$ , such that the resulted light is linearly polarized in the direction at  $45^\circ$  from  $\mathbf{n}$ . The reflected light that traverses through the bottom-twisted regime twice (forwardly and backwardly) will have the same linear polarization. Then the uniform regime changes it to be circularly polarized by gathering another  $\pi/2$  phase change. The polarization state of the outgoing circular wave will again not be influenced after traversing through the top-twisted regime. Finally, almost all of the light passes through the broadband circular polarizer. In other words, the CPVA system preserves the input light efficiently.

On the contrary, for the LPVA system the input light is linearly polarized in the  $x$  direction. The top-twisted regime will slightly rotate the plane of polarization according to Eq. (4.6). The non-twisted regime will generally change the light to an elliptically polarized light. The characteristic of the polarization ellipse depends on the angle between the local

director  $\mathbf{n}$  and the entering linear wave. At  $x = x_b$ , most directors are aligned parallel in the  $y$  direction. Since the incident light of the non-twisted region is almost linearly polarized in the  $x$  direction, one of the linear eigenwaves has almost zero amplitude while the other remains oscillating in the  $x$  direction after having passed through this region. The reflected light that traverses through the bottom twisted regime twice will maintain the same polarization. i.e. along the  $x$  direction. The light will then traverse through the uniform and the top-twisted regions the second time with its polarization almost unchanged as already discussed above. Eventually, the outgoing light will be blocked by the analyzer resulting in a minimum reflectance,  $R_{LP}(x_b)$ . At  $x = x_a$  as shown in Fig. 4.3, most directors without twist deformation are aligned in the  $45^\circ$  direction with respect to the  $x$ -axis. Therefore, the two linear eigenwaves have almost the same amplitudes in this regime. By gathering a  $\pi$  phase change after passing through the LC layer twice, the outgoing light will be linearly polarized at the direction nearly perpendicular to that of the incident light, which results in a maximum reflectance  $R_{LP}(x_a)$ . The reflectance for the rest area can be deduced from the same model and the results are in between  $R_{LP}(x_a)$  and  $R_{LP}(x_b)$ .

## 4.4 Experimental results

Figures 4.4 (a) and (b) depict the experimental results when the panel is operated at the alternating bright and dark states for the LPVA and the CPVA devices, respectively. The photos were captured by CCD through an optical polarizing microscope. It is clearly shown that the image of the LPVA device is degraded by the fringing-field-effect severely. The dark lines in the bright pixels originate from the distortion of the LC director profile illustrated in Figs. 4.2 and 4.3. By contrast, Fig. 4.4(b) shows that the dark lines are totally eliminated in the CPVA device. Therefore, the sharpness and the brightness of the displayed images are enhanced significantly.

The CPVA optical system not only improves the static performance but also dramatically reduces the dynamic response time of the LCOS panel. Figures 4.4 (c) and (d) show the photos of the LC panel switched from the alternate bright and dark states to the all-bright state for the LPVA and the CPVA devices, respectively. The elapsed time after switching is 198 ms in Fig. 4.4 (c) and 33 ms in Fig. 4.4 (d). The distorted LC directors take extremely long time to relax back to the original state. The dark lines in the LPVA device last for at least several hundred milliseconds after switching which causes a serious image blurring effect. Since the distorted LC directors are mainly rotating in the x-y plane during the relaxation process, the influence on the optical response of the CPVA device is very small. Figure 4.5 shows the measured reflectance with respect to the elapsed time after switching from the alternate bright and dark states to the all-bright state for the CPVA device. The result indicates that the transition time is less than 10 ms.

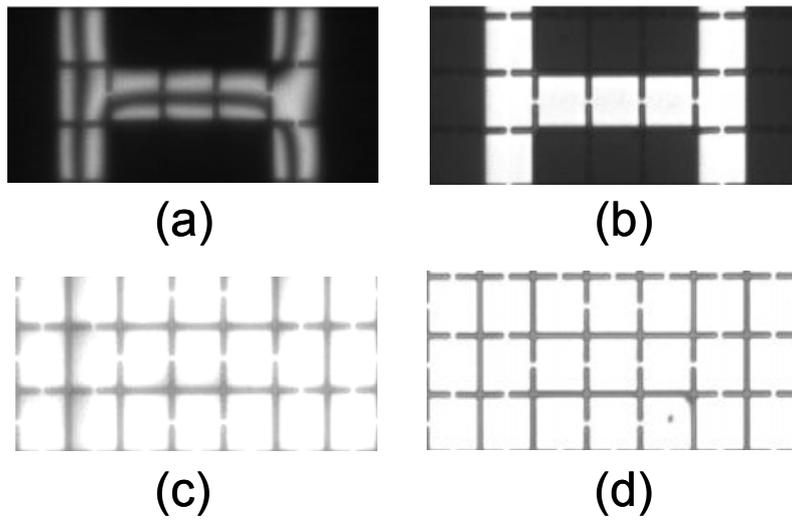


Fig. 4.4 Photos captured by CCD through the polarizing microscope of the LC panel operated at the alternate bright and dark states for (a) the LPVA and (b) the CPVA devices. Photos of the LC panel switched from the alternate bright and dark states to the all-bright state for (c) the LPVA device at 198 ms after switching and (d) the CPVA device at 33 ms after switching.

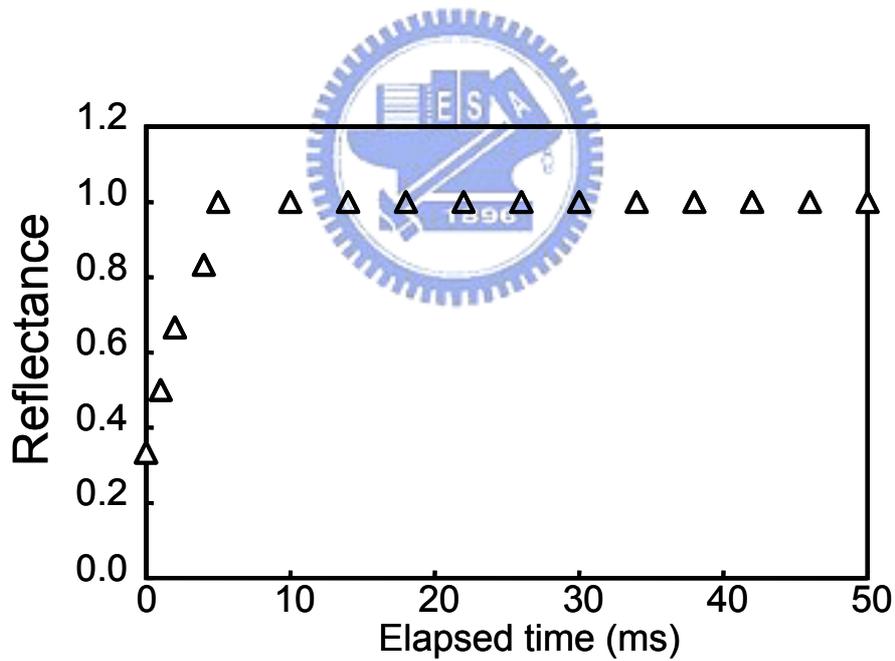


Fig. 4.5 Measured reflectance with respect to the elapsed time after switching from the alternate bright and dark states to the all-bright state for the CPVA device.

## 4.5 Optical engines for CPVA device

A circularly polarizer (CP) can be easily formed by combining a linear polarizer (LP) and a quarter-wave plate with a 45 degree angle between their optical axes. In order to widen the bandwidth of a CP, a half-wave plate is usually inserted between the LP and the quarter-wave plate [12]. The relative directions of their optical axes are arranged as in Fig. 4.6. Note that the incident light (I) and the reflective light (R) have the same polarization state, which means that PBS are not able to separate the incident light and the signal light in this condition.

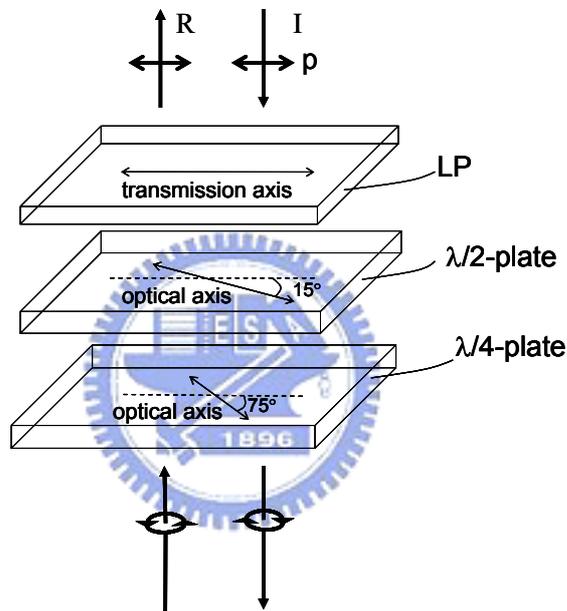


Fig. 4.6 Sketch of the broadband circular polarizer which comprises a linear polarizer, a  $1/2\lambda$ -plate and a  $1/4\lambda$ -plate.

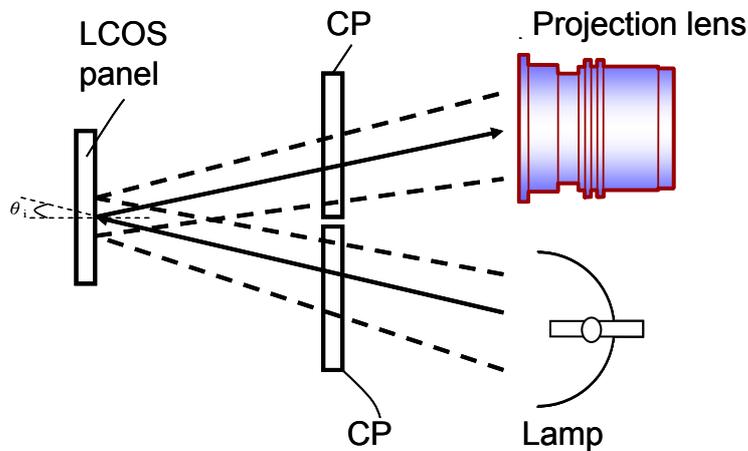


Fig. 4.7 The off-axis optical system for reflective CPVA device.

One available optical engine for CPVA device is the off-axis system as shown in Fig. 4.7. This design was developed by Aurora corp.[13] As shown in the figure, the light is incident on the LCOS panel with an oblique angle  $\theta_i$ . The reflected light will be directed to the projection lens with a different optical path. A broadband CP is placed on the incident path to generate circularly polarized light, and another CP is placed on the reflective path to analyze the signal light. It is obvious that the incident light and the signal light can be separated regardless of their polarization states. However, the off-axis design is more complicated and the viewing angle properties of the LCOS panel become more critical.

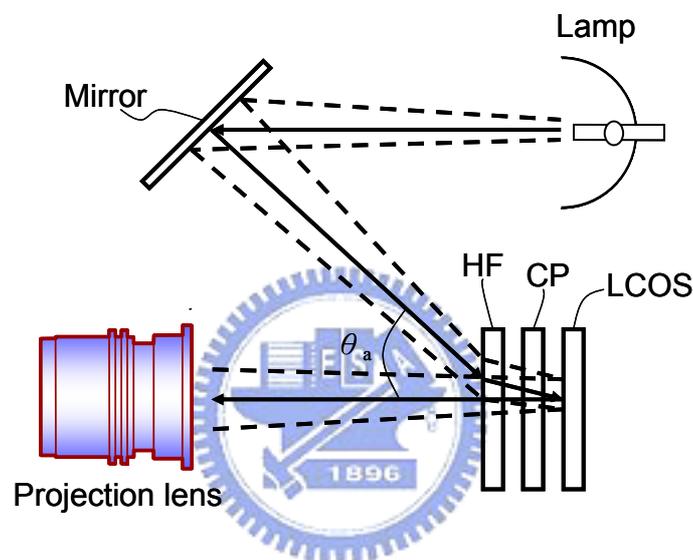


Fig. 4.8 The optical system using hologram film for reflective CPVA device.

Another candidate of the optical engine is the one using hologram film (HF) as shown in Fig. 4.8. This system was first presented by JVC corp. as mentioned in Chap. 1. By appropriately designing the HF, the oblique incident light that passes through it will be directed to the LCOS panel in the normal direction. A broadband CP is placed between the HF and the LCOS panel to generate the circularly polarized light. The reflected light will be analyzed by the same CP and pass through the HF again without any interference. Finally, the signal light will enter the projection lens. It is noteworthy that JVC's design was intended for one panel system. Therefore, the alignment of the HF is very critical in order to direct the R, G, B light into their corresponding subpixels. This issue can be ignored in the CPVA system because the three-panel engine can be employed. It was shown that the

light efficiency of the HF for single-panel system can reach 40% [14]. It is believed that by optimizing the HF based on Kogelnik's theory [15], the light efficiency can be much higher for the CPVA system.

The third design of CPVA's optical system consist a Faraday rotator between the broadband CP and the PBS as sketched in Fig. 4.9. In this case, the normal-incident condition is preserved. The plane of polarization of the incident light will be rotated by an angle  $\theta_f$  after it passes through Faraday rotator [16].  $\theta_f$  can be controlled by external magnetic field  $B$  as:

$$\theta_f = V_d B l \tag{4.7}$$

where  $V_d$  is the Verdet constant and  $l$  is the length of the rotator along the light propagating direction. The light will then encounter the broadband CP and the LCOS panel. After modulated by the LC layer, the reflected light will pass through the Faraday rotator again. Therefore, the total rotation angle will be  $2\theta_f$ . By setting  $\theta_f=45^\circ$ , the plane of polarization can be rotated by  $90^\circ$  which is identical to the condition of LP system. Therefore, the PBS can be employed to direct the signal light to the projection lens.

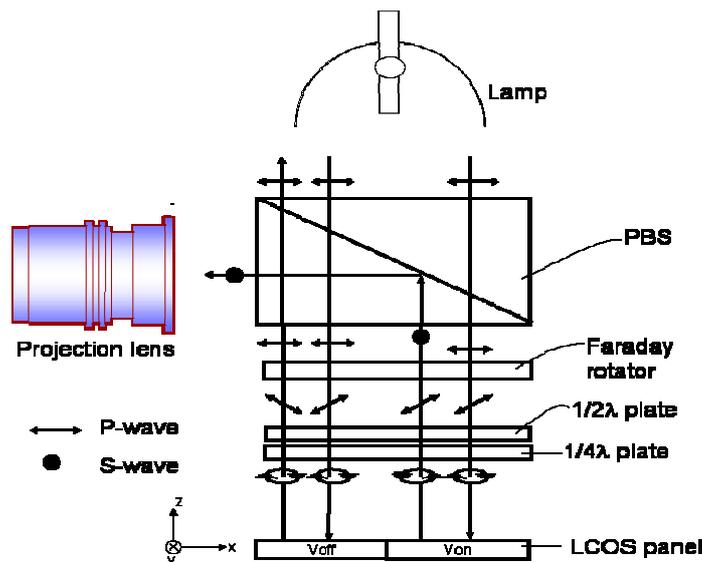


Fig. 4.9 The optical system using Faraday rotator for reflective CPVA device.

The transmissive CPVA optical engine is sketched in Fig. 4.10. As shown in the figure,

the system is simply formed by each LC panel sandwiched by two CPs. Despite of that, there is no additional modification on the optical engine. The simplicity of the transmissive CPVA system makes it more promising for the high-definition projection displays.

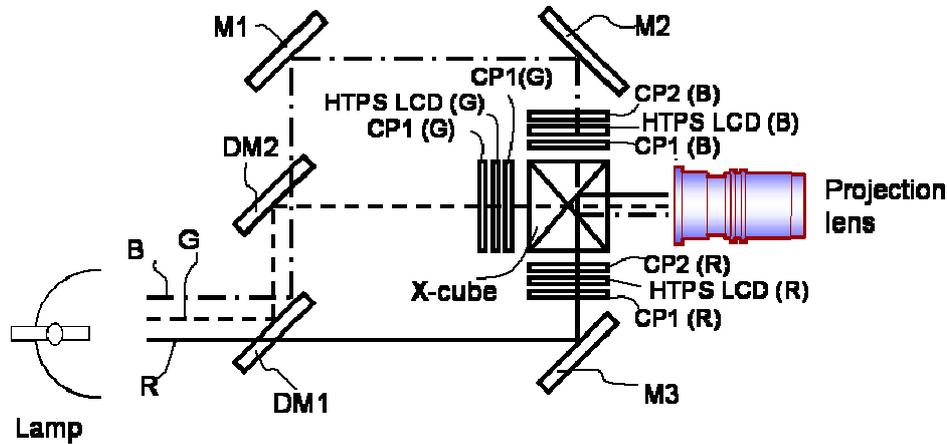


Fig. 4.10 The three-panel optical system for transmissive CPVA high-temperature poly-Si LCD.

## 4.6 Conclusion

We have demonstrated a circularly polarized light illuminated vertically aligned LCOS microdisplay. The long standing problems of poor sharpness and low brightness in the conventional device illuminated by a linearly polarized light are successfully overcome. Furthermore, the dynamic transition time of the CPVA device switched from the alternate bright and dark states to the all-bright state is less than 10 ms, which is adequate to eliminate the blurring of moving images in the LPVA device. The optical properties are interpreted qualitatively by the de Vries theory. Applicable optical engines for CPVA devices are also discussed. Potential applications of this device for high contrast and high optical efficiency reflective LCOS and transmissive p-Si TFT-LCD projection displays are foreseeable.

## References

- [1] Y. Ji, J. Gandhi and M. Stefanov, *Soc. Information Display Tech. Digest* **30**, 750 (1999).
- [2] K. H. Fan Chiang, S. T. Wu, and S. H. Chen, *Jpn. J. Appl. Phys.* **41**, pp.4577 (2002).
- [3] S. Zhang, M. Lu, and K. H. Yang, *Soc. Information Display Tech. Digest*, **31**, 898 (2000).
- [4] M. Lu and K. H. Yang, *Asian Soc. Information Display Tech. Digest*, **31**, 30 (2000).
- [5] K. H. Fan Chiang, X. Zhu, S. T. Wu and S. H. Chen, *Soc. Information Display Tech. Digest*, paper 35.1 (2005).
- [6] Kuan-Hsu Fan Chiang, Shin-Tson Wu and Shu-Hsia Chen, “High-definition vertically-aligned liquid crystal microdisplays using a circularly-polarized light”, submitted to *Appl. Phys. Lett.*
- [7] Z. Lu, L. Li, H. Vithana, Y. Jiang and S. M. Faris, *Mol. Cryst. Liq. Cryst.* **301**, 237 (1997).
- [8] S. Kutter and M. Warner, *Eur. Phys. J. E* **12**, 515 (2003)
- [9] H. de Vries, *Acta Crystallogr.*, **4**, pp.219 (1951).
- [10] P. G. de Gennes and J. Prost. *The Physics of Liquid Crystals 2<sup>nd</sup> Edition* (Clarendo Press, 1993).
- [11] P. Yeh and C. Gu, *Optics of Liquid Crystal Displays* (John Wiley & Sons, 1999).
- [12] T. H. Yoon, G. D. Lee and J. C. Kim, *Opt. Lett.* **25**, 1547 (2000).
- [13] B.A. Scott and W. L. DeBoynton, “Light separation and recombination for an off-axis projector.” U.S. patent 6,046,858 (2000).
- [14] T. Yamazaki, M. Tokumi, T. Suzuki, S. Nakagaki and S. Shimizu, “The Single-Panel D-ILA Hologram Device for ILA<sup>TM</sup> Projection TV.” *Intl. Display Workshop*, pp. 1077, (2000).

- [15] H. Kogelnik, "Couple Wave Theory for Thick Hologram Gratings." *Bell. Syst. Tch. J.* **48**, pp.2909 (1969).
- [16] G. R. Fowles, *Introduction to Modern Optics 2<sup>nd</sup> Edition* (Holt, Rinehart, and Winston, Inc., 1975).



## Chapter 5

# Diffraction Effect of the LCOS Devices

### 5.1 Introduction

In projection displays, compactness is favorable when designing optical engine. Therefore, the dimensions of the optical parts and the LCOS panels need to be as small as possible. In order to maintain high resolution on such small panels, the pixel pitch fabricated on the silicon backplane can be made comparable to the wavelength of visible light. In this condition, the periodic pixel electrodes function as a reflective grating which causes significant light scattering and diffraction effect. The diffraction light propagates along the direction deviated from the axis of optical system may not enter the projection lenses and cause severe light loss. In order to analyze the diffraction effect of LCOS devices, a rigorous simulation method is needed when analyzing the performance of a LCOS panel. The conventional matrix-type methods based on the assumption of stratified medium are no longer suitable in this condition. As introduced in Chap. 2, the extended beam propagation method for optical simulations of reflective liquid crystal display is developed [1,2]. This diffraction-included method is especially helpful for predicting the optical performance of high-definition liquid crystal displays [3-6]. In this chapter, we analyze the effect of diffraction on light efficiency of the optical system. The influence of pixel pitch to the efficiency is also investigated. Based on the simulated results, the diffraction effect can be compensated for some specific wavebands when adjusting the structure parameter of LCOS panel appropriately.

## 5.2 The influence of the pixel pitch to the light efficiency

From the derivation in Chap.2, the field components of reflective waves can be obtained using the extended beam propagation method. It is important to further investigate the angular distribution of the light intensity, which is called the intensity angular spectrum. By using the Fourier transform, the amplitude angular spectra,  $A_{x,y}(\frac{\alpha}{\lambda})$ , of the transverse fields,  $E'_x$  and  $E'_y$ , are given as follows [7]:

$$A_{x,y}(\frac{\alpha}{\lambda}) = \int E'_{x,y} \exp[j2\pi \cos(\frac{\pi/2 - \cos^{-1} \alpha}{\lambda} x)] dx, \quad (5.1)$$

where  $\lambda$  is the light wavelength in the propagating medium and  $\alpha$  represents the cosine of the beam propagating direction depicted in Fig.4.1.

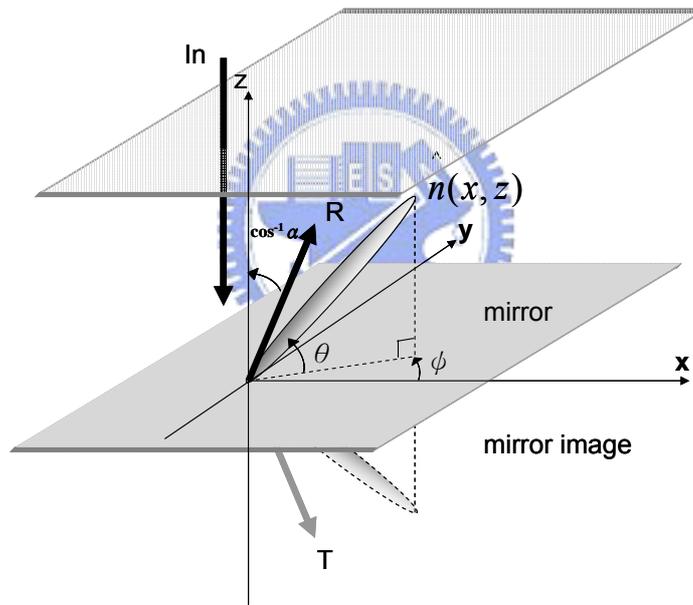


Fig. 5.1 Schematic representation of angle definitions and mirror image of reflective LCOS device.

Finally, the output intensity angular spectrum is expressed as:

$$I(\frac{\alpha}{\lambda}) = A_x^2 + A_y^2 \quad (5.2)$$

Equation (4.2) represents the spectrum of the light at the end of the propagation which is prior to enter the cover glass. When considering the spectrum of the light exits from the LC panel, the refraction at the interfaces of the cover glass and the air must be taken into consideration. As a consequence, the final propagating angle,  $\theta_p$ , is given as follows:

$$\theta_p = \sin^{-1}(n_{eff}^r \times \sin(\cos^{-1} \alpha)) \quad (5.3)$$

where the  $n_{eff}^r$  represents the effective refractive index at the end of propagation in the LC layer. We then define the light efficiency of the LCOS optical system as,  $\eta$ , as follows:

$$\eta = \frac{\int_{-\theta_a}^{\theta_a} I\left(\frac{\theta_p}{\lambda}\right)}{I_{in}}, \quad (5.4)$$

where  $I_{in}$  is the intensity of the incident light and  $\theta_a$  represents the acceptance angle of the optical system which is related to the f-number ( $F_{\#}$ ) of the projection lenses:

$$\theta_a = \tan^{-1}\left(\frac{1}{2F_{\#}}\right) \quad (5.5)$$

Figure 5.2 sketches the acceptance angle of the projection lenses.

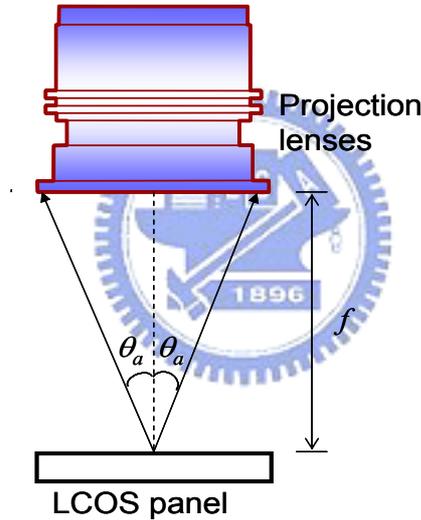


Fig. 5.2 Sketch of the acceptance angle  $\theta_a$  of the light waves propagating from the LCOS panel to the projection lens.

Here we focus on two specific LC operation modes, VA and finger-on-plane (FOP) modes. FOP mode was first developed by Electronics Research & Service Organization (ERSO), Industrial Technology Research Institute (ITRI) [8,9]. The main characteristic of this mode is its tiny common electrodes fabricated on top of the pixel electrodes. Using this specific structure, it can effectively eliminate the fringing-field effect of LCOS panel. However, the tiny common electrodes are found contributive to the diffraction effect and result in a poor light efficiency as will be discussed in the following.

Figure 5.3 shows the cell structures used for the 2D simulations of the LC director distributions and the light efficiencies. The  $d\Delta n$  equals 207.5 nm for the FOP mode and 190.9 nm for the VA mode. The LC parameters used for simulations are based on the commercial material MLC-6608.

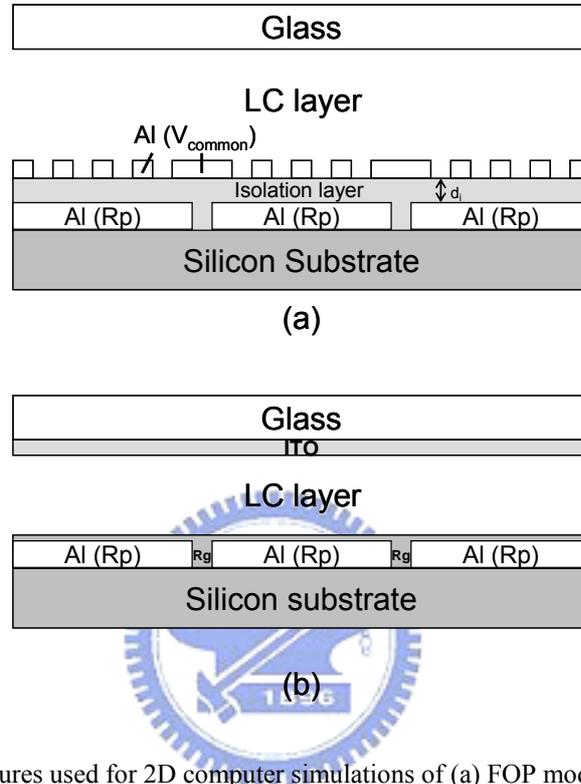


Fig. 5.3 Cell structures used for 2D computer simulations of (a) FOP mode (b) VA mode.

The LCOS panels are both illuminated by a normally incident linearly polarized light. The angles between the direction of polarization and the LC rubbing direction on the top glass are  $0^\circ$  and  $45^\circ$  for the FOP mode and the VA mode, respectively. In our optical engine, we assume  $F_{\#}=2.8$ , which indicates  $\theta_a \sim 10^\circ$  from Eq. (5.5). In order to investigate the influence of the pixel pitch ( $P$ ) to the light efficiency, we varied the  $P/\lambda$  value from 30 to 2.5 with a fixed inter-pixel gap ( $0.7 \mu\text{m}$ ). The LC layer is divided as a grid with the spatial step  $\Delta x=100 \text{ nm}$  and  $\Delta z=50 \text{ nm}$  during the numerical analyses. In simulations, we assume  $R_p=90\%$  and  $R_g=0\%$  for the pixelated aluminum electrodes and absorptive black matrices underneath the interpixel regions, respectively.

Figures 5.4 plots the calculated light efficiencies ( $\theta_a=10^\circ$ ) of the LCOS devices with

respect to the  $P/\lambda$  value when all the pixels are turned off for the FOP. The results calculated by the Jones matrix method are also included in the figures. From Fig. 5.4, the light efficiencies predicted by the BPM are much lower than those given by the Jones matrix method. In reality, the comb-like common electrodes on the bottom substrate of the FOP device are acting as a phase grating. The light waves encountered these electrodes will be scattered and diffracted to various angles. The light waves propagating outside the acceptance angle of the projection lens are wasted. Thus, the overall light efficiency is decreased. It is well known that from the grating formula,  $m\lambda = g \sin \theta$  (where  $m$  is the order of diffraction,  $g$  is the grating pitch, and  $\theta$  is the diffraction angle), the diffraction angle gets larger as the pitch becomes smaller [10]. Therefore, a smaller pixel pitch generally gives a lower light efficiency in LCOS devices. However, some exceptions may occur. For example, when  $P/\lambda=5$  in Fig. 5.4, the diffraction angle of the first order light exceeds the critical angle of the total internal reflection at the glass-air interface. Hence, the energy will not escape from the device leading to a higher light efficiency than the larger  $P/\lambda$  case.

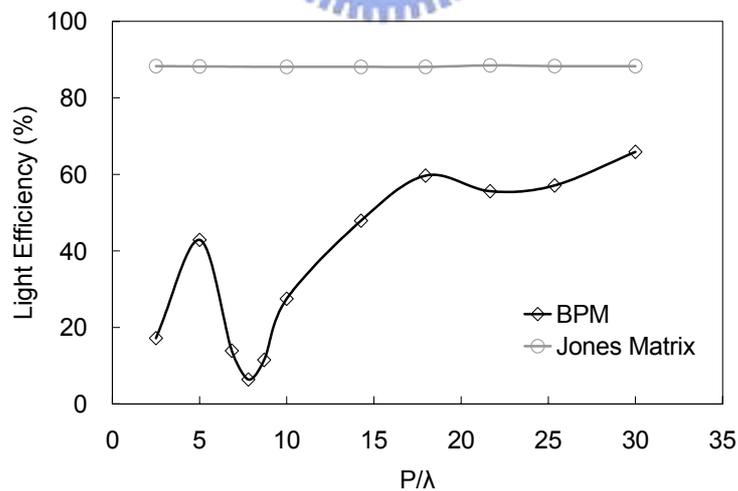


Fig. 5.4 Computer simulated light efficiencies ( $\theta_a=10^\circ$ ) with respect to  $P/\lambda$  value of FOP-LCOS devices at voltage-off state by extended BPM and Jones matrix method.

We have shown that the BPM describes reasonably well the optical behavior of the FOP device. The Jones matrix results maintain almost identical for different pixel pitch and

are much higher than those obtained from BPM. Basically, the Jones matrix method treats the bottom substrate only as a specular reflector. Figure 5.5 shows the intensity angular spectrum calculated by both methods with  $P=7.7\ \mu\text{m}$  and  $\lambda=540\ \text{nm}$ . It can be easily seen that without considering the diffraction effect, the signal light waves mainly propagate along the normal direction, which will cause an unbearable error in the real system.

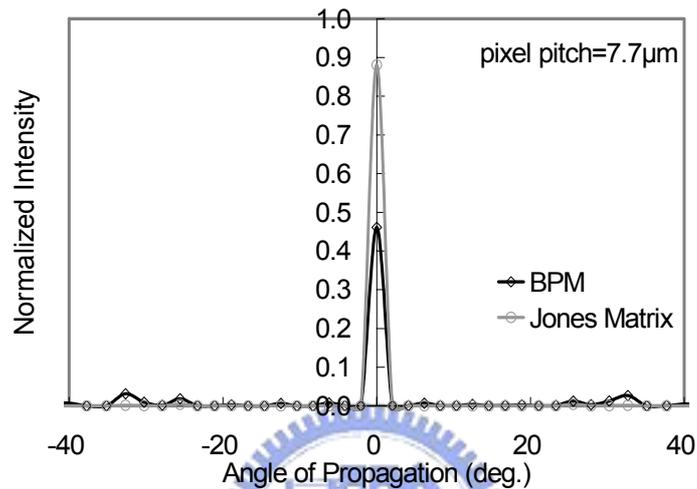


Fig. 5.5 Simulated intensity angular spectrum with  $P=7.7\ \mu\text{m}$  and  $\lambda=540\ \text{nm}$  for FOP mode.

In the case of VA mode, an absorption material (black matrix) is employed underneath the inter-pixel gaps. In the voltage-off state, the device is acting as a slit grating. The calculated light efficiencies from the BPM and the Jones matrix method are almost the same as shown in Figs. 5.6 (a) and (b). The light efficiency calculated by Jones Matrix depends on  $P/\lambda$  because of the influence of the dark inter-pixel gaps. These dark gaps act as slits and generate periodic intensity profiles of the signal light. Therefore, the diffraction effect induced by these gaps can still be analyzed via the angular spectrum even though the fields are calculated by the Jones matrix method. However, when the voltages between the adjacent pixels are different, which is common seen when an image is displayed, the diffraction and scattering induced by phase difference and the variation of LC directors are not included by using the Jones matrix method. Therefore, we simulated the extreme case in which one pixel is on and its adjacent pixels are off, i.e. the off-on-off configuration.

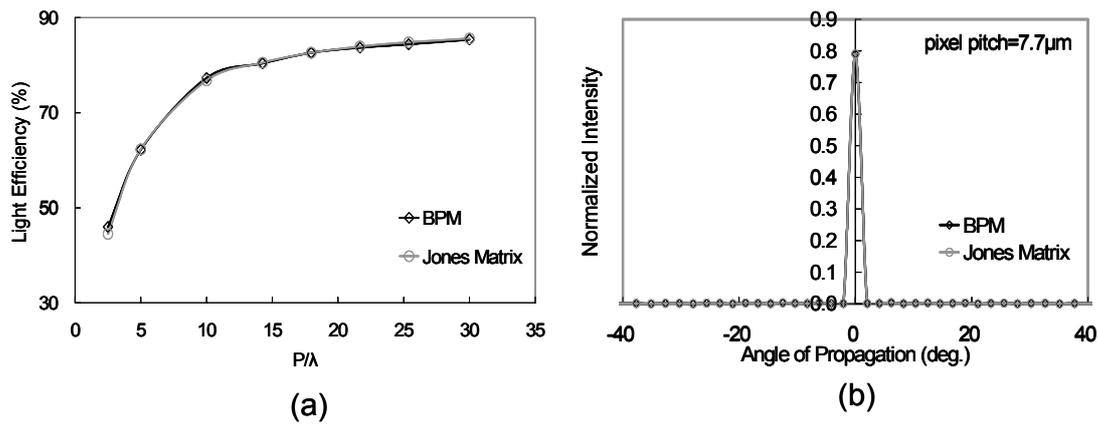


Fig. 5.6 (a) Simulated light efficiencies with respect to  $P/\lambda$  value of VA-LCOS devices at voltage-off state by extended BPM and Jones matrix method, and (b) simulated intensity angular spectrum with  $P=7.7 \mu\text{m}$  and  $\lambda=540 \text{ nm}$ .

Figure 5.7 (a) shows the calculated light efficiencies of the VA device as a function of  $P/\lambda$ . Although this figure still shows almost identical results between the two methods, the optical behaviors are very different. Figure 5.7 (b) shows the calculated intensity angular spectra with  $P=7.7 \mu\text{m}$  and  $\lambda=540 \text{ nm}$ . As shown in the figure, the intensities of the signal light near the normal direction calculated by the BPM are much lower than those by the Jones matrix method. The intensity of the zeroth order diffracted light,  $I_0$ , is also calculated with respect to the  $P/\lambda$  value as shown in Fig. 5.7 (c). The  $I_0$  calculated by the BPM is always lower due to the light scattering and diffraction by the various LC orientations around the pixel edges. These results are especially important for designing a projection display, because accurately predicting the angular distribution of the light intensity can prevent many unwanted image aberrations in the optical system.

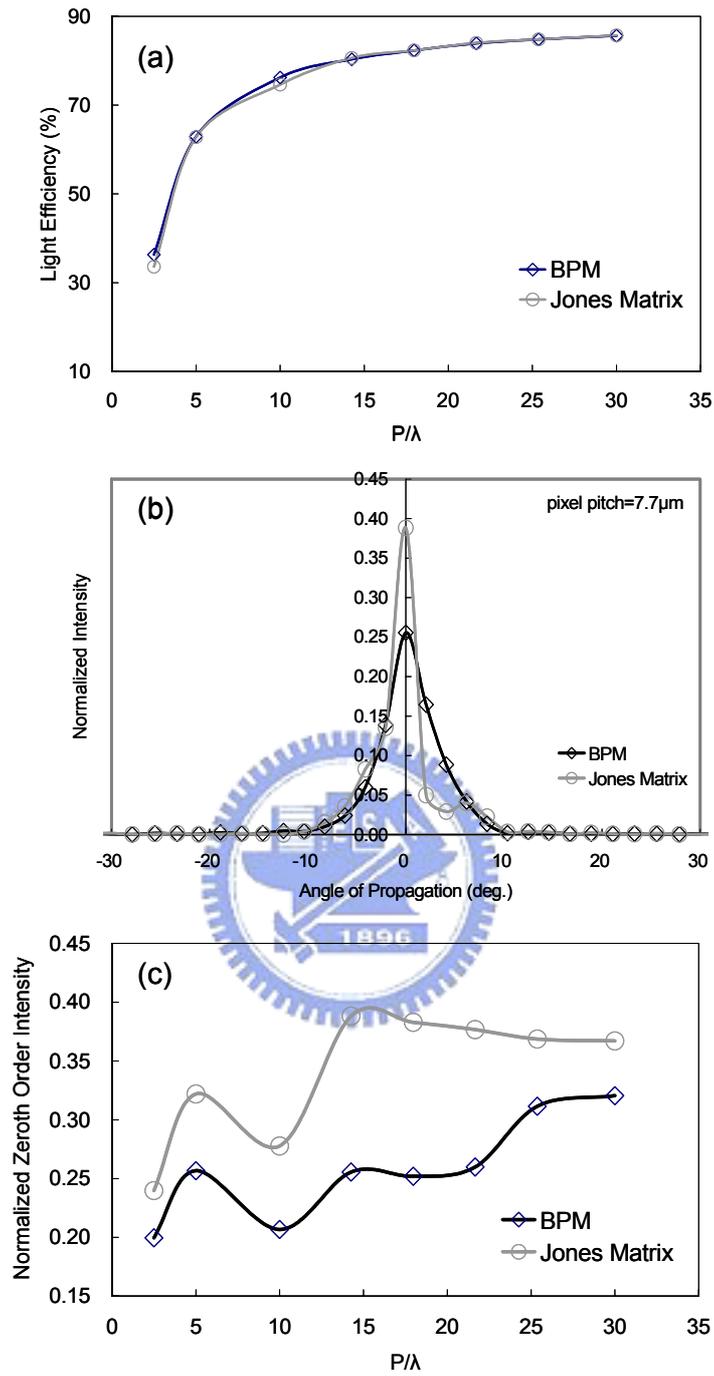


Fig. 5.7 Computer simulated results of VA mode with off-on-off pixel configuration by extended BPM and Jones matrix method: (a) light efficiencies ( $\theta_a=10^\circ$ ) of LCOS devices with respect to  $P/\lambda$  value, (b) intensity angular spectrum with  $P=7.7\mu\text{m}$  and  $\lambda=540\text{nm}$ , and (c) the intensity of zeroth-order diffracted light,  $I_0$ , calculated with respect to  $P/\lambda$  value.

### 5.3 Phase-compensated finger-on-plane mode

The extended BPM simulator is useful to design high resolution LCOS devices. By using this method, we can modify the structure of FOP mode to relax the diffraction effect by phase compensation between the propagating beams. As shown in Fig. 5.3 (a), appropriately selecting the thickness ( $d_i$ ) and the refractive index of the isolation layer between the common electrodes and the pixel electrodes can reduce the diffraction effect in some specific wavebands. The modified structure is called phase-compensated finger-on-plane modes. The simulated light efficiency with respect to the wavelength for the FOP mode ( $P=15.5 \mu\text{m}$ ) with different  $d_i$  as shown in Fig. 5.8. Here we assume the material of the isolation layer is  $\text{SiO}_2$  whose refractive index is about 1.46. From the figure, the green band exhibits a higher efficiency at  $d_i=115 \text{ nm}$  while the red and blue bands favor  $d_i=150 \text{ nm}$ . Therefore, one can boost the efficiency of the FOP device in a two- or three-panel projection system by optimizing the  $d_i$  corresponding to the RGB bands.

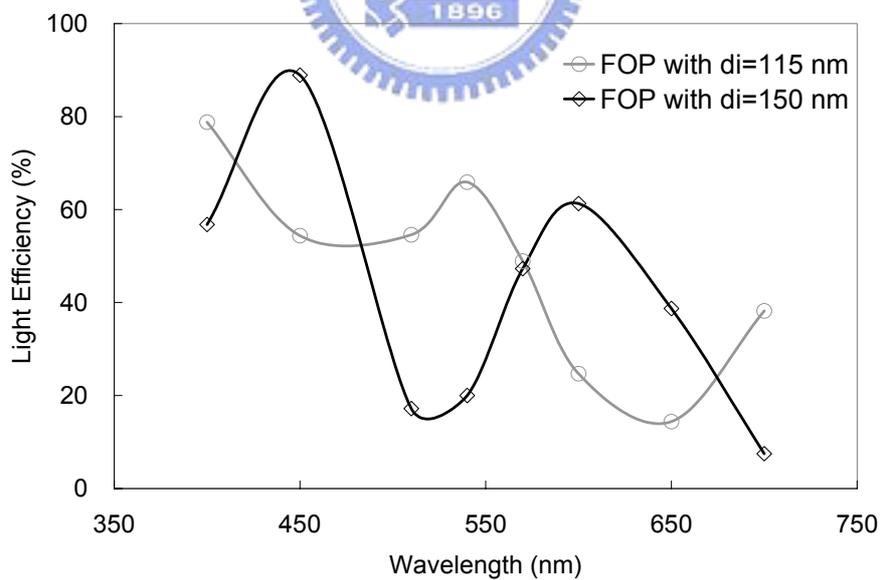


Fig. 5.8 Calculated light efficiency by reflective BPM with respect to wavelength for FOP mode ( $P=15.5 \mu\text{m}$ ) with  $d_i=115 \text{ nm}$  and  $150 \text{ nm}$ .

## 5.4 Conclusion

The conventional matrix-type methods can not authentically exhibits the optical characteristics when the pixel pitch becomes comparable to the wavelength. We extend the beam propagation method, which was commonly employed in the waveguide calculations, to simulate the optical performance of the high resolution LCOS devices. Light scattering and diffraction effects are included in the simulations. Two promising LC modes: vertically aligned and finger-on-plane LCOS devices are analyzed. Our results indicate that both modes are significantly influenced by the diffraction effect. The calculated light efficiency strongly depends on the pixel pitch. The optical behaviors are also explicitly described from the intensity angular spectra. We have shown that it is essential to employ the BPM for designing the LCOS devices. By using this rigorous simulation method, it is possible to design a LCOS system with minimum diffraction effect.



## References

- [1] Kuan-Hsu Fan Chiang, Shin-Tson Wu and Shu-Hsia Chen, “Analyzing the Diffraction Effect of LCOS Devices by Beam Propagation Method”, *AM-LCD'03*, pp. 247 (2003).
- [2] Kuan-Hsu Fan Chiang, Shu-Hsia Chen and Shin-Tson Wu, “Diffraction Effect on the High Resolution Liquid-Crystal-on-Silicon Device”, *Jpn. J. Appl. Phys.* **44**, (2005) in press.
- [3] E. E. Kriezis and S. J. Elston, *J. Mod. Opt.* **46**, pp.1201 (1999).
- [4] E. E. Kriezis and S. J. Elston, *Appl. Opt.* **39**, pp.5707 (2000).
- [5] D. K. G. de Boer, R. Cortie, A. D. Pearson, M. E. Becker, H. Wöhler, D. Olivero, O. A. Peverini, K. Neyts, E. E. Kriezis, and S. J. Elston, *Soc. Information Display Tech. Digest*, pp. 818, (2001).
- [6] E. E. Kriezis and S. J. Elston, *Liquid Crystals* **26**, pp.1663 (1999).
- [7] J. W. Goodman, *Introduction to Fourier Optics* (Robert & Company Publishers, 1996).
- [8] W. Y. Chou, L. S. Chuang, S. W. Chang, C. H. Hsu and H. C. Chiang, *Intl. Display. Workshop*, pp.217 (2001).
- [9] W. Y. Chou, C. H. Hsu, S. W. Chang, H. C. Chiang and T. Y. Ho, *Jpn. J. Appl. Phys.* **41**, 7386 (2002).
- [10] F. L. Pedrotti, S. J. and L. S. Pedrotti, *Introduction to Optics 2<sup>nd</sup> Edition*, (Prentice Hall, New Jersey, 1993).

## Chapter 6

# Summary and Future Scope

Liquid-crystal-on-silicon (LCOS) device is a promising candidate for projection displays. The standard manufacturing process of silicon wafers gives the potential of low cost of LCOS panels. Furthermore, the intrinsic high electron mobility of single-crystal silicon guarantees an extremely high resolution of LCOS devices. However, as the demand on resolution becomes higher, new problems arise. When the inter-pixel gap becomes comparable to the cell thickness, the fringing fields generated by the voltage difference between the adjacent pixels become critical to the optical performance of the LCOS devices. This fringing-field effect may decrease the brightness, contrast ratio, image sharpness and even the dynamic properties of the LC cells. Meanwhile, if the pixel pitch becomes comparable to wavelength of incident light, the diffraction effect becomes significant and may cause light loss of the optical system.

In this dissertation, the fringing-field effects in several commonly used LC operation modes are investigated. It is found that the mixed-mode twist nematic (MTN) cells are less sensitive to the fringing fields due to its relative thin cell gap. On the other hand, twist nematic (TN) modes suffer from strong fringing-field effect because of their thicker cell gaps to satisfy the Mauguin condition. Shrinking cell gaps may effectively reduce the fringing-field effects in TN modes. However, a special material with high birefringence needs to be employed. Therefore, the potential of TN-LCOS devices is limited. Vertically aligned (VA) mode is famous by its excellent dark state, which results in an extremely high contrast ratio. However, based on the simulated results, the fringing-field effect is particularly severe in VA mode. When the applied voltages are different between the adjacent pixels, a reverse-tilted regime will be form around the inter-pixel area due to the

fringing fields. LC distortions are generated near the pixel edges and extended toward the turned-on pixel. When the VA-LCOS panel is placed between crossed polarizers, dark stripes can be observed inside the bright pixel due to the LC distortions. This effect significantly decreases the image sharpness and brightness of the display. Furthermore, when a VA cell is switched from the dark-bright-dark state to the all-bright state, the LC distortions take a long time to relax back to the normal state. Therefore, severe image blurring can be observed when a movie is displayed. The effect of pixel pitch, cell gap, pretilt angle and electrode slope are also investigated.

In order to eliminate the fringing-field effect while keeping high contrast ratio, we have designed a circularly polarized light illuminated VA-LCOS (CPVA) device. Utilizing the characteristics of circularly polarized light, we are able to solve both the static and dynamic issues. The simulations and confirmed experimental results indicate that the sharpness and the brightness of the displaying images are significantly improved. Furthermore, the dynamic transition time from the dark-bright-dark state to the all-bright state is less than 10 ms, which has successfully overcome the image blurring effect. The optical properties of this promising device are interpreted qualitatively by the de Vries theory.

Another problem generated from the small pixel pitch of LCOS panel is the diffraction effect. The light loss caused by diffraction can be significant when the pixel pitch becomes comparable to the wavelength. In order to take the diffraction effect into account, a rigorous simulation method is needed. Conventional matrix-type solvers can cause severe miscalculating and are no longer available in this condition. The beam propagation method (BPM), which includes light scattering and diffraction, is found particularly suitable for high-definition LCD simulations. We further extend this method to analyze the reflective LCOS device. Two promising LC modes, VA and finger-on-plane (FOP), are analyzed. The calculated light efficiencies with respect to pixel pitch are presented. The results are

compared to those obtained by Jones matrix method. It is shown that the BPM demonstrates much more reasonable results than Jones matrix method does. By using this powerful tool, we present a phase-compensated FOP mode in which the diffraction effect is reduced for certain wavebands.

The CPVA device successfully overcomes the long standing problem caused by fringing fields. However, as discussed in Chap 4, either off-axis design or a Faraday rotator is needed in its optical engine. For the topic of future works, it is a subject to design an optimal optical engine for the CPVA device. Using hologram films is a good approach to achieve this goal. In order to obtain good efficiency of the hologram films, rigorous analyses based on the couple wave theory are needed. On the aspect of diffraction effect of LCOS panel, further investigations by using BPM are needed for optimizing the panel structure and minimizing the light loss.



# Vita

## ● Personal Information:

Kuan-Hsu Fan-Chiang 范姜冠旭

Date of Birth: Feb. 26<sup>th</sup>, 1978.

E-mail: simonf.eo89g@nctu.edu.tw

Phone: +866-3-5712121 ext. 56344

Contact Address: 4F, No. 253, Puding Rd., Hsinchu, 300, R.O.C.

(300 新竹市埔頂路 253 號 4 樓)

## ● Education

---

Ph. D. 2002/2~2005/6 Institute of Electro-Optical Engineering, National Chiao Tung University. (國交通大學光電工程研究所)

---

2003/7~2004/6 Exchanged student at College of Optics and Photonics/CREOL /FPCE, University of Central Florida.

---

2000/9~2002/1 Institute of Electro-Optical Engineering, National Chiao Tung University; Directly promoted to the Ph. D. Program.  
(國交通大學光電工程研究所；直生博士班)

---

B. S. 1996/9~2000/6 Department of Electrophysics, National Chiao Tung University.  
(國交通大學電子物理學系)

---

## ● Awards

2004	第十五屆美國佛羅里達州中華學人年會學生論文獎
2003	國科會補助博士生赴國外研究獎學金 (千里馬計畫)
2002	教育部博士班研究生獎學金
2001	國立交通大學光電工程研究所書卷獎
2000	教育部碩士班研究生獎學金
1997~1999	國立交通大學電子物理學系書卷獎

# Publication List

## A. Journal Papers 期刊論文

- [1] **Kuan-Hsu Fan Chiang**, Shin-Tson Wu and Shu-Hsia Chen, “Fringing Field Effect of the Liquid-Crystal-on-Silicon Devices”, *Jpn. J. Appl. Phys.* Vol. 41, pp. 4577-4585 (2002).
- [2] **Kuan-Hsu Fan Chiang**, Shu-Hsia Chen and Shin-Tson Wu, “Diffraction Effect on the High Resolution Liquid-Crystal-on-Silicon Device”, *Jpn. J. Appl. Phys.* Vol. 44, pp. 3068-3072 (2005) .
- [3] Yi-Hsin Lin, Hongwen Ren, **Kuan-Hsu Fan-Chiang**, Wing-Kit Choi, Sebastian Gauza, Xinyu Zhu and Shin-Tson Wu, “Tunable-Focus Cylindrical Liquid Crystal Lenses”, *Jpn. J. Appl. Phys.* Vol. 44, pp. 243-244 (2005).
- [4] **Kuan-Hsu Fan Chiang**, Shin-Tson Wu and Shu-Hsia Chen, “High-definition vertically-aligned liquid crystal microdisplays using a circularly-polarized light”, *Applied Phys. Lett.*, to be published (July 25, 2005).
- [5] **Kuan-Hsu Fan-Chiang**, Shin-Tson Wu and Shu-Hsia Chen, “Fringing-field effects on high-resolution LCOS devices”, *J. Display Technology*, to be submitted.

## B. Conference Papers 會議論文

- [1] **Kuan-Hsu Fan Chiang**, Shin-Tson Wu and Shu-Hsia Chen, “Sloped Electrodes for Minimizing Fringing Field Effect of LCOS”, *Proc. Asia Display/Intl. Display Workshop*, pp. 1723-1724 (2001).
- [2] **Kuan-Hsu Fan Chiang**, Ching-Yih Chen and Shu-Hsia Chen, “Dynamic Simulation of Vertical-Aligned pi-cell Liquid Crystal”, *Taiwan Liquid Crystal Society conference*, pp.57 (2001).
- [3] Chao-Hsu Liu, Jung Y. Huang, **Kuan-Hsu Fan Chiang** and Shu-Hsia Chen, “Study on the Surface Anchoring Properties of a Photo-Decomposable Polyimide”, *Proc. Optics and Photonics Taiwan*, Vol.3, pp.58 (2002).
- [4] Chao-Hsu Liu, Jung Y. Huang, **Kuan-Hsu Fan Chiang** and Shu-Hsia Chen, “Study on the Alignment Properties of a Photo-Decomposable Polyimide”, *Proc. International Display Manufacturing Conference*, pp.599 (2003).
- [5] **Kuan-Hsu Fan Chiang**, Shin-Tson Wu and Shu-Hsia Chen, “Analyzing the Diffraction Effect of LCOS Devices by Beam Propagation Method”, *AM-LCD*, pp. 247 (2003)
- [6] **Kuan-Hsu Fan Chiang**, Shin-Tson Wu and Shu-Hsia Chen, “A Novel Method to Reduce the Diffraction Effect for Finger-On-Plane LCOS Device”, *Taiwan*

*Liquid Crystal Society conference*, pp.51 (2003).

- [7] **Kuan-Hsu Fan Chiang**, Shu-Hsia Chen, Xinyu Zhu and Shin-Tson Wu, “Comparative Studies of Liquid-Crystal-on-Silicon Microdisplay Modes”, *Proc. Of 15<sup>th</sup> Conference of The Chinese-American Scholars Association of Florida*, pp.27 (2004).
- [8] **Kuan-Hsu Fan Chiang**, Xinyu Zhu, Shin-Tson Wu and Shu-Hsia Chen, “Eliminating fringing field effects of vertically aligned liquid-crystal-on-silicon by using circularly polarized light”, *Soc. Information Display Tech. Digest*, Vol. 36, pp. 1290 (2005).

## C. Patent 專利

- [1] 范姜冠旭, 朱新羽, 吳詩聰, 王淑霞, “光學系統設計”, 台灣和美國專利申請中。

## D. Others 其它

- [1] 范姜冠旭, 王淑霞, 朱新羽, 吳詩聰, “液晶模態對於反射式矽液晶顯示器之影響”, *光訊* 108 期, pp. 13 (2004).
- [2] 范姜冠旭, 吳詩聰, 王淑霞, “反射式單晶矽液晶顯示器”, 王淑霞教授榮退學術研討會—液晶科學與技術 (2005).